Dissertation zur Erlangung des Doktorgrades
der Fakultät für Chemie und Pharmazie
der Ludwig-Maximilians-Universität München

Uniting Hydride, Nitride and Nitridoborate Anions – Synthesis and Characterization of Novel Multianionic Compounds

Sophia Lena Wandelt
aus
München, Deutschland

2023

Erklärung

Diese Dissertation wurde im Sinne von §7 der Promotionsordnung vom 28. November 2011 von Herrn Prof. Dr. Wolfgang Schnick betreut.

Eidesstattliche Versicherung

Diese Dissertation wurde eigenständig und ohne unerlaubte Hilfsmittel erarbeitet

München, den 06.11.2023

_____

Sophia Lena Wandelt

Dissertation eingereicht am:	06.11.2023
1. Gutachter:	Prof. Dr. Wolfgang Schnick
2. Gutachter:	Prof. Dr. Hubert Huppertz
Mündliche Prüfung am:	12.12.2023

Manchmal sollte man sich statt Sorgen lieber Nudeln machen

unbekannt

Danksagung

Mein erster Dank gilt meinem Doktorvater Herrn Prof. Dr. Schnick für die freundliche Aufnahme in seinem Arbeitskreis, die stete Hilfsbereitschaft und die Möglichkeit meine Dissertation anfertigen zu können. Ich bedanke mich für die anfängliche Einführung in das Gebiet der Leuchtstoffe und die anschließende Möglichkeit, zu den spannenden Hydriden und Nitridoboraten zu wechseln. Zudem hat die von Ihnen initiierte Kooperation mit Frau Prof. Dr. Nathalie Kunkel und Dr. Alexander Mutschke meine Forschung wirklich sehr bereichert.

Herrn Prof. Dr. Hubert Huppertz möchte ich für die Übernahme des Zweitgutachtens meiner Dissertation danken. Des Weiteren habe ich mich sehr über die Organisation der Obergurgl-Festkörperseminare gefreut, in denen ich meine Forschungsergebnisse schon in der Masterarbeit in einer angenehmen und freundschaftlichen Atmosphäre präsentieren konnte.

Darüber hinaus danke ich Herrn Prof. Dr. Holger Kohlmann, Frau Prof. Dr. Silvija Markic, Herrn Prof. Dr. Thomas Klapötke und Herrn Prof. Dr. Hans-Christian Böttcher für die freundliche Bereitschaft zur Teilnahme an meiner Promotionskommission.

Ein besonderer Dank gilt Dr. Alexander Mutschke, der mir immer alle Fragen bezüglich der Hydride und jeglicher Analytik beantwortet hat und mit seinem Wissen und quantenchemischen Rechnungen stets tatkräftig zur Seite stand. Ohne diese Hilfe wäre die Auswertung und Publikation meiner Forschungsergebnisse nicht in diesem Umfang möglich gewesen.

Bei Olga Lorenz, Wolfgang Wünschheim und Dr. Dieter Rau bedanke ich mich für die freundliche und zuverlässige Unterstützung in allen organisatorischen, computertechnischen sowie sicherheitsrelevanten Bereichen.

Mein Dank gilt zudem Dr. Dmitry Khalyavin für die zahlreichen Neutronenmessungen, deren Auswertung und die freundliche Aufnahme am ISIS in Oxford.

Christian Minke, Jennifer Steinadler und Dr. Thomas Bräuniger danke ich für die Messung und Auswertung meiner NMR-Spektren sowie die Beantwortung aller meiner Fragen dazu.

Des Weiteren danke ich Herrn Prof. Dr. Antti Karttunen für die theoretischen Rechnungen zu den NMR-Messungen.

Ayla Karnas danke ich für ihre praktische und synthetische Unterstützung während ihrer Bachelorarbeit und ihrer Zeit als wissenschaftliche Hilfskraft.

Obwohl ich dem Themengebiet der Leuchtstoffe letztendlich doch noch entflohen bin, möchte ich mich bei den Kooperationspartnern von Lumileds, Dr. Peter Schmidt, Dr. Philipp Strobel und Dr. Niels Van der Veen bedanken. Durch die zahlreichen Meetings und Besuche in Aachen schon seit meiner Masterarbeit konnte ich viel über Lumineszenz lernen.

Robert Calaminus und Frau Prof. Dr. Bettina Lotsch danke ich für die Messung und Auswertung der Ionenleitfähigkeitsmessungen.

Bei Dr. Peter Mayer möchte ich mich für die Einweisung und Unterstützung am Einkristalldiffraktometer bedanken.

Meinen aktuellen und ehemaligen Laborkollegen Dr. Eugenia Elzer, Dr. Lucien Eisenburger, Dr. Simon Kloß, Dr. Dieter Rau und Monika Pointner danke ich für die angenehme Arbeitsatmosphäre und besonders letzterer für die vielen unterhaltsamen Gespräche während der Arbeit.

Meinen Freunden und Kollegen Reinhard Pritzl, Florian Engelsberger, Amalina Buda, Lisa Gamperl, Thanh Chau, Sebastian Ambach, Thaddäus Koller, Tobias Giftthaler, Georg Krach und Mirjam Zipkat danke ich für die anregenden Diskussionen und die lustige Zeit innerhalb und außerhalb des Labors.

Zudem möchte ich mich bei allen anderen Mitgliedern der Arbeitskreise Schnick, Hoch, Johrendt und Lotsch für die Unterstützung und für die vielen unterhaltsamen Momente in der Kaffeeküche bedanken.

Darüber hinaus möchte ich mich von ganzem Herzen bei meinem Freund Marwin Dialer bedanken, der mir mit fachlichen sowie persönlichen Gesprächen stets hilfsbereit zur Seite stand. Danke, dass Du Dir immer alle meine Probleme angehört hast.

Zu guter Letzt bedanke ich mich noch bei meinen Eltern und bei meiner Schwester. Danke, dass Ihr mich stets unterstützt und auf diesem langen Weg begleitet habt.

Table of Contents

1 Introduction

1.1 Multianionic Compounds

The combination of multiple anions in one compound is proving itself as an alternative way to modify the structural, electronic, optical and physical properties of materials.[1] The well-known multiple cation approach already convinced as a powerful tool of compound tuning, for example, tailoring the emission wavelength of Eu^{2+} doped phosphors.[2-3] Taking this into the extreme with a combination of four or more different atoms results in high entropy compounds, such as ultra-hard nitride ceramics.[4] However, combining different anions with distinct ionic radii, electronegativities and coordination geometries add new dimensions to synthesize unprecedented materials.[5-6] The bonding situation in such materials can be influenced by ionic or covalent contributions, which allows tuning of the bandgap and the crystal field splitting. Introducing distinct anions in known structures results in local asymmetry and complex anions further expand the structural diversity. Similar to traditional single-anion compounds, multianionic species are widely dominated by oxides and fluorides due to their high reactivity and stability. Hydride, nitride and nitridoborate anions are already well-explored on their own, but also manifold combinations with oxide or halide ions are reported. After discovering $LaSrCoH_{0.7}O_3$ and its high magnetic ordering temperature, the research on hydride oxides gained rising attraction.[7] While the series $La_{2-y}Sr_yLiH_{1+y}O_{3-y}$ convinces with high hydride ion conductivity, Sr_2LiSiO_4H and Sr_3AlO_4H show intense luminescence upon doping with lanthanides.[8-10] Nitridoborate halides, for example, exhibit a great structural diversity with mostly bent $[BN_2]^{3-}$ units and low symmetric crystal structures. The series $M_2[BN_2]X$ (*M* = Mg, Ca, Sr, Ba, Eu and *X* = F, Cl, Br, I) yielded 13 new compounds and despite their identical formula type, only few of them are isostructural, resulting in eight different structure types.[11] This effect is presumably caused by complex packing effects arising from the changing ionic radii of the halides, leading to different structural moieties. However, nitride halides such as *M*N*X* with *M* = Ti, Zr, Hf and *X* = Cl, Br, I are mostly isotypic and crystallize in two different polymorphs of a layered structure, which consist of *M*–N double layers sandwiched between halide layers. Moreover, such compounds can act as photocatalysts or superconductors.[12-13]

With these compounds being just a small overview, the field of multianionic compounds is far-reaching and many regions are still unexplored yet. However, this thesis only focuses on the structurally intriguing hydride, nitride and nitridoborate anions and combinations thereof.

1.2 Different Anions and their Relatives

1.2.1 The Hydride Ion

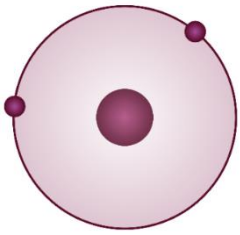

Hydrogen makes up more than 90% of all matter in the universe and plays a pivotal role in the formation of stars and galaxies.[14] Despite its low abundance on planet earth, hydrogen represents two-thirds of the atoms in the human body and thus plays an essential role in our lives, which are governed by organic chemistry. Most hydrogen compounds contain cationic hydrogen – *protons* – but the class of materials containing anionic hydrogen – *hydrides* – has attracted more and more attention over the last decades among inorganic chemists. The hydride ion itself is the electronically simplest anion and consists of only one proton and two electrons, fulfilling the noble gas configuration. The excess electron is not tightly bound to the nucleus and with a moderate electronegativity of 2.2 on the Pauling scale, the hydride is considered a "soft" anion with varying ionic radius and high polarizability.[15-16] While most of the hydrides are clearly ionically bound, its polarizability can result in bonding situations that possess significant covalent contributions, depending on the respective bonding partner. Therefore, the ionic radius of the hydride ion is widely discussed to range from 132 to 208 pm, dictated by its chemical surrounding.[17-21] The coordination environment of the hydride ion in metal hydrides can be linear, trigonal planar, tetrahedral, trigonal bipyramidal or even octahedral (Figure 1.1) with $M^{\delta+}$–$H^{\delta-}$ distances of 1.6 to 3.0 Å.[22-25] Such materials show properties like magnetic ordering, hydride ion conductivity or even superconductivity.[26-28] When another metal or non-metal is added to salt-like hydrides, they can also form complex anions such as $[NiH_4]^{2-}$ or $[BH_4]^-$.[29-30]

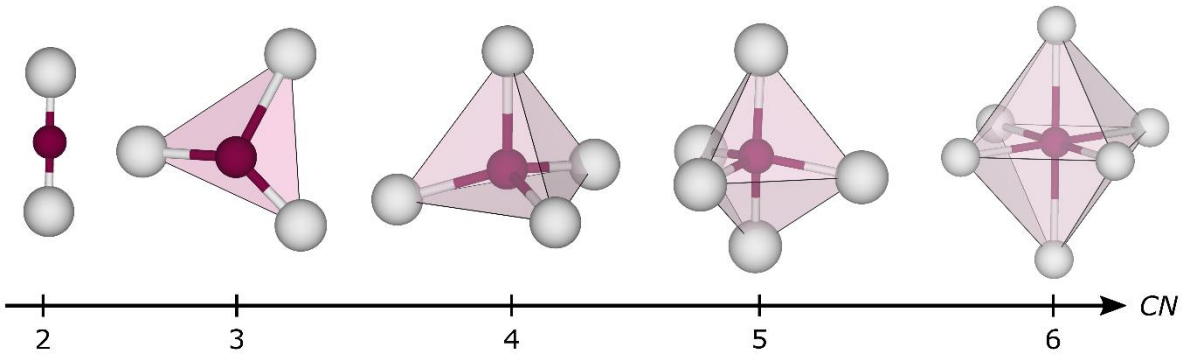

Figure 1.1. Different coordination spheres of the hydride ion from left to right in $LiNiH_3$ (linear), $CaAlH_5$ (trigonal planar and tetrahedral), $LiCa_3As_2H$ (trigonal bipyramidal) and Ba_2NH (octahedral) with coordination number (*CN*) 2 to 6.[22-25] The hydride ions are shown in purple and the respective metal cations in gray.

The Hydride-Fluoride Analogy

As the fluoride anion has the same charge and a similar ionic radius of 133 pm, many hydrides and fluorides crystallize isostructurally, which is known as the hydride-fluoride analogy.[18,31] This can be observed for the binary alkali and alkaline earth compounds as well as in ternary alkali or alkaline earth perovskites. But despite their structural relation, the syntheses, number of reported compounds and physical properties differ significantly.[32] Due to their higher stability and easier accessibility, the fluoride compounds clearly outnumber the more fragile hydrides. However, even hydride fluoride solid-solution series, such as NaH_xF_{1-x} or $SrH_{2-x}F_x$, are reported lately, whereas the latter even shows tunable luminescence upon doping with Eu^{2+}.[33-34] The emission maxima in the series $SrF_2:Eu^{2+}$ to $SrH_2:Eu^{2+}$ show a continuous redshift, known as the nephelauxetic effect. As the hydride builds more covalent bonds to the activator ion than the fluoride, the crystal field splitting is larger, resulting in a shift of the emission maximum to lower energies.[9-10]

1.2.2 The Nitride Ion

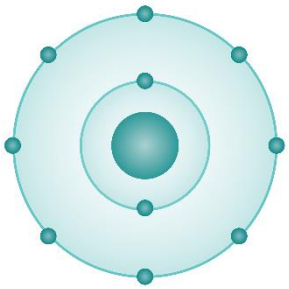

With almost 80% abundance N_2 is the main component of the earth's atmosphere. Due to the strong triple bond between the two nitrogen atoms, it is inert under ambient conditions, in contrast to the much more reactive O_2. Nevertheless, choosing the right reactants and raising the synthesis temperature enables to break the N–N bond and incorporate nitride ions into different materials. Such compounds are important components in both organic and inorganic chemistry. While nitrogen is often bound in an amide ($–NH_2$) or nitro ($–NO_2$) group in organic materials, it shows a great variety of bonding situations in inorganic solids. Nitrides are found in complex moieties such as $[NH_4]$, $[BN_3]$, $[PN_4]$ or $[SiN_4]$ or as an isolated anion. Although the latter is less common in multinary solid-state materials, the N^{3-} ion already shows a wide diversity of coordination environments in binary nitrides, ranging from *CN* = 2 to *CN* = 9 (Figure 1.2). The metal–nitride bond lengths hereby vary significantly from 1.41 to 2.78 Å.

Many binary nitride compounds are of high interest in industry with TaN, Si_3N_4 and VN being just three examples of commercially used semiconductors, ultra-hard coatings or catalysts, respectively.[35-37] Moreover, multinary nitrides such as $Sr_2[Si_5N_8]:Eu^{2+}$ or $Ca[AlSiN_3]:Eu^{2+}$ are efficient phosphors for white light emitting pcLEDs.[38]

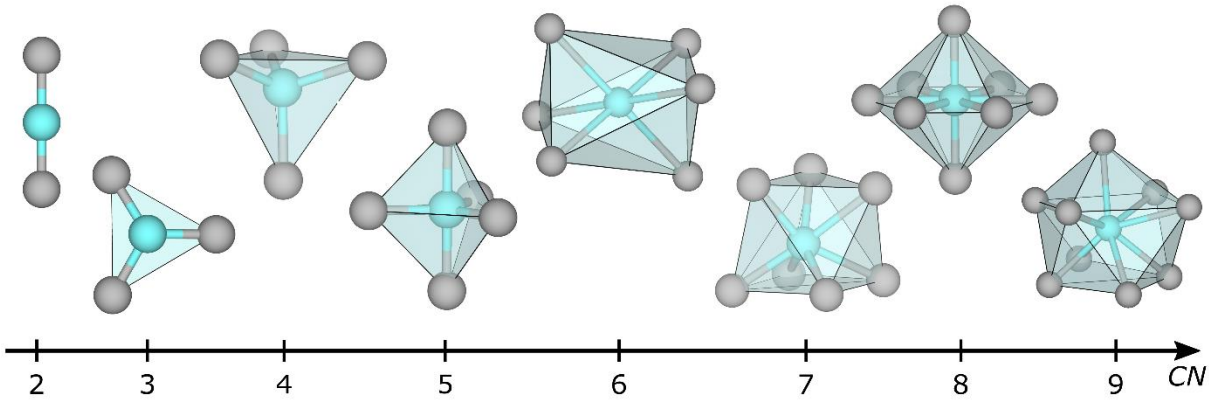

Figure 1.2. Different coordination spheres of the nitride ion from left to right in MoN (linear), h-BN (trigonal planar), AlN (tetrahedron), Be_3N_2 (trigonal bipyramid), K_3N (trigonal antiprism), hp-Mg_3N_2 (capped trigonal prism), Li_3N (hexagonal bipyramid) and hp-Na_3N (capped quadratic antiprism).[39-46] The nitrides are shown in blue and the respective metal cations in gray.

Nitrides and Oxides

Despite the nitride ion having a slightly larger ionic radius than the oxide, both are building many isotypic or related structures and are also often found together in one compound, known as oxonitrides. However, the number of oxide materials easily surpasses the nitrides as oxygen has a rather weak double bond and two free electrons, resulting in high reactivity. Therefore, the vast majority of minerals are oxidic, whereas nitridic ones are found very rarely and solely under oxygen-free conditions, which means they are formed almost exclusively in meteorites. Taking a closer look on the binary and ternary compounds, the structural similarities become clearer. For example, the third group nitrides BN, AlN, GaN, and InN crystallize in the wurtzite type, like BeO, CoO and ZnO.[47] Moreover, the series Ge_3N_4–Ge_2SiN_4–$GeSi_2N_4$–Si_3N_4 are found in the spinel group, which is well-known for oxides such as $MgAl_2O_4$ or $CoFe_2O_4$. Furthermore, the binary nitrides and oxides of most of the rare earth metals as well as of some transition metals belong to the rock salt family.[47] Both nitrides and oxides are known as stable, inert materials and BN, Al_2O_3 or Si_3N_4, for example, can be employed as crucible materials or high-temperature ceramics, respectively.

1.2.3 The $[BN_2]^{3-}$ Unit

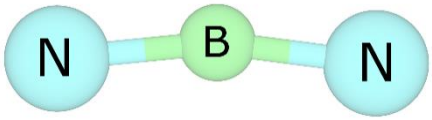

Hexagonal boron nitride (h-BN) belongs to the technically important binary main group nitrides. As it is building layers of covalently bound B_3N_3 hexagons, it is often referred to as "white graphite".[48] Nitridoborate anions arise as a substructure of h-BN and usually occur as a linear or slightly bent $[N–B–N]^{3-}$ unit.[11] Under more extreme synthesis conditions trigonal planar $[BN_3]^{6-}$ units or even $[BN_4]^{9-}$ tetrahedra can be found.[49-50] Moreover, nitridoborates can also form structural motifs known from organic chemistry such as oxalate-like $[B_2N_4]^{8-}$ units or hexagonal $[B_3N_6]^{9-}$ rings.[51-52]

$Li_3[BN_2]$, $Ca_3[BN_2]_2$ and $Ba_3[BN_2]_2$ were the first compounds with linear $[BN_2]^{3-}$ anions, reported by Goubeau and Anselment in 1961.[53] Since then, systematic analyses on ternary and quaternary nitridoborates with alkali and alkaline earth metals have been performed. Within these compounds, it can also appear as a slightly bent anion with N–B–N angles between 168 and 180° and B–N distances between 1.31 and 1.39 Å.[11] Usually, the nitridoborate anion is coordinated 6-, 8- or 10-fold by its counter ions (Figure 1.3). While most of the nitridoborate halides show a distorted trigonal prism (*CN* = 6), the coordination sphere in the highly symmetric ternary compounds can be described as a bicapped quadratic prism (*CN* = 10).[54-55] Another recurring coordination polyhedron is the bicapped trigonal prism (*CN* = 8), such as in β-$Ba_3[BN_2]_2$.[56]

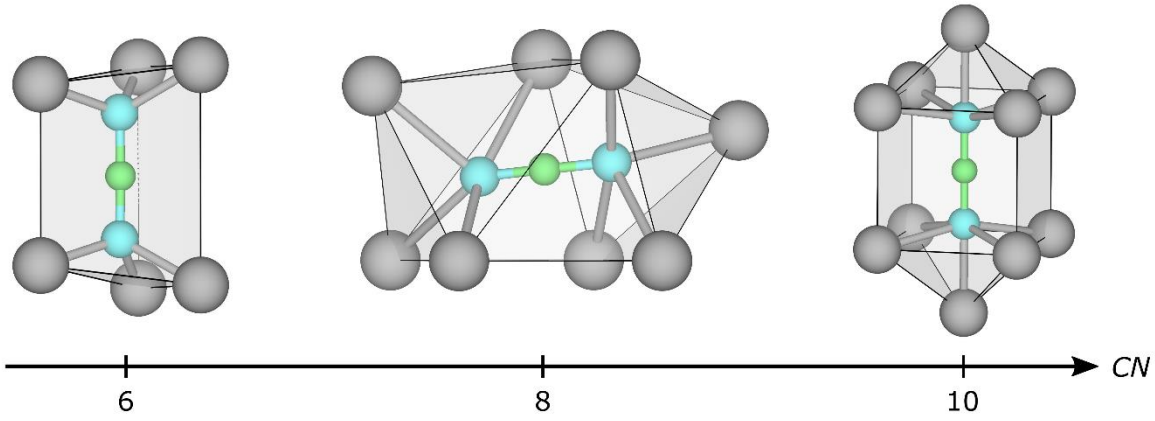

Figure 1.3. Different coordination spheres of the $[BN_2]^{3-}$ anion from left to right in $Mg_8[BN_2]_5I$ (trigonal prism), β-$Ba_3[BN_2]_2$ (bicapped trigonal prism) and $LiCa_4[BN_2]_3$ (bicapped quadratic prism). The boron atoms are displayed in green, nitrogen in blue and the metal ions in gray.

Isoelectronic Anions

Next to the most prominent analogue CO_2, the $[BN_2]^{3-}$ unit has even more triatomic linear relatives containing 16 electrons with $[N_3]^-$, $[OCN]^-$, $[CNO]^-$, $[CN_2]^{2-}$, $[BO_2]^-$, $[C_3]^{4-}$, $[CBN]^{4-}$ and $[BC_2]^{5-}$ being some examples (Figure 1.4). Due to their changing ionic radii and bonding situations, these triatomic anions show fundamentally different bond lengths, structures and properties.

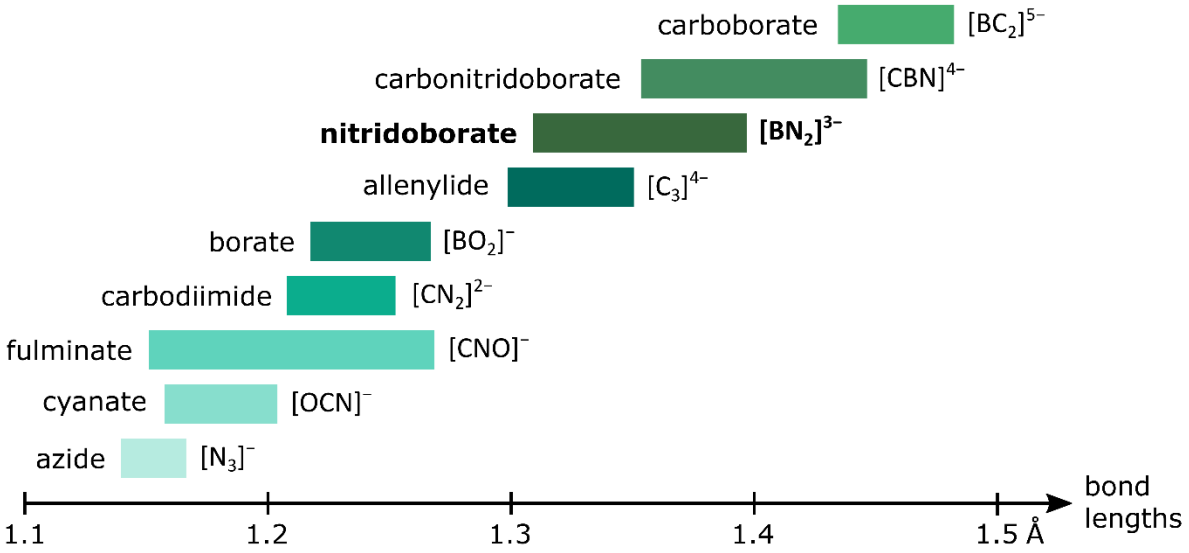

Figure 1.4. Depiction of the different isoelectronic $[A–B–C]^{x-}$ anions sorted by their respective *A*–*B* and *B*–*C* distances. A detailed list of all triatomic anions with the bond distances and angles as well as their references can be found in Chapter 8.1.

Taking a closer look reveals $[CBN]^{4-}$ and $[C_3]^{4-}$ as the structurally most related anions to the $[BN_2]^{3-}$ unit. They show akin bond lengths and share an often appearing polyhedron, the bicapped trigonal prism, coordinated by the respective metal cations.[56-58] The carbonitridoborate anion can also be linear or slightly bent with angles of 175 to 180° and shows somewhat larger interatomic distances of 1.35 to 1.44 Å.[58-59] It is even found together with nitridoborate units in one single compound, namely $Ca_{10}[BN_2]_4[CBN]_2$.[60] The allenylide anion, however, appears usually slightly bent with a C–C–C angle of about 170° and shorter bond lengths of 1.30 to 1.35 Å.[61-62] $Ca_3Cl_2[C_3]$ also crystallizes isotypic to $Ca_3Cl_2[CBN]$, emphasizing the structural similarities of these anions even more.[59,62]

With these compounds being just an overview of some relatives of $[BN_2]^{3-}$, there are several more isoelectronic units such as the heavier analogues $[BP_2]^{3-}$ and $[BAs_2]^{3-}$ or even the nitronium ion $[NO_2]^+$.[63-64] Moreover, even some transition metals such as Ni, Cu, Ag and Hg build similar $[O–M–O]^{x-}$ moieties with even longer *M*–O distances of 1.8 to 2.2 Å.[65-68]

1.3 Analytical Methods

After the successful synthesis of compounds containing hydride, nitride and nitridoborate anions, their structural analysis can bear some challenges. As all three anions have their own peculiarities, a combination of analytical methods has to be taken into account to fully characterize such materials. While single-crystal X-ray and neutron powder diffraction data are essential to solve the crystal structure, MAS NMR and vibrational spectroscopy further support the presence of the different structural motifs.

1.3.1 Single-Crystal X-ray Diffraction

If the desired sample yields crystals in appropriate sizes, single-crystal X-ray diffraction is an easily accessible and suitable method to elucidate the crystal structure. X-rays interact with the electron shell of an atom and therefore, heavier elements are easier detectable than light ones. The atomic form factor *f* is the Fourier transform of the electron density and describes how effective X-rays are diffracted by the respective atoms (Figure 1.5, left). However, the atomic form factor *f* decays quickly with increasing diffraction angle θ, which leads to low intensities at higher angles. The form factors of barium and strontium are large enough to determine their crystallographic positions with high accuracy.[69] Nitrogen and boron show a smaller *f*, but are still reliably detectable with X-ray diffraction experiments, if the crystal quality is sufficient. The atomic form factor of hydrogen is close to zero, which only allows the determination of its crystallographic positions with relatively large errors, if at all.

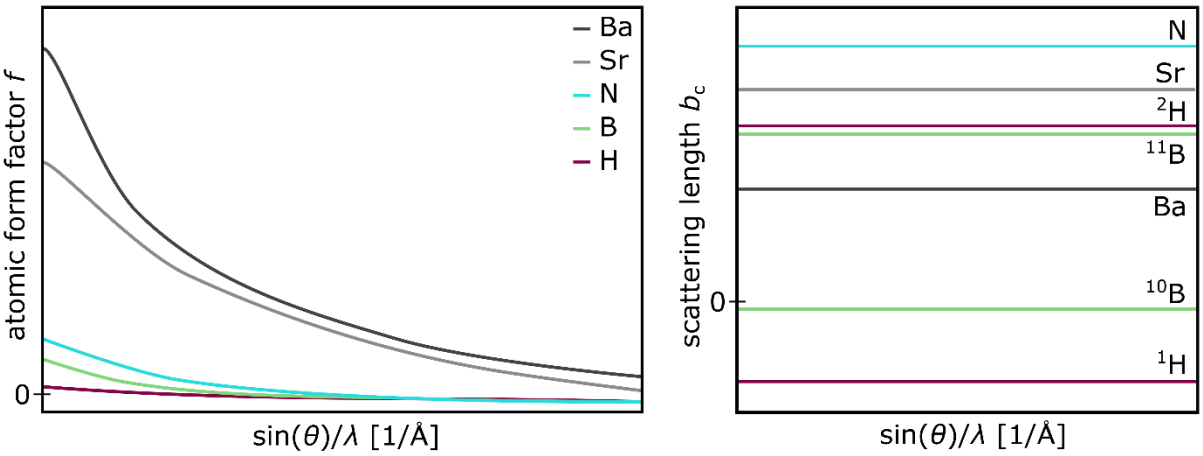

Figure 1.5. Schematic depiction of the atomic form factor *f* (left) and coherent scattering length b_c (right) of barium, strontium, nitrogen, boron and hydrogen.

1.3.2 Neutron Powder Diffraction

In contrast, neutrons interact with the atomic nucleus rather than the electron shell and are well suited for the reliable analysis of light elements. The coherent scattering length b_c describes how the neutrons are interacting with the nucleus, similar to the atomic form factor f. However, b_c does not correlate with the atomic number and remains constant for increasing θ (Figure 1.5, right).[70] The scattering of neutrons depends, among other factors, on the spin of the nucleus and allows different isotopes of an element to be distinguished.[71] For example, ^{1}H has a negative b_c and shows incoherent scattering, which can significantly deteriorate the data quality due to the formation of a large background. However, ^{2}H has a b_c of 6.7 fm and is well suited for neutron diffraction experiments. Similarly, ^{10}B is known as an efficient neutron absorber (b_c = −0.1 fm) while ^{11}B shows a reasonable b_c of 6.6 fm, which often requires an isotopic modification to obtain reliable data.[71] However, the use of neutron diffraction for analysis is not straightforward as the access to experimental institutions is restricted and the sample preparation can be challenging. The source of the neutrons used for diffraction experiments can either be obtained from a nuclear reactor or a spallation source (Figure 1.6).[72]

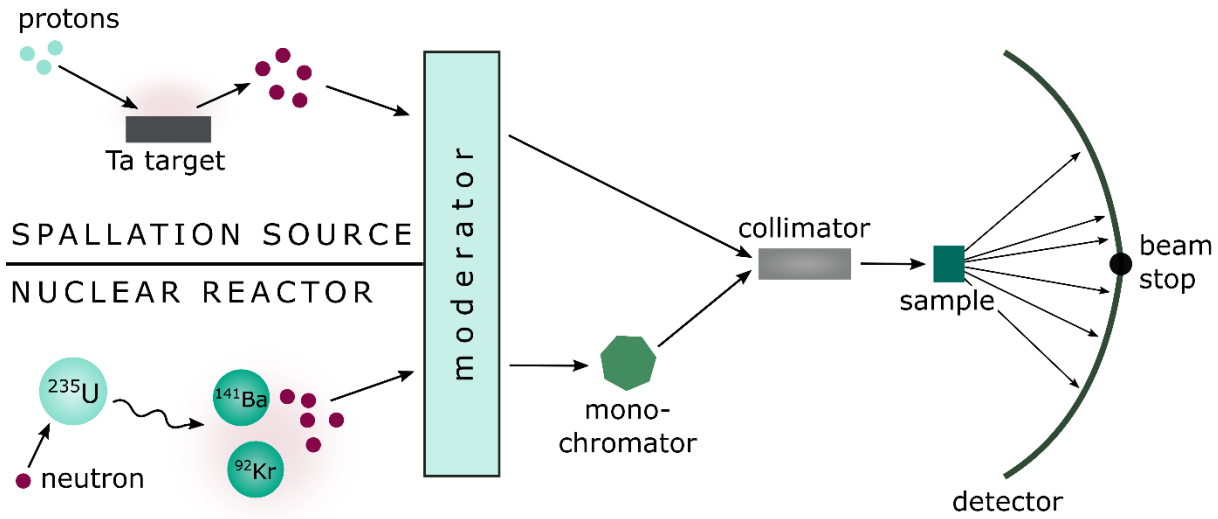

Figure 1.6. Simplified schematic illustration of the neutron beamline of spallation source and nuclear reactor.

In a reactor, a controlled nuclear fission chain reaction is used to generate neutrons. A first neutron is accelerated on a ^{235}U nucleus, initiating a nuclear fission which typically releases ^{141}Ba and ^{92}Kr, energy and neutrons. These neutrons further collide with other uranium nuclei, starting a self-sustaining chain reaction which constantly produces neutrons.[73] At a spallation source, protons are accelerated on a heavy metal target, usually tantalum or tungsten, which then emits

high energetic neutrons. Contrary to the fission source, a spallation source needs constant supply of protons for the new formation of neutrons. To use these neutrons from either source for diffraction experiments, they need to slow down in moderator tanks, which are usually filled with water or solid methane. In nuclear reactors, the angle-dispersive diffraction method is frequently used (constant wavelength experiment): the neutron beam is monochromatized and only a single wavelength is used for the experiments, analogous to a laboratory X-ray diffraction setup. At most spallation sources, the "white" neutron beam is directly focused on the sample and the detection of the neutrons is time-dispersive (time-of-flight experiment). Both methods result in a two-dimensional diffraction pattern, which can be further evaluated by Rietveld refinement and provides information about the atomic positions, crystal structure and magnetic properties of the sample.[74]

1.3.3 Nuclear Magnetic Resonance

To further validate the structure model obtained from diffraction data, nuclear magnetic resonance (NMR) can be a helpful tool to examine hydrogen or boron containing compounds. To reduce anisotropic interactions, the Magic Angle Spinning (MAS) NMR technique is often used for solid-state samples, in which the sample is rotated rapidly at the magic angle of 54.7° (Figure 1.7). The position of the NMR signal, which is equal to the isotropic chemical shift δ_{iso} for non-quadrupolar nuclei, as well its shape contains information about the chemical environment of the respective atom. For spectra influenced by quadrupolar interactions, a fitting of the signal can provide further information such as δ_{iso} and the quadrupolar coupling constant C_Q.

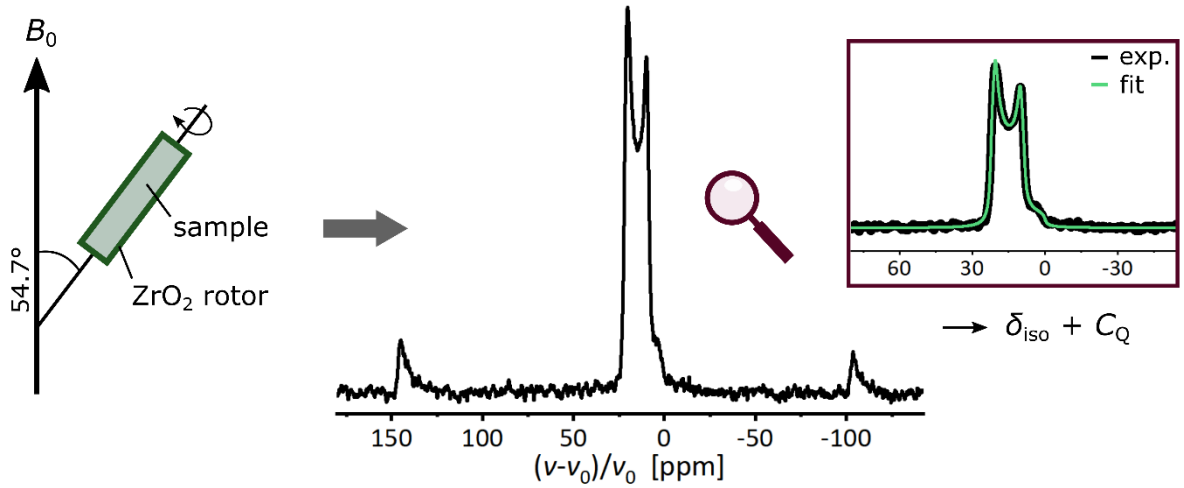

Figure 1.7. Schematic illustration of a MAS NMR experiment of a quadrupolar nucleus with the resulting spectrum and its fit with the isotropic chemical shift δ_{iso} and quadrupolar coupling constant C_Q.

^{1}H MAS NMR

With 99.99% natural abundance and a spin of 1/2, ^{1}H is well suited for NMR measurements although it is mainly used to study protons in liquid organic samples. MAS experiments of solid inorganic samples can provide information about protonic but also hydridic species. While the MAS NMR signal of protons is expected in the positive range of δ_{iso}, negative values are usually characteristic for hydrides. However, it is reported that NMR signals of hydride compounds can also appear in the range of 0–15 ppm, depending on the metal-hydride distance.[75-76]

^{11}B MAS NMR

Natural boron consists of 20% ^{10}B with a spin of I = 3 and 80% ^{11}B with I = 3/2, which means that both nuclei show quadrupolar interaction.[77] As ^{11}B has a smaller quadrupole moment and a higher abundance and sensitivity, it is usually the preferred isotope for NMR experiments. However, its quadrupolar character significantly influences the shape and position of the resonance lines, making the evaluation of such spectra often not straightforward.[78] But at the same time, the quadrupolar coupling tensor provides information about the electronic environment of the nucleus, which can be extracted with a suitable fit of the respective signal.[79] Therefore, the isotropic chemical shift δ_{iso}, the quadrupole coupling constant C_Q and the asymmetry parameter η_Q can be calculated.[80] As most of the $[BN_2]^{3-}$ anions are linear or just slightly bent, the asymmetry parameter η_Q is expected to be close to zero. However, despite the high number of compounds containing such $[BN_2]^{3-}$ units, only one reported compound was further examined with ^{11}B MAS NMR spectroscopy so far, namely $SrBa_8[BN_2]_6$.[81] Oppositely, compounds containing tetrahedrally or trigonally planar coordinated boron are well studied with MAS NMR spectroscopy.[79]

^{14}N/^{15}N MAS NMR

To further examine the structural motifs in the synthesized compounds, nitrogen MAS NMR would be another analytical method. ^{15}N has a spin of −1/2 and is well suited for NMR investigations, but due to its low natural abundance of just 0.4% a costly isotope modification is necessary, which was beyond the scope of this thesis. ^{14}N, however, has a high abundance but also a spin of 1 and a comparably large quadrupolar moment. Therefore, a distortion of the electronic environment of the nitrogen atom leads to broad doublet resonance lines, whose

acquisition and analysis is not straightforward. However, highly symmetric coordinated nitrides can be investigated with ^{14}N MAS NMR as already shown for ScN and VN.[82] But as the nitride ions in the compounds presented in this thesis are not located in a highly symmetric environment, this method did not provide any reasonable results.

1.3.4 Vibrational Spectroscopy

N–B–N Vibrations

Just as the well-investigated CO_2, triatomic $[A–B–A]^{x-}$ anions are IR and Raman active. Next to the proof of the presence of such structural motifs in the material, vibrational spectroscopy can provide even more information about the respective compound. As its vibrations are sensitive to the chemical environment of the anions, a comparison of the vibrational bands allows to distinguish different structure models, as seen in $Ca_2[BN_2]X$ (X = H, F and Cl) and $Mg_3M[BN_2]N_2$ (M = Al and Ga).[83-86] Following the $3N-5$ and $3N-6$ rule, we expect 4 or 3 vibrational modes for a linear or slightly bent $[AB_2]^{x-}$ anion, respectively. These characteristic and intense vibrations are the symmetrical stretching (ν_1), the anti-symmetrical stretching (ν_2) and the in-plane and out-of-plane bending (ν_3, Figure 1.8). A "free" linear $[A–B–A]^{x-}$ anion has a $D_{\infty h}$ point group symmetry and therefore, ν_1 would be only Raman active and ν_2 as well as the doubly-degenerate ν_3 would be IR active.[83] But as the influence of the surrounding network slightly disturbs the symmetry, some $[AB_2]^{x-}$ units are bent and asymmetric $[A–B–C]^{x-}$ anions show different bond lengths, they have an overall symmetry of C_{2v} or even only C_s, which means that all modes become both IR and Raman active.

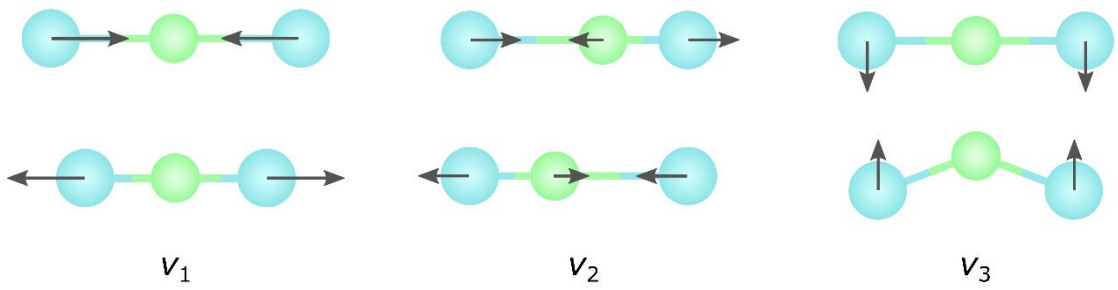

Figure 1.8. Depiction of the different vibrations of a linear $[A–B–A]^{x-}$ anion: symmetrical stretching (ν_1, left), anti-symmetrical stretching (ν_2, middle) and bending (ν_3, right).

Looking at the IR spectrum of a compound containing slightly bent $[BN_2]^{3-}$ units, the anti-symmetrical stretching (ν_2) is usually the strongest vibration (at around 1700 cm^{-1}), since infrared spectroscopy is sensitive to changes in the dipole moment. The bending vibrations (ν_3) usually appear at between 550 and 650 cm^{-1} in the infrared spectrum. Contrary, Raman spectroscopy involves the polarizability of the atoms, which is why the symmetrical stretching (ν_1) appears as the strongest vibrational band at around 1050 cm^{-1}.

Sr/Ba–H and Sr–N Vibrations

Similarly, the hydride and nitride anions show in-plane and out-of-plane vibrations inside the strontium or barium coordination sphere. However, their direct chemical environment can differ significantly and thus the position and intensities of the vibrations vary. Quantum chemical calculations allow to simulate IR and Raman spectra and a comparison to the experimental ones helps to further corroborate the structural analysis of such compounds. Nevertheless, hydride and nitride vibrations appear rather weak compared to the intense N–B–N vibrations.

1.4 Combination of H^-, N^{3-} and $[BN_2]^{3-}$ Anions

No combination of hydride, nitride and nitridoborate anions in one single compound is reported to date. However, the combination of nitrides with either hydrides or nitridoborates already yielded a handful of compounds (Figure 1.9). Nitride hydrides such as Ba_2NH and Ca_2NH convince with hydride ion conductivity, while nitridoborate nitrides, e.g., $Mg_7Si[BN_2]_2N_4$ or $Mg_3Ga[BN_2]N_2$ exhibit intense luminescence upon doping with Eu^{2+}.[25,85-87] A compound containing hydride together with nitridoborate anions is only reported once so far, namely Ca_2BN_2H.[83]

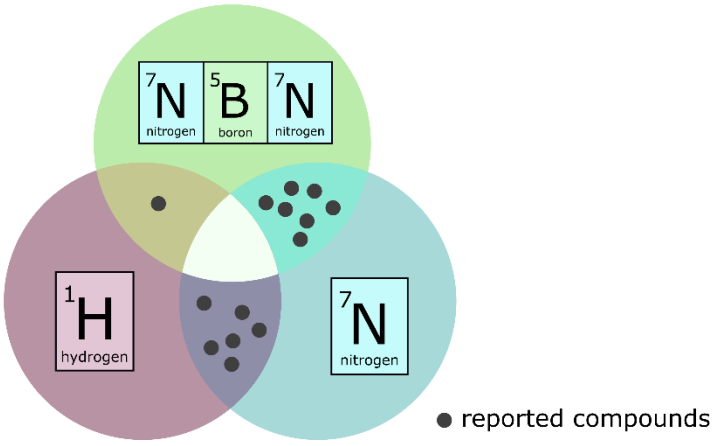

Figure 1.9. Illustration of the overlap of hydride, nitride and nitridoborate anion containing compounds.

Taking a closer look on the synthesis routes of hydride, nitride and nitridoborate containing compounds reveals their differences. Hydrides are mostly known as air and moisture sensitive materials which easily decompose at elevated temperatures. Established synthetic routes for hydridic materials include topotactical or mechanochemical reactions as well as hydrogenation under H_2 atmosphere or pressure.[88] The reactions occur under comparatively mild conditions at low temperatures or even room temperature. To avoid hydrogen loss by diffusion at higher temperatures, suitable crucible materials and high partial pressures are necessary. However, hydrides have a strong reducing power and are easily oxidized when a suitable reactant is present, which restricts the syntheses even more.

In contrast, nitridoborates are known for their high thermal and chemical stability. The most common precursor h-BN is even used as crucible material due to its remarkable stability and inertness. To activate the boron nitride, it is necessary to choose high temperatures, reactive precursors such as azides or subnitrides, or a salt flux.[11] Most syntheses are performed in a classical solid-state ampoule reaction at temperatures of 900 to 1100 °C.

Similarly, nitride compounds are also dominantly formed at elevated temperatures. As discussed in Chapter 1.1, N_2 exhibits a strong triple bond between the nitrogen atoms, necessitating high temperatures or reactive precursors. Next to the direct nitridation with N_2, the ammonia gas flow route at moderate temperatures is also often used for nitride syntheses. Moreover, chemical vapor deposition can be used to achieve thin films or coatings of high purity.

Comparing these distinct synthesis routes (Figure 1.10), it becomes clear why the combination of hydrides, nitrides and nitridoborates remains unexplored. As their synthesis methods are not coinciding – with some exceptions – it is not easy to find a route fitting those building units. However, the synthesis conditions of nitride and hydride compounds as well as those of nitrides and nitridoborates do partially overlap, explaining the presence of such materials.

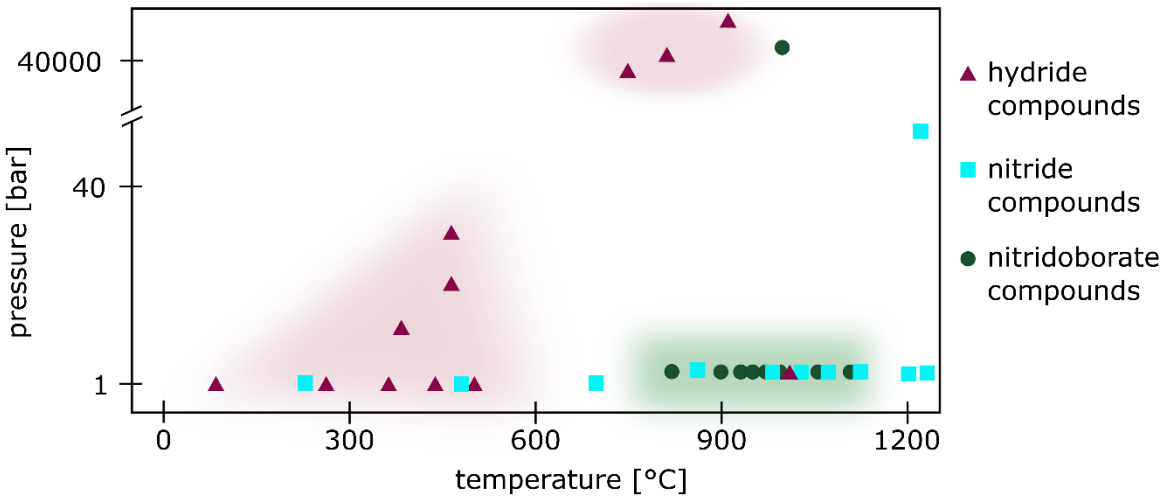

Figure 1.10. Schematic depiction of the different synthesis conditions of nitridoborate and hydride compounds. A full list of all compounds and their syntheses are found in Chapter 8.1.

1.5 Scope of this Thesis

The aim of the present work is the explorative synthesis and characterization of novel materials combining hydride, nitride and nitridoborate anions. Despite such compounds are already very well explored on their own, the research on materials containing two or even all three of these anions is still in its infancy. The fundamental challenge here is to find a suitable synthesis route, which fits the contrasting participants. Expanding the solid-state ampoule reaction – which is well established for nitridoborate and nitride compounds – on hydride precursors in a temperature range of 750 to 950 °C enables the access to such multianionic compounds.

The crystal structures of the new materials in this work were initially solved based on single-crystal X-ray diffraction data. As the hydride ion only has two electrons and therefore a low X-ray scattering power, other techniques are necessary to complete the structural analysis. Rietveld refinement based on neutron powder diffraction of the isotope modified compounds allowed to determine the crystallographic positions of the deuteride/hydride atoms. The resulting partially novel structure types and moieties were characterized and compared to related structures. Additionally, ^{1}H MAS NMR studies supported the presence of anionic hydrogen in the samples and ^{11}B NMR measurements provided further information about the present boron. Infrared and Raman spectroscopy corroborated the structural analysis by examining the characteristic N–B–N, Sr–N and Sr/Ba–H vibrations and electrochemical impedance measurements verified possible hydride ion conductivity. Finally, quantum chemical calculations validated the structure models and vibrational spectra and further investigated the electronic structure of the different compounds.

Within this work, the little-explored class of nitridoborate (nitride) hydrides was investigated thoroughly and expanded by four new compounds with intriguing structures and properties.

1.5 References

[1] H. Kageyama, K. Hayashi, K. Maeda, J. P. Attfield, Z. Hiroi, J. M. Rondinelli, K. R. Poeppelmeier, *Nat. Commun.* **2018**, *9*, 772.

[2] G. Li, Y. Tian, Y. Zhao, J. Lin, *Chem. Soc. Rev.* **2015**, *44*, 8688−8713.

[3] R. Shafei, D. Maganas, P. J. Strobel, P. J. Schmidt, W. Schnick, F. Neese, *J. Am. Chem. Soc.* **2022**, *144*, 8038–8053.

[4] D. Moskovskikh, S. Vorotilo, V. Buinevich, A. Sedegov, K. Kuskov, A. Khort, C. Shuck, M. Zhukovskyi, A. Mukasyan, *Sci. Rep.* **2020**, *10*, 19874.

[5] H. Kageyama, T. Yajima, Y. Tsujimoto, T. Yamamoto, C. Tassel, Y. Kobayashi, *Bull. Chem. Soc. Jpn.* **2019**, *92*, 1349–1357.

[6] A. Fuertes, *Inorg. Chem.* **2006**, *45*, 9640−9642.

[7] C. A. Bridges, G. R. Darling, M. A. Hayward, M. J. Rosseinsky, *J. Am. Chem. Soc.* **2005**, *127*, 5996–6011.

[8] A. J. E. Rowberg, L. Weston, C. G. V. d. Walle, *J. Phys. Chem. C* **2021**, *125*, 2250–2256.

[9] T. Wu, A. Ishikawa, T. Honda, H. Tamatsukuri, K. Ikeda, T. Otomo, S. Matsuishi, *RSC Adv.* **2020**, *9*, 5282–5287.

[10] T. Wu, K. Fujii, T. Murakami, M. Yashima, S. Matsuishi, *Inorg. Chem.* **2020**, *59*, 15384–15393.

[11] R. Pöttgen, O. Reckeweg, *Z. Kristallogr.* **2017**, *232*, 653–668.

[12] J. Liu, X.-B. Li, D. Wang, H. Liu, P. Peng, L.-M. Liu, *J. Mater. Chem. A* **2014**, *2*, 6755–6761.

[13] Y. Kasahara, K. Kuroki, S. Yamanaka, Y. Taguchi, *Phys. C: Supercond.* **2015**, *514*, 354–367.

[14] W. Grochala, *Nat. Chem.* **2015**, *7*, 264.

[15] A. L. Allred, *J. Inorg. Nucl. Chem.* **1961**, *17*, 215–221.

[16] S. Yamaguchi, *Science* **2016**, *351*, 1262–1263.

[17] L. Pauling, *J. Am. Chem. Soc.* **1927**, *49*, 765–790.

[18] R. D. Shannon, *Acta Cryst.* **1976**, *A32*, 751–767.

[19] P. F. Lang, B. C. Smith, *Dalton Trans.* **2010**, *39*, 7786–7791.

[20] A. F. Holleman, N. Wiberg, *Lehrbuch der Anorganischen Chemie*, De Gruyter, Berlin, Germany, **2007**.

[21] C. Janiak, H.-J. Meyer, D. Gudat, R. Alsfasser, E. Riedel, *Moderne Anorganische Chemie*, De Gruyter, Berlin, **2012**.

[22] R. Sato, H. Saitoh, N. Endo, S. Takagi, M. Matsuo, K. Aoki, S.-I. Orimo, *Appl. Phys. Lett.* **2013**, *102*, 091901.

[23] C. Weidenthaler, T. J. Frankcombe, M. Felderhoff, *Inorg. Chem.* **2006**, *45*, 3849−3851.

[24] T. V. Blankenship, X. Wang, C. Hoffmann, S. E. Latturner, *Inorg. Chem.* **2014**, *53*, 10620−10626.

[25] F. Altorfer, W. Bührer, B. Winkler, G. Coddens, R. Essmann, H. Jacobs, *Solid State Ion.* **1994**, *70*, 272−277.

[26] K. Higashi, M. Ochi, Y. Nambu, T. Yamamoto, Taito Murakami, N. Yamashina, C. Tassel, Y. Matsumoto, H. Takatsu, C. M. Brown, H. Kageyama, *Inorg. Chem.* **2021**, *60*, 11957−11963.

[27] A. J. E. Rowberg, C. G. V. d. Walle, *ACS Appl. Energy Mater.* **2021**, *4*, 6348–6355.
[28] K. P. Hilleke, E. Zurek, *Angew. Chem. Int. Ed.* **2022**, *61*, e202207589.
[29] G. Renaudin, L. Guénée, K. Yvon, *J. Alloys Compd.* **2003**, *350*, 145–150.
[30] M. Matsuo, A. Remhof, P. Martelli, R. Caputo, M. Ernst, Y. Miura, T. Sato, H. Oguchi, H. Maekawa, H. Takamura, A. Borgschulte, A. Züttel, S.-I. Orimo, *J. Am. Chem. Soc.* **2009**, *131*, 16389–16391.
[31] C. E. Messer, *J. Solid State Chem.* **1970**, *2*, 144–155.
[32] A. J. Maeland, *Z. Phys. Chem.* **1993**, *179*, 181–185.
[33] N. Kunkel, H. Kohlmann, *J. Phys. Chem. C* **2016**, *120*, 10506−10511.
[34] T. D. Humphries, D. A. Sheppard, M. R. Rowles, M. V. Sofianos, C. E. Buckley, *J. Mater. Chem. A* **2016**, *4*, 12170–12178.
[35] T. Higashi, H. Nishiyama, Y. Pihosh, K. Wakishima, Y. Kawase, Y. Sasaki, A. Nagaoka, K. Yoshino, K. Takanabe, K. Domen, *Phys. Chem. Chem. Phys.* **2023**, *25*, 20737–20748.
[36] J. Musil, P. Zeman, *Solid State Phenom.* **2007**, *127*, 31–36.
[37] C. Jeong-Gil, J. Moon-Ki, C. Saemin, P. Tae-Keun, K. I. Hiun, Y. J. Hyung, P. H. Soo, L. Han-Soo, A. Do-Hee, C. Hongsuk, *Bull. Chem. Soc. Jpn.* **1997**, *70*, 993–996.
[38] P. Pust, P. J. Schmidt, W. Schnick, *Nat. Mater.* **2015**, *14*, 454–458.
[39] X. Zhao, K. J. Range, *J. Alloys Compd.* **2000**, *296*, 72–74.
[40] A. Brager, *Acta Physicochim. URSS* **1937**, *7*, 699–706.
[41] G. A. Jeffrey, G. S. Parry, R. L. Mozzi, *J. Chem. Phys.* **1956**, *25*, 1024–1031.
[42] P. Eckerlin, A. Rabenau, *Z. Anorg. Allg. Chem.* **1960**, *304*, 218–229.
[43] D. Fischer, Z. Cancarevic, J. C. Schön, M. Jansen, *Z. Anorg. Allg. Chem.* **2004**, *630*, 156–160.
[44] J. Hao, Q. L. Cui, G. Zou, J. Liu, X. Li, Y. Li, Q. L. Zhou, D. Iiu, M. Li, F. Li, W. W. Lei, W. Chen, Y. Ma, *Inorg. Chem.* **2009**, *48*, 9737–9741.
[45] E. Zintl, G. Brauer, *Z. Elektrochem. Angew. Phys. Chem.* **1935**, *41*, 102–107.
[46] G. V. M. Vajenine, X. Wang, I. Efthimiopoulos, S. Karmakar, K. Syassen, M. Hanfland, *Phys. Rev. B* **2009**, *79*, 224107.
[47] P. Villars, K. Cenzual, *Pearson's Crystal Data - Crystal Structure Database for Inorganic Compounds*, ASM International, Ohio, **2017**.
[48] N. Ooi, V. Rajan, J. Gottlieb, Y. Catherine, J. B. Adams, *Modelling Simul. Mater. Sci. Eng.* **2006**, *15*, 515–535.
[49] M. Orth, R.-D. Hoffmann, R. Pöttgen, W. Schnick, *Chem. Eur. J.* **2001**, *7*, 2791–2797.
[50] S. Vogel, A. T. Buda, W. Schnick, *Angew. Chem. Int. Ed.* **2018**, *57*, 13202−13205.
[51] H. Jing, H.-J. Meyer, *Z. Anorg. Allg. Chem.* **1999**, *626*, 514–517.
[52] M. Orth, W. Schnick, *Z. Anorg. Allg. Chem.* **1999**, *625*, 551–554.
[53] J. Goubeau, W. Anselment, *Z. Anorg. Allg. Chem.* **1961**, *310*, 248–260.
[54] M. Somer, M. N. Kütükcü, R. C. Gil, H. Borrmann, W. Carrillo-Cabrera, *Z. Anorg. Allg. Chem.* **2004**, *630*, 1015–1021.
[55] M. Somer, U. Herterich, J. Curda, K. Peters, H. G. v. Schnering, *Z. Kristallogr.* **1994**, *209*, 182.
[56] O. Reckeweg, F. J. DiSalvo, M. Somer, *J. Alloys Compd.* **2003**, *361*, 102–107.

[57] R. Czekalla, W. Jeitschko, R.-D. Hoffmann, H. Rabeneck, *Z. Naturforsch.* **1996**, *51b*, 646–654.
[58] H. Womelsdorf, H.-J. Meyer, *Z. Anorg. Allg. Chem.* **1994**, *620*, 258–261.
[59] H.-J. Meyer, *Z. Anorg. Allg. Chem.* **1991**, *594*, 113–118.
[60] M. Wörle, H. M. z. Altenschildesche, R. Nesper, *J. Alloys Compd.* **1998**, *264*, 107–114.
[61] T. V. Blankenship, M. J. Dickman, L. J. v. d. Burgt, S. E. Latturner, *Inorg. Chem.* **2015**, *54*, 914−921.
[62] H.-J. Meyer, *Z. Anorg. Allg. Chem.* **1991**, *593*, 186–192.
[63] H.-G. v. Schnering, M. Somer, M. Hartweg, K. Peters, *Angew. Chem. Int. Ed.* **1990**, *29*, 65–67.
[64] Y. V. Guk, M. A. Ilyushin, E. L. Golod, B. V. Gidaspov, *Russ. Chem. Rev.* **1983**, *52*, 284–297.
[65] N. Z. Ali, J. Nuss, M. Jansen, *Z. Anorg. Allg. Chem.* **2011**, *637*, 183–185.
[66] K. Duris, U. Müller, M. Jansen, *Z. Anorg. Allg. Chem.* **2012**, *638*, 737–743.
[67] J. Curda, W. Klein, M. Jansen, *J. Solid State Chem.* **2001**, *162*, 220–224.
[68] A. M. Abakumov, V. L. Aksenov, V. A. Alyoshin, E. V. Antipov, A. M. Balagurov, D. A. Mikhailova, S. N. Putilin, M. G. Rozova, *Phys. Rev. Lett.* **1998**, *80*, 385–388.
[69] E. Prince, *International Tables for Crystallography, Volume C*, Wiley-VCH, New Jersey, **2006**.
[70] W. I. F. David, K. Shankland, L. B. McCusker, C. Baerlocher, *Structure Determination from Powder Diffraction Data*, University Press, Oxford, **2002**.
[71] V. F. Sears, *Neutron News* **1992**, *3*, 26–37.
[72] A. Taylor, M. Dunne, S. Bennington, S. Ansell, I. Gardner, P. Norreys, T. Broome, D. Findlay, R. Nelmes, *Science* **2007**, *315*, 1092–1095.
[73] W. M. Stacey, *Nuclear Reactor Physics*, Wiley-VCH, New Jersey, **2018**.
[74] M. Arai, K. Crawford, *Neutron Sources and Facilities*, Springer, Boston, **2009**.
[75] K. Hayashi, P. V. Sushko, Y. Hashimoto, A. L. Shluger, H. Hosono, *Nat. Commun.* **2014**, *5*, 3515.
[76] A. Mutschke, G. M. Bernard, M. Bertmer, A. J. Karttunen, C. Ritter, V. K. Michaelis, N. Kunkel, *Angew. Chem. Int. Ed.* **2021**, *60*, 5683–5687.
[77] R. K. Harris, E. D. Becker, S. M. C. D. Menezes, R. Goodfellow, P. Granger, *Pure Appl. Chem.* **2001**, *73*, 1795–1818.
[78] Y.-T. A. Wong, D. L. Bryce, *Annu. Rep. NMR Spectrosc.* **2018**, *93*, 213–279.
[79] T. Bräuniger, M. Jansen, *Z. Anorg. Allg. Chem.* **2013**, *639*, 857–879.
[80] D. Massiot, F. Fayon, M. Capron, I. King, S. L. Calvé, B. Alonso, J. O. Durand, B. Bujoli, Z. Gan, G. Hoatson, *Magn. Reson. Chem.* **2002**, *40*, 70–76.
[81] S. Seidel, T. Dierkes, T. Jüstel, C. Benndorf, H. Eckert, R. Pöttgen, *Dalton Trans.* **2016**, *45*, 12078–12086.
[82] J. Steinadler, L. Eisenburger, T. Bräuniger, *Z. Anorg. Allg. Chem.* **2022**, *648*, e202200201.
[83] M. Somer, Ö. Yaren, O. Reckeweg, Y. Prots, W. Carrillo-Cabrera, *Z. Anorg. Allg. Chem.* **2004**, *630*, 1068–1073.
[84] F. Rohrer, R. Nesper, *J. Solid State Chem.* **1998**, *135*, 194–200.

[85] M. Ströbele, K. Dolabdjian, D. Enseling, D. Dutczak, B. Mihailova, T. Jüstel, H.-J. Meyer, *Eur. J. Inorg. Chem.* **2015**, *10*, 1716–1725.

[86] D. Dutczak, K. M. Wurst, M. Ströbele, D. Enseling, T. Jüstel, H.-J. Meyer, *Eur. J. Inorg. Chem.* **2016**, *6*, 861–866.

[87] G. J. Irvine, R. I. Smith, M. O. Jones, J. T. S. Irvine, *Nat. Commun.* **2023**, *14*, 4389.

[88] A. Mutschke, *Dissertation*, TU Munich, **2022**.

2 Strontium Nitridoborate Hydride Sr_2BN_2H Verified by Single-Crystal X-ray and Neutron Powder Diffraction

Published in: *Inorg. Chem.* **2022**, *61*, 12685–12691

Authors: Sophia L. Wandelt, Ayla Karnas, Alexander Mutschke, Nathalie Kunkel, Clemens Ritter, and Wolfgang Schnick

DOI: https://doi.org/10.1021/acs.inorgchem.2c01688

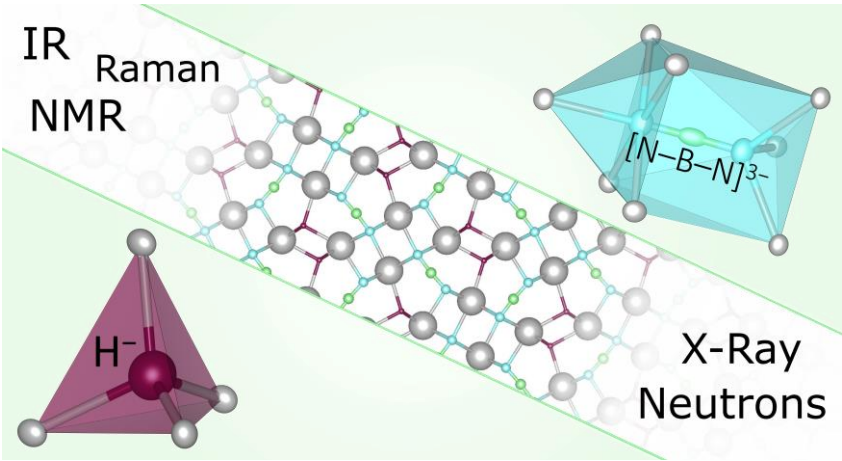

Abstract. Combining different anions in one material allows tuning of its structural, magnetic, and electronic properties. We hereby present the mixed anion compound Sr_2BN_2H, expanding the less-known class of nitridoborate hydrides. Solid-state reaction of Sr_2N, BN, and SrH_2 at 850 °C in a tube furnace yielded a gray, air- and moisture-sensitive powder of Sr_2BN_2H. It crystallizes as colorless platelets in the orthorhombic space group *Pnma* (no. 62) with a = 9.9164(2), b = 3.9079(1), and c = 10.1723(2) Å and Z = 4. An initial structural model was obtained from single-crystal X-ray diffraction data and corroborated by neutron powder diffraction data of the corresponding deuteride. Further validation by ^{1}H and ^{11}B MAS NMR, FTIR, and Raman spectroscopy complements the structural proof of anionic hydrogen present in the compound. Quantum chemical calculations support the experimental findings and reveal the electronic structure of Sr_2BN_2H.

2.1 Introduction

Combining multiple anions within one compound precedes as an alternative approach to modify the physical, optical, magnetic, and electronic properties of an inorganic material.[1–3] The traditional multiple cation approach already proved itself as a powerful tool of host compound tuning, for example, controlling the emission wavelength of luminescent materials.[4–6] Similarly, the combination of multiple anions with their different polarizabilities, ionic radii, coordination geometries, and electronegativities opens up a variety of new compound classes with a promising scope of diverse applications.[7,8] Single-atom anions (e.g., H^-, F^-, O^{2-}, or N^{3-}) as well as molecular anions (e.g., BH_4^-, CBN^{4-}, BN_2^{3-}, NH^{2-}, or SO_4^{2-}) have been observed isolated in manifold minerals or synthetic materials, but their combination has not gained much attention so far. Acknowledging this concept with several known compounds, oxide hydrides, nitride hydrides, and oxide fluorides are just three examples for functional mixed anionic species.[9–12] Facing the synthesis of such materials, some hurdles have to be crossed. The common synthesis routes vary notably from moderate temperatures and ambient pressure for sensitive anion-containing compounds (e.g., H^-, NH^{2-}, or BH_4^-) to high-temperature and high-pressure conditions for stable anion-containing compounds (e.g., O^{2-}, N^{3-}, or BN_2^{3-}).[13–15] To unify these stability and reactivity contrasts, appropriate precursors and synthesis routes have to be developed. One of these challenging anion combinations is set within nitridoborate hydrides. Numerous combinations of either hydrides or nitridoborates with other anions are known, but for the combination of these two, only one representative has been reported in literature so far, namely, Ca_2BN_2H.[16] The field of hydride research has attracted much attention over the last decade, revealing intriguing materials such as hydride ion conductors or even host lattices for Eu^{2+} luminescence.[17,18] Comparing the ionic radii and structural features, hydrides are closely related to fluorides.[19] Considering the number of known compounds in each class, fluorides clearly outnumber hydrides due to their higher stability and easier accessible synthesis routes. Hydridic materials mostly decompose at elevated temperatures, and hydrogen tends to diffuse through various materials, which profoundly complicates the synthesis of hydride species. Contrarily, nitridoborate compounds are convincing with their high stability and wide range of synthesis conditions.[20] Nitridoborates arise as substructures of h-BN and often appear as a linear or slightly bent $[N–B–N]^{3-}$ anion. Under more extreme synthesis conditions, other structural motifs such as BN_3^{6-}, $B_2N_4^{8-}$, or $B_3N_6^{9-}$ are observable.[20] Isoelectronic to CO_2, BN_2^{3-} and its close relative CBN^{4-} are suitable building units for inorganic compounds, building up a

large variety of crystal structures.[21] Despite their substantially different synthesis routes, hydride and nitridoborate anions can be combined within one compound through sensibly chosen precursors and reaction conditions.

In this contribution, we present the nitridoborate hydride Sr_2BN_2H, accessible by solid−state reaction of the corresponding nitrides and hydride. The crystal structure was elucidated from X-ray single-crystal data and neutron powder diffraction. Additionally, magic angle spinning (MAS) NMR and vibrational spectroscopy confirm the hydridic character, providing a full analytical and structural proof of hydride anions in our compound.

2.2 Results and Discussion

2.2.1 Synthesis

Sr_2BN_2H was obtained as a colorless crystalline powder, which is sensitive toward air and moisture. Isolated single crystals exhibit a platelet-like shape up to 70 µm in length (Figure 2.1, left). Minor amorphous black impurities presumably arising from the Ta ampule cause a gray body color of the bulk sample. Rietveld refinement based on the powder XRD data shows the phase composition of the bulk material (Figure 2.1, right), where small amounts of SrH_2, SrO, and $Sr_3B_2N_4$ were observed as byproducts (data of Rietveld refinement are listed in Table S2.1 in Chapter 8.2). Varying the precursor stoichiometry and temperature (750−950 °C) revealed a substantial variability for the synthesis of Sr_2BN_2H but did not lead to a higher yield of the product.

2.2.2 Structure Determination

XRD data of a single crystal led to a first structure model for Sr_2BN_2H. The crystal structure was partially solved in the orthorhombic space group *Pnma* (no. 62, Table 2.1), refining only Sr, B, and N due to the low X-ray scattering power of hydrogen. Neutron powder diffraction measurements were performed to determine the hydride atomic positions within the structure. As ^1H shows intense incoherent scattering, a deuterated sample was necessary to obtain reliable data (coherent scattering lengths $b_c(H) = -3.7$ fm; $b_c(D) = 6.7$ fm).[22] Additionally, the precursors were enriched with ^{11}B to avoid neutron absorption of ^{10}B, which is present in the natural isotope mixture of boron. Figure S2.1 in the Appendix shows the phase composition of the bulk sample prepared for neutron experiments determined by Rietveld refinement based on powder XRD

data (data for the refinement are found in Table S2.2); similar to Sr_2BN_2H, some minor byproducts [SrO (7.4(2) wt %), $Sr_3{}^{11}B_2N_4$ (6.4(3) wt %), and SrD_2 (6.3(4) wt %)] were observed.

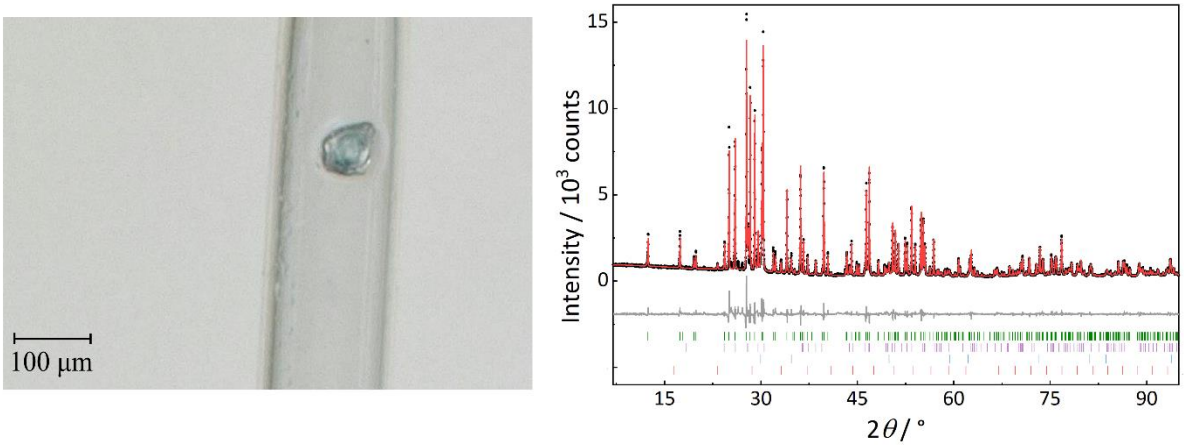

Figure 2.1. Optical micrograph of a single crystal of Sr_2BN_2H with dimensions of 68 × 64 µm^2 in an Ar-filled glass capillary (left). Rietveld refinement of Sr_2BN_2H based on powder XRD data of the bulk sample at ambient temperature with Cu-Kα_1 radiation (λ = 1.5406 Å, right). The black, red, and gray lines mark the experimental and calculated data and their difference, respectively. The Bragg markers indicate from top to bottom Sr_2BN_2H [86.9(1) wt %], SrH_2 [8.5(1) wt %], SrO [2.8(1) wt %], and $Sr_3B_2N_4$ [1.9(1) wt %].

Rietveld refinement based on the neutron powder diffractogram (Table 2.1, Figure 2.2) confirmed the proposed structure model and revealed the deuteride anions on a fully occupied Wyckoff position 4*c*. Minor impurities of hydrogen in the synthesized ^{11}BN (elemental analysis report is shown in Figure S2.2) impeded the full deuteration of the compound, and the refinement led to the sum formula $Sr_2{}^{11}BN_2D_{0.86}H_{0.14}$. As a mixed occupation of H and D (14%:86%) and a partially filled deuterium site with 22% vacancies result in an identical scattering length of 5.18 fm, the refinement alone cannot disclose the occupation on this crystallographic position. To prove our thesis of a mixed occupation, other analytics have to be taken into account. Infrared spectroscopy of the sample (Figure S2.3) shows weak hydrogen and strong deuterium vibrations with an expected shift of √2 due to the different atomic weights. ^{1}H MAS NMR data (Figure S2.4) show a sharp signal at 5.8 ppm identical to Sr_2BN_2H (Figure 2.4), confirming the presence of hydrogen in the sample. Considering charge balance and infrared and NMR data, a partially filled deuterium site seems highly unlikely. Due to the larger mass and therefore less pronounced vibrations of deuterium, $Sr_2{}^{11}BN_2D_{0.86}H_{0.14}$ has slightly smaller lattice parameters compared to Sr_2BN_2H. Moreover, the neutron data exclude any presence of oxygen

on the nitrogen positions as their coherent scattering lengths differ significantly [b_c(O) = 5.8 fm, b_c(N) = 9.4 fm].[22] Minor SrO impurities in the bulk sample remain from the synthesis of the precursor SrD_2. The atomic positions and displacement parameters of both single-crystal X-ray and neutron powder diffraction data refinement can be found in Tables S2.3 and S2.4.

Table 2.1. Crystallographic data for the single-crystal XRD refinement and Rietveld refinement based on neutron powder diffraction data of Sr_2BN_2H and $Sr_2{}^{11}BN_2D_{0.86}H_{0.14}$, respectively.

formula	**Sr_2BN_2H**	**$Sr_2{}^{11}BN_2D_{0.86}H_{0.14}$**
formula mass / g·mol^{-1}	215.08	216.28
space group	*Pnma* (no. 62)	
lattice parameters / Å	a = 9.9164(2)	a = 9.8978(4)
	b = 3.9079(1)	b = 3.9041(1)
	c = 10.1723(2)	c = 10.1569(4)
cell volume / Å^3	394.20(2)	392.48(2)
formula units / cell	4	
calculated density / g·cm^{-3}	3.624	3.643
diffractometer	Bruker D8 Venture	ILL, D20
radiation, λ / Å	Mo-$K\alpha$, 0.709	neutrons, 1.54
temperature / K	293	300
θ range / °	2.9–39	9–150
refined parameters	34	49
GoF	1.089	2.147
R indices	$R1$ ($I \geq 2\sigma(I)$) = 0.0152	R_p = 0.0139
	$wR2$ ($I \geq 2\sigma(I)$) = 0.0305	R_{wp} = 0.0192
	$R1$ (all data) = 0.0193	R_{exp} = 0.0089
	$wR2$ (all data) = 0.0310	R_{Bragg} = 0.0110

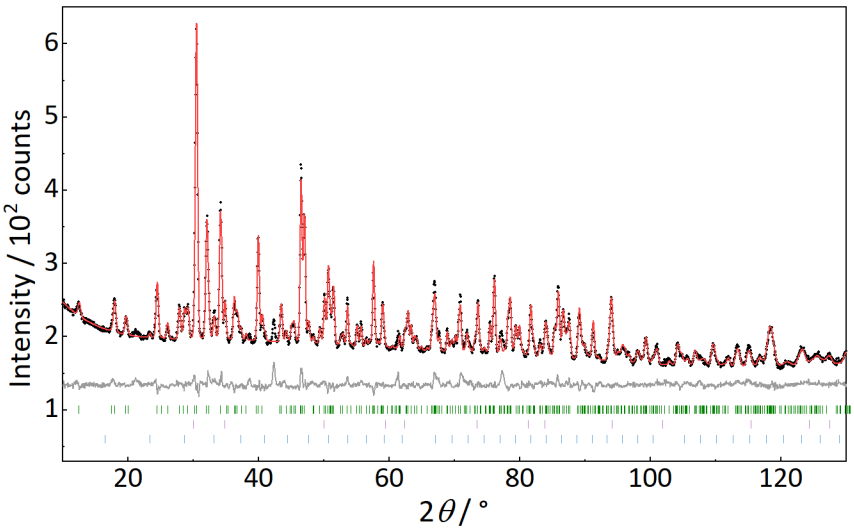

Figure 2.2. Rietveld refinement of $Sr_2{}^{11}BN_2D_{0.86}H_{0.14}$ based on constant wavelength neutron powder diffraction data (λ = 1.54 Å) of the bulk sample. The graph displays the experimental, calculated, and difference data in black, red, and gray, respectively. The Bragg markers indicate the main compound $Sr_2{}^{11}BN_2D_{0.86}H_{0.14}$ [86.9(3) wt %] and the byproducts SrO [7.0(3) wt %] and $Sr_3{}^{11}B_2N_4$ [6.1(2) wt %], from top to bottom.

2.2.3 Structure Description

Sr_2BN_2H crystallizes isotypically to Sr_2BN_2F and exhibits BN_2^{3-} units and anionic hydrogen coordinated to strontium atoms (Figure 2.3a).[23] N1 of the BN_2^{3-} units is coordinated in a distorted quadratic bipyramid, whereas N2 is distorted tetrahedrally coordinated by the corresponding B and Sr atoms (Figure 2.3b). In the voids of this network of edge-sharing $[BN_2^{3-}]Sr_8$ polyhedra, the distorted tetrahedrally coordinated hydrides build edge-sharing strands running along [010] (Figure 2.3c,d). The BN_2^{3-} units are slightly bent with an N–B–N angle of 174.9(3)° and show B–N distances of 1.325(4)–1.350(4) Å, which are in good agreement with literature values.[16,24] Sr–H [2.453(8)–2.568(8) Å] and Sr–N [2.561(3)–2.764(2) Å] bond lengths are also in a typical range for known strontium nitrides or hydrides.[23,25,26] All bond lengths are listed in Table S2.5 in the Appendix. Sr_2BN_2H was found to crystallize in the Sr_2BN_2F structure type following the calcium analogue Ca_2BN_2H and its corresponding fluoride Ca_2BN_2F.[16,23] This acknowledges the often observed analogy between hydrides and fluorides regarding their similar ionic radii.[19]

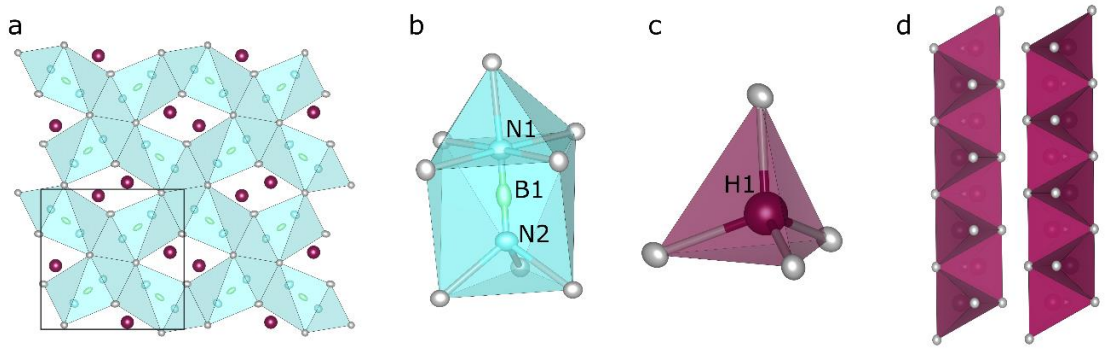

Figure 2.3. (a) The crystal structure of Sr_2BN_2H exhibits BN_2^{3-} units coordinated by strontium with the hydride anions in the voids, viewed along [010]. (b) Coordination polyhedron of a BN_2^{3-} unit. (c) HSr_4 tetrahedron. (d) Edge-sharing HSr_4 tetrahedra strands running along [010]. All ellipsoids are displayed at a 95% probability level, Sr atoms in gray, N atoms in blue, B atoms in green, H atoms, HSr_4 tetrahedra in purple, and $[BN_2^{3-}]Sr_8$ polyhedra in blue.

2.2.4 MAS NMR

^{1}H MAS NMR measurements (Figure 2.4, left) show one comparatively narrow signal at 5.8 ppm; the small shoulder around 1.9 ppm can be attributed to minor impurities. The chemical shift of the signal to a lower magnetic field validates the anionic character of the hydrogen present in the sample, as already shown in other hydride species.[27–29] The boron isotope ^{11}B has spin I = 3/2 and hence possesses a quadrupole moment.[30,31] Consequently, the ^{11}B NMR spectrum acquired under MAS shows a second-order broadened signal of the central transition, centered at about 13 ppm (Figure 2.4, right). Compared to literature, the shape and chemical shifts of the signal are in agreement with those of other known nitridoborates such as $Ca_3B_2N_4$.[21]

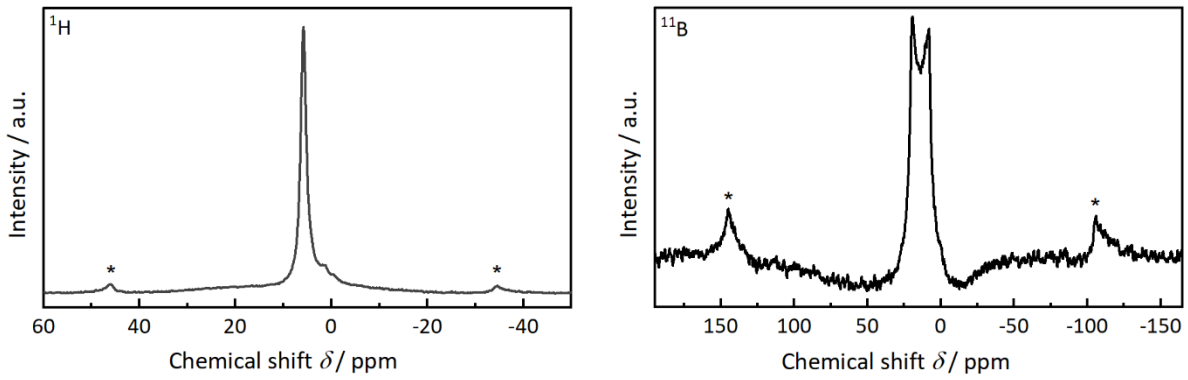

Figure 2.4. ^{1}H (left) and ^{11}B (right) MAS NMR spectra of Sr_2BN_2H; both show one strong signal corresponding to one crystallographic site of hydrogen and boron, respectively. The spinning sidebands are marked with an asterisk.

2.2.5 Vibrational Spectroscopy

As both hydride and nitridoborate anions can show IR and Raman active modes, vibrational spectroscopy is another suitable technique to validate the proposed structure model of Sr_2BN_2H and prove the hydride abundance. The FTIR spectrum (Figure 2.5, left) shows two bands at 728 and 928 cm^{-1} for the hydride out-of-plane and in-plane vibrations (referring to the plane described by Sr atoms) and two bands at 598 and 1664 cm^{-1} for the B–N bending and antisymmetrical stretching, respectively. Compared to the simulated data, the experimental spectrum matches as predicted, and the observed bands of the B–N vibrations are in good agreement with the reported IR pattern of the isostructural Ca_2BN_2H and Sr_2BN_2F.[16,23] Additionally, we can exclude any NH^- or OH^- species, as there are no signals in the region of 3600–3200 cm^{-1} visible (Figure S2.5 in the Appendix). The weak bands marked with an asterisk are from the IR and Raman active byproduct $Sr_3B_2N_4$. Due to the different coordination environment of the BN_2^{3-} unit, the bands are shifted to higher wavenumbers compared to Sr_2BN_2H.

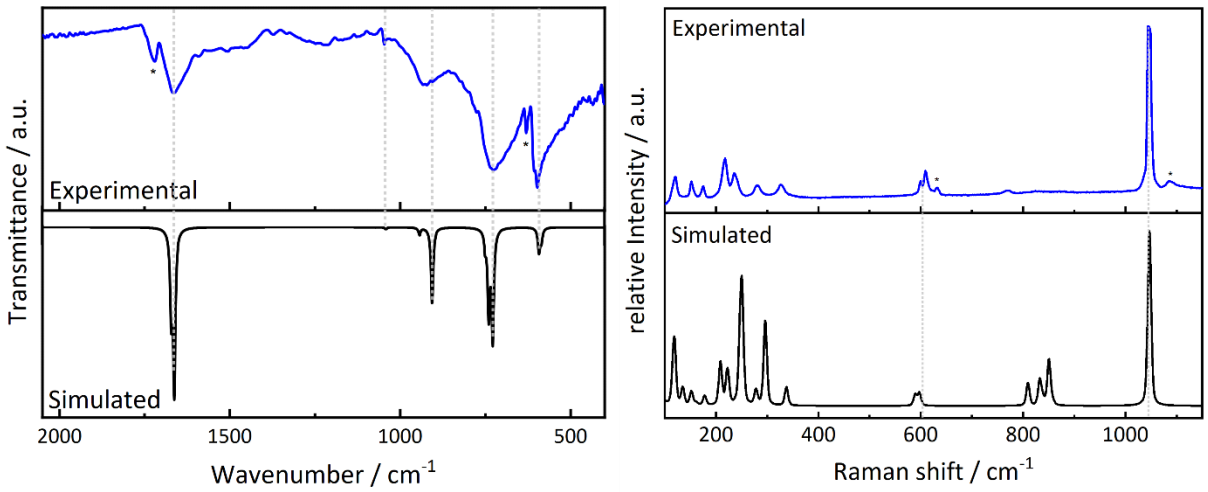

Figure 2.5. Experimental (top) and simulated (DFT-PBE0, bottom) FTIR (left) and Raman (right) spectra of Sr_2BN_2H. Signals arising from the byproduct $Sr_3B_2N_4$ are marked with an asterisk.

The Raman spectrum exhibits one strong and two weaker signals at 1045 and 600–610 cm^{-1}, which arise from symmetric B–N stretching and bending (Figure 2.5, right). In the region of 100–340 cm^{-1}, the lattice and hydride vibrations are detectable. Compared to the simulated spectrum, the observed bands are again in good agreement with the theoretical data. However, the intensity of the vibrations below 400 nm are overestimated in the simulated spectrum.

Furthermore, the hydride vibrations at 800 nm appear rather broad and unresolved compared to the simulated spectrum. B–N vibrations of the byproduct $Sr_3B_2N_4$ cause the diminished signals marked with an asterisk. The separate vibrations of both IR and Raman spectra can be assigned by quantum chemical calculations and are resolved further in Tables S2.6 and S2.7 in the Appendix.

2.2.6 Quantum Chemical Calculations

Quantum chemical calculations were conducted to validate the structure model and further analyze the electronic properties of our compound. After optimizing the crystal structure at the DFT-PBE0 level of theory, our model of Sr_2BN_2H confirmed to be a true local minimum with no imaginary frequencies. The optimized lattice parameters *a*, *b*, and *c* differ by −0.8, −0.3, and +0.6%, respectively, compared to the experimental data. Calculations of the electronic band structure (Figure 2.6, left) reveal an indirect band gap of 5.0 eV, resulting in Sr_2BN_2H being a colorless and transparent insulator. Analyzing the projected density of states (Figure 2.6, right), nitrogen appears as the topmost valence bands. Contrary to other known mixed anionic hydride compounds, the steep hydrogen bands emerge at lower energies, which might be due to its lower polarizability compared to the highly anionic nitride ions (N^{3-}).[32,33]

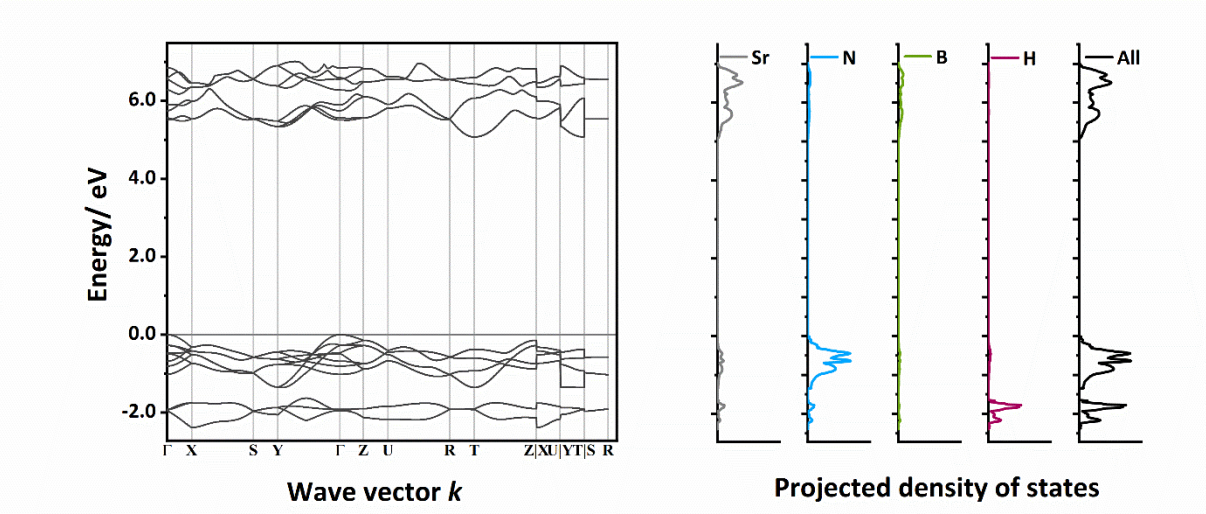

Figure 2.6. Electronic band structure (left) and projected density of states (right) of Sr_2BN_2H calculated at the DFT-PBE0/TZVP level of theory, predicting an indirect band gap of 5.0 eV.

2.3 Conclusion

Herein, we present the strontium nitridoborate hydride Sr_2BN_2H accessed by the solid−state reaction of the corresponding binary nitrides and hydride, facing the challenge of combining sensitive hydride and highly stable nitridoborate anions within one material. We provide a full analytical and structural proof of the hydride presence in Sr_2BN_2H. Neutron powder diffraction data in addition to single-crystal XRD data revealed the crystal structure in the orthorhombic space group *Pnma* (no. 62); distorted tetrahedrally coordinated hydrides are located in the voids of a network of slightly bent $[N–B–N]^{3-}$ units connected by strontium atoms. MAS NMR and vibrational spectroscopy further validate the hydride species in our compound. Quantum chemical calculations supported the experimental findings and stated nitrogen being at the topmost valence bands of the electronic band structure, contrary to most of the known hydridic compounds. Sr_2BN_2H was found to be isotypic to Sr_2BN_2F and Ca_2BN_2X (X = H, F), which again confirms the often-observed fluoride−hydride analogy. Keeping the high number of fluoride compounds in mind, the class of hydride analogues bears a promising potential of new functional materials.

2.4 Experimental Part

2.4.1 Synthesis

Sr_2BN_2H and isotypic $Sr_2{}^{11}BN_2D_{0.86}H_{0.14}$ were synthesized by the solid−state reaction of Sr_2N, BN (^{11}BN) and SrH_2 (SrD_2). Because of the air and moisture sensitivity of the starting materials as well as the products, all experiments were performed in Ar-filled gloveboxes (Unilab, MBraun, Garching, O_2 < 1 ppm, H_2O < 1 ppm). For the synthesis of Sr_2N, granulated Sr metal (Sigma-Aldrich, 99.99%) was heated in a radio frequency furnace (IG 10/600; Hüttinger Elektronik Freiburg, Germany) at 1000 °C for 24 h under a nitrogen atmosphere according to DiSalvo et al. but at a higher temperature.[34] BN and ^{11}BN were synthesized in an NH_3 (Airliquide, 99.999%) gas flow reaction at 800 °C starting from H_3BO_3 (Sigma-Aldrich, ≥ 99%) and $H_3{}^{11}BO_3$ (Sigma-Aldrich, ≥ 99%), respectively, using 1 equiv. of $CO(NH_2)_2$ (Sigma-Aldrich, >99.5%) as a catalyst.[35] SrH_2 and SrD_2 were prepared from Sr metal (Sigma-Aldrich, 99.99%) in an autoclave reaction under H_2 (Westfalen AG, 99.9%) or D_2 (Airliquide, 99.8%) at 60 bar and 450 °C for 15 h.[32] The purity of all starting materials was analyzed using powder X-ray diffraction. To synthesize Sr_2BN_2H, stoichiometric amounts of Sr_2N (31.2 mg, 0.17 mmol), SrH_2 (14.8 mg, 0.17 mmol), and BN (4.09 mg, 0.17 mmol) were ground in an agate mortar and filled into a tantalum ampule. For

$Sr_2{}^{11}BN_2D_{0.86}H_{0.14}$, Sr_2N (30.2 mg, 0.16 mmol), SrD_2 (14.3 mg, 0.16 mmol), and a slight excess of ^{11}BN (5.54 mg, 0.22 mmol) were used as precursors. The ampoules were welded shut in an arc furnace under water cooling to avoid uncontrolled reaction and then placed in a silica tube. The tube was filled with argon and then heated to 850 °C within 3 h in a tube furnace (Carbolite Gero, Neuhausen, Germany). After maintaining this temperature for 15 h, the furnace was cooled down to 300 °C in 9 h and then quenched to room temperature by switching it off. Sr_2BN_2H and $Sr_2{}^{11}BN_2D_{0.86}H_{0.14}$ were both obtained as gray crystalline powders, which are sensitive to air and moisture and were stored in a glovebox for all further analyses.

2.4.2 Single-Crystal XRD

A single crystal of Sr_2BN_2H was isolated under a microscope in a glovebox and transferred into a glass capillary, which was subsequently sealed airtight. The XRD data were obtained using a Bruker D8 VENTURE diffractometer with a rotating anode and Mo-Kα radiation. For integration and absorption correction of the data, the program package APEX3 was used.[36,37] The structure solution was performed with direct methods (SHELXS), whereas the structure refinement was conducted using the full-matrix least-squares methods (SHELXL).[38,39] For visualization of the crystal structure, VESTA3 was used.[40]

2.4.3 Powder XRD

The Sr_2BN_2H bulk sample was ground in an agate mortar and transferred into a glass capillary, which was sealed under an argon atmosphere. Powder XRD data were obtained using a STOE Stadi P diffractometer with Cu-Kα_1 radiation, a Ge(111) monochromator, and a Mythen1K detector in Debye–Scherrer geometry. For Rietveld refinements, the TOPAS6 package with a fundamental parameter approach (convoluting source emission profile, axial instruments' contributions, microstrain effects, and crystallite size) was used.[41,42] A capillary absorption correction was conducted, and the background was refined with a shifted Chebychev function.[34]

2.4.4 Neutron Powder Diffraction

About 150 mg of $Sr_2{}^{11}BN_2D_{0.86}H_{0.14}$ was transferred into a vanadium cylinder and sealed airtight. Neutron powder diffraction data of the sample were obtained from the high-intensity two-axis

diffractometer D20 at the Institute Laue-Langevin, Grenoble, using the high take-off angle of 90° and a constant wavelength of 1.54 Å. TOPAS6 was used for Rietveld refinement, where a shifted Chebychev function was used for the background, and the peak shape was modeled with a Thompson Cox Hastings function.[42,44] For the refinement, a scattering length of 6.65(4) fm was used for ^{11}B.[22]

2.4.5 MAS NMR

Solid-state MAS NMR measurements of ^{1}H and ^{11}B were performed using a 2.5 mm ZrO_2 rotor with a Bruker 500 AVANCE-III spectrometer operating at 500.2 MHz. The spectra were acquired at a spinning frequency of 20 kHz with a 2.5 µs 90° pulse. The chemical shift was referenced with respect to TMS (δ = 0 ppm).

2.4.6 FTIR Spectroscopy

Infrared spectra of the hydride and the deuteride samples were obtained using a Bruker Alpha-P FTIR spectrometer with an attenuated total reflectance unit. The spectra were recorded in the range of 450−4000 cm^{-1} with a resolution of 2 cm^{-1}. Due to the air and moisture sensitivity of the samples, the spectrometer was operated under an argon atmosphere.

2.4.7 Raman Spectroscopy

Raman spectra of both compounds were measured in sealed glass capillaries with a Renishaw inVia Reflex Raman System in the range of 100−1200 cm^{-1} using a charge-coupled device detector and a laser with a wavelength of λ = 532 nm.

2.4.8 Quantum Chemical Calculations

The geometric, electronic, and vibrational properties were studied using the CRYSTAL17 program package.[45] The PBE0 hybrid functional method with Gaussian-type basis sets was used.[46,47] The basis sets for Sr, N, B, and H were previously derived from the Karlsruhe def2 basis sets.[48] Triple valence polarized basis sets were used for N, B, and H[32,49] and the split valence basis set for Sr.[49,50] The reciprocal space was sampled using a Monkhorst-type 3×8×4 k-mesh.[51] Tightened tolerance factors (TOLINTEG) of 8, 8, 8, 8, and 16 were used for the evaluation of the exchange and Coulomb integrals. For the geometry optimization, the lattice

parameters and atomic positions were fully optimized within the constraints of the space group symmetry. The reciprocal band paths have been determined by the Seek-path web service.[52,53] Harmonic frequencies and Raman and FTIR intensities were simulated by computational schemes implemented within the CRYSTAL17 program package.[54–56] For the simulation of the FTIR and Raman spectra, a pseudo-Voigt function (50:50–Lorentzian/ Gaussian) with a full width at half-maximum of 8 cm^{-1} was used as the profile function. To compensate for overestimation of the harmonic frequencies calculations, the simulated infrared spectrum was shifted by a factor of 0.96.[57] The temperature and wavelength of the Raman laser were set according to the experimental setup.

2.5 Acknowledgements

The authors gratefully acknowledge the ILL Grenoble for granting beamtime (Proposal no. 86528) and Christian Minke and Dr. Thomas Bräuniger (both at the Department of Chemistry, LMU Munich) for NMR measurements as well as financial support by the Fonds der Chemischen Industrie (FCI).

2.6 References

[1] H. Kageyama, K. Hayashi, K. Maeda, J. P. Attfield, Z. Hiroi, J. M. Rondinelli, K. R. Poeppelmeier, *Nat. Commun.* **2018**, *9*, 772.

[2] K. Maeda, F. Takeiri, G. Kobayashi, S. Matsuishi, H. Ogino, S. Ida, T. Mori, Y. Uchimoto, S. Tanabe, T. Hasegawa, N. Imanaka, H. Kageyama, *Bull. Chem. Soc. Jpn.* **2021**, *95*, 26–37.

[3] G. D. Park, J.-S. Park, J. K. Kim, Y. C. Kang, *Adv. Energy Mater.* **2021**, *11*, 2003058.

[4] L. Wang, R.-J. Xie, T. Suehiro, T. Takeda, N. Hirosaki, *Chem. Rev.* **2018**, *118*, 1951−2009.

[5] G. Li, Y. Tian, Y. Zhao, J. Lin, *Chem. Soc. Rev.* **2015**, *44*, 8688−8713.

[6] R. Shafei, D. Maganas, P. J. Strobel, P. J. Schmidt, W. Schnick, F. Neese, *J. Am. Chem. Soc.* **2022**, *144*, 8038–8053.

[7] H. Kageyama, T. Yajima, Y. Tsujimoto, T. Yamamoto, C. Tassel, Y. Kobayashi, *Bull. Chem. Soc. Jpn.* **2019**, *92*, 1349–1357.

[8] A. Fuertes, *Inorg. Chem.* **2006**, *45*, 9640−9642.

[9] F. Takeiri, A. Watanabe, A. Kuwabara, H. Nawaz, N. I. P. Ayu, M. Yonemura, R. Kanno, G. Kobayashi, *Inorg. Chem.* **2019**, *58*, 4431−4436.

[10] K. Higashi, M. Ochi, Y. Nambu, T. Yamamoto, Taito Murakami, N. Yamashina, C. Tassel, Y. Matsumoto, H. Takatsu, C. M. Brown, H. Kageyama, *Inorg. Chem.* **2021**, *60*, 11957−11963.

[11] F. Altorfer, W. Bührer, B. Winkler, G. Coddens, R. Essmann, H. Jacobs, *Solid State Ion.* **1994**, *70*, 272−277.

[12] T. Wu, K. Fujii, T. Murakami, M. Yashima, S. Matsuishi, *Inorg. Chem.* **2020**, *59*, 15384–15393.

[13] A. Mutschke, T. Wylezich, C. Ritter, A. J. Karttunen, N. Kunkel, *Eur. J. Inorg. Chem.* **2019**, *48*, 5073–5076.

[14] M. Matsuo, A. Remhof, P. Martelli, R. Caputo, M. Ernst, Y. Miura, T. Sato, H. Oguchi, H. Maekawa, H. Takamura, A. Borgschulte, A. Züttel, S.-I. Orimo, *J. Am. Chem. Soc.* **2009**, *131*, 16389–16391.

[15] L. Gamperl, O. E. O. Zeman, P. Strobel, P. J. Schmidt, W. Schnick, *Chem. Eur. J.* **2022**, *28*, e202104007.

[16] M. Somer, Ö. Yaren, O. Reckeweg, Y. Prots, W. Carrillo-Cabrera, *Z. Anorg. Allg. Chem.* **2004**, *630*, 1068–1073.

[17] N. Kunkel, H. Kohlmann, *J. Phys. Chem. C* **2016**, *120*, 10506−10511.

[18] Y. Iwasaki, N. Matsui, K. Suzuki, Y. Hinuma, M. Yonemura, G. Kobayashi, M. Hirayama, I. Tanaka, R. Kanno, *J. Mater. Chem. A* **2018**, *6*, 23457–23463.

[19] C. E. Messer, *J. Solid State Chem.* **1970**, *2*, 144–155.

[20] H.-J. Meyer, *Dalton Trans.* **2010**, *39*, 5973–5982.

[21] M. Wörle, H. M. z. Altenschildesche, R. Nesper, *J. Alloys Compd.* **1998**, *264*, 107–114.

[22] V. F. Sears, *Neutron News* **1992**, *3*, 26–37.

[23] F. Rohrer, R. Nesper, *J. Solid State Chem.* **1998**, *135*, 194–200.

[24] R. Pöttgen, O. Reckeweg, *Z. Kristallogr.* **2017**, *232*, 653–668.

[25] B. Blaschkowski, T. Schleid, *Z. Anorg. Allg. Chem.* **2007**, *633*, 2644–2648.

[26] M. Häberlen, J. Glaser, H.-J. Meyer, *J. Solid State Chem.* **2005**, *178*, 1478–1487.

[27] Y. Ruiz-Morales, G. Schreckenbach, T. Ziegler, *Organometallics* **1996**, *15*, 3920−3923.

[28] A. Mutschke, G. M. Bernard, M. Bertmer, A. J. Karttunen, Clemens Ritter, V. K. Michaelis, N. Kunkel, *Angew. Chem. Int. Ed.* **2021**, *60*, 5683–5687.

[29] J. Schneider, C. P. Sindlinger, K. Eichele, H. Schubert, L. Wesemann, *J. Am. Chem. Soc.* **2017**, *139*, 6542−6545.

[30] A. H. Silver, P. J. Bray, *J. Chem. Phys.* **1958**, *29*, 984–990.

[31] T. Bräuniger, M. Jansen, *Z. Anorg. Allg. Chem.* **2013**, *639*, 857–879.

[32] T. Wylezich, R. Valois, M. Suta, A. Mutschke, C. Ritter, A. Meijerink, A. J. Karttunen, N. Kunkel, *Chem. Eur. J.* **2020**, *26*, 11742–11750.

[33] T. Wu, A. Ishikawa, T. Honda, H. Tamatsukuri, K. Ikeda, T. Otomo, S. Matsuishi, *RSC Adv.* **2020**, *9*, 5282–5287.

[34] O. Reckeweg, F. J. DiSalvo, *Solid State Sci.* **2002**, *4*, 575–584.

[35] A. F. Holleman, N. Wiberg, *Lehrbuch der Anorganischen Chemie*, Walter de Gruyter, Berlin, Germany, **2007**.

[36] G. M. Sheldrick, SADABS Version 2: Multi-Scan Absorption Correction, Bruker-AXS, Madison, Wisconsin, USA, **2012**.

[37] Bruker-AXS, XPREP Reciprocal Space Exploration, Vers. 6.12, Karlsruhe, Germany, **2001**.

[38] G. M. Sheldrick, SHELXS - A Program for Crystal Structure Solution, University of Göttingen, Göttingen, Germany, **1997**.
[39] G. M. Sheldrick, *Acta Crystallogr.* **2008**, *A64*, 112–122.
[40] K. Momma, F. Izumi, *J. Appl. Crystallogr.* **2011**, *44*, 1272–1276.
[41] H. M. Rietveld, *J. Appl. Crystallogr.* **1969**, *2*, 65–71.
[42] A. Coelho, TOPAS-Academic V6.1, Coelho Software, Brisbane, Australia, **2007**.
[43] M. Bowden, M. Ryan, *J. Appl. Crystallogr.* **2010**, *43*, 693−698.
[44] P. Thompson, D. E. Cox, J. B. Hastings, *J. Appl. Crystallogr.* **1987**, *20*, 79–83.
[45] R. Dovesi, A. Erba, R. Orlando, C. M. Zicovich-Wilson, B. Civalleri, L. Maschio, M. Rérat, S. Casassa, J. Baima, S. Salustro, B. Kirtman, *Wiley Interdiscip. Rev.-Comput. Mol. Sci.* **2018**, *8*, e1360.
[46] J. P. Perdew, K. Burke, M. Ernzerhof, *Phys. Rev. Lett.* **1996**, *77*, 3865–3868.
[47] C. Adamo, V. Barone, *J. Chem. Phys.* **1999**, *110*, 6158–6170.
[48] F. Weigend, R. Ahlrichs, *Phys. Chem. Chem. Phys.* **2005**, *7*, 3297–3305.
[49] A. J. Karttunen, T. Tynell, M. Karppinen, *J. Phys. Chem. C* **2015**, *119*, 13105–13114.
[50] B. Scheibe, C. Pietzonka, O. Mustonen, M. Karppinen, A. J. Karttunen, M. Atanasov, F. Neese, M. Conrad, F. Kraus, *Angew. Chem. Int. Ed.* **2018**, *57*, 2914–2918.
[51] H. J. Monkhorst, J. D. Pack, *Phys. Rev. B* **1976**, *13*, 5188–5192.
[52] Y. Hinuma, G. Pizzi, Y. Kumagai, F. Oba, I. Tanaka, *Comput. Mater. Sci.* **2017**, *128*, 140–184.
[53] A. Togo, I. Tanaka, **2018**, arXiv:1808.01590.
[54] F. Pascale, C. M. Zicovich-Wilson, F. L. Gejo, B. Civalleri, R. Orlando, R. Dovesi, *J. Comput. Chem.* **2004**, *25*, 888–897.
[55] C. M. Zicovich-Wilson, F. Pascale, C. Roetti, V. R. Saunders, R. Orlando, R. Dovesi, *J. Comput. Chem.* **2004**, *25*, 1873–1881.
[56] L. Maschio, B. Kirtman, M. Rérat, R. Orlando, R. Dovesi, *J. Chem. Phys.* **2013**, *139*, 164101.
[57] A. P. Scott, L. Radom, *J. Phys. Chem.* **1996**, *100*, 16502–16513.

3 A Novel Nitridoborate Hydride $Sr_{13}[BN_2]_6H_8$ Elucidated from X-ray and Neutron Diffraction Data

Published in: *Chem. Eur. J.* **2023**, e202301241

Authors: Sophia L. Wandelt, Alexander Mutschke, Dmitry Khalyavin, Jennifer Steinadler, and Wolfgang Schnick

DOI: https://doi.org/10.1002/chem.202301241

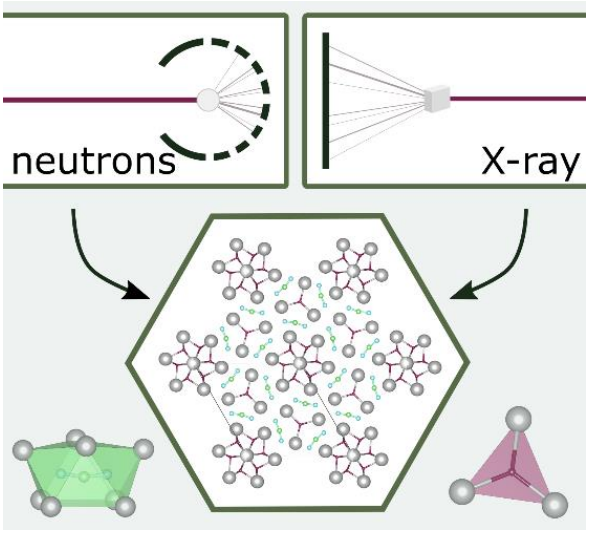

Abstract. Metal hydrides are an uprising compound class bringing up various functional materials. Due to the low X-ray scattering power of hydrogen, neutron diffraction is often crucial to fully disclose the structural characteristics thereof. We herein present the second strontium nitridoborate hydride known so far, $Sr_{13}[BN_2]_6H_8$, formed in a solid-state reaction of the binary nitrides and strontium hydride at 950 °C. The crystal structure was elucidated based on single-crystal X-ray and neutron powder diffraction in the hexagonal space group $P6_3/m$ (no. 176), exhibiting a novel three-dimensional network of $[BN_2]^{3-}$ units and hydride anions connected by strontium cations. Further analyses with magic angle spinning (MAS) NMR and vibrational spectroscopy corroborate the presence of anionic hydrogen within the structure. Quantum chemical calculations reveal the electronic properties and support the experimental outcome. $Sr_{13}[BN_2]_6H_8$ expands the emerging family of nitridoborate hydrides, broadening the access to an open field of new, intriguing materials.

3.1 Introduction

Convincing with a widespread variety of structural and functional features, the class of metal hydrides is an exciting field of current research. Intriguing properties such as hydrogen storage or luminescence upon doping with Eu^{2+} demonstrate the practical applicability of these materials.[1,2] Moreover, metal hydrides can exhibit fast hydride ion conductivity, enhancing their attractiveness as alternative energy materials for application in solid-state batteries.[3,4] Coming to the characterization of these compounds, the possibilities are limited. Laboratory X-ray diffraction (XRD) studies are often not capable of resolving light elements such as hydrogen or lithium due to their low electron density.[5] In contrast to X-rays, the scattering of neutrons is independent of the atomic number, but varies for each isotope and is influenced, among other factors, by the spin of the nucleus.[6] The coherent scattering length b_c together with the scattering cross section σ describes, how effective the neutrons will be scattered at the respective nucleus, analogous to the atomic form factor for X-ray radiation.[7] However, neutron diffraction allows distinction of neighboring elements such as nitrogen (b_c = 9.4 fm) and oxygen (b_c = 5.8 fm) and is also sensitive to different isotopes of an element. For instance, ^{10}B has a high σ, a negative b_c and shows strong neutron absorption, whereas ^{11}B has a moderate σ and b_c and is well suited for neutron experiments.[6] Analogously, the two stable isotopes of hydrogen show fundamentally different scattering lengths ($b_c(^1H)$ = −3.7 fm, $b_c(^2H)$ = 6.7 fm), so that a clear distinction of these nuclei is possible.[6] The peculiarities of certain elements can result in disruptive side effects such as absorption or incoherent scattering, making an isotope modification of the compound often necessary to obtain reliable diffraction data. Once the suitability of the sample is verified, neutron diffraction data can reveal various structural features, such as magnetic properties or superstructures caused by light elements.[8,9] In the case of hydride compounds, neutron data allow for the exact determination of the crystallographic positions, occupancies and atomic parameters of hydrogen or deuterium atoms in the crystal structure. Taking a closer look at their structural motifs, hydridic compounds comprise a large variability of coordination spheres and bonding partners of the hydride anion. Ranging from linear, for example in $LiNiH_3$, over trigonal planar and tetrahedral in $CaAlH_5$ up to octahedral coordination in Ba_2NH, the $M^{\delta+}$–$H^{\delta-}$ distances vary from 1.6 to 3.0 Å, respectively.[10–12] Within this structural diversity, hydrides tend to build compounds with multiple cations or multiple anions, whereas the latter have gained much interest in research over the last decades. Combining different anions in one material allows tailoring its physical, structural and electronic

features.[13] Multinary hydrides are largely dominated by hydride oxides and hydride fluorides due to their similar atomic radii, easy accessibility and high stability.[2,14,15] Other anion combinations such as hydrides and nitridoborates are a less explored class so far. Only two representatives of nitridoborate hydrides have been reported to date, namely Ca_2BN_2H and Sr_2BN_2H, leaving an open field of new functional and structurally diverse materials.[16,17]

Herein, we present the strontium nitridoborate hydride $Sr_{13}[BN_2]_6H_8$, which was synthesized from the respective nitrides and strontium hydride and crystallizes in a new structure type. Single-crystal X-ray and neutron powder diffraction data together with MAS NMR and vibrational spectroscopy provide a comprehensive structural analysis of the compound.

3.2 Results and Discussion

3.2.1 Synthesis

Analogous to other nitridoborate hydrides, $Sr_{13}[BN_2]_6H_8$ was synthesized in a solid-state reaction of stoichiometric amounts of Sr_2N, SrH_2 and BN in a sealed tantalum ampule under argon atmosphere at 950 °C. It is highly sensitive to air and moisture and exhibits colorless, block-like crystals up to 50 µm in length. The bulk sample was analyzed by means of powder XRD (Figure 3.1), showing a high phase purity of $Sr_{13}[BN_2]_6H_8$. The crystallographic data of the Rietveld refinement can be found in Table S3.1 in the Appendix.

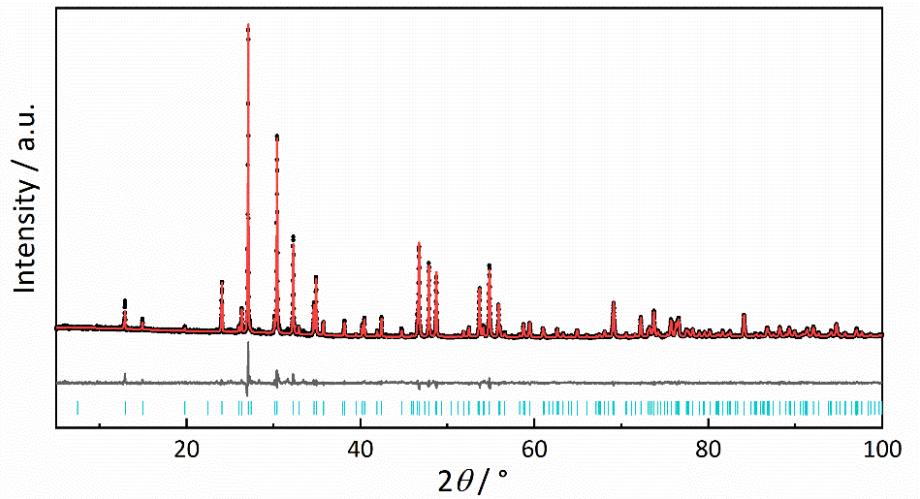

Figure 3.1. Rietveld refinement of $Sr_{13}[BN_2]_6H_8$ based on powder XRD data. The red, black and gray lines mark the calculated and experimental data and their difference, respectively, the Bragg markers are displayed in blue.

3.2.2 Structure Elucidation

The crystal structure of the title compound was partially elucidated from single-crystal XRD data (Table 3.1). Due to the low scattering power of hydrogen, only Sr, B, and N could be refined, building a three-dimensional network in the hexagonal space group $P6_3/m$ (no. 176). To determine the atomic positions of hydrogen in the structure, neutron powder diffraction was performed. As mentioned earlier, ^{1}H has a large incoherent scattering length and ^{10}B acts as a neutron absorber, necessitating a synthesis with ^{11}B and ^{2}H to obtain reliable data. Rietveld refinement of the neutron diffraction pattern (Figure 3.2, Table 3.1) led to two crystallographic positions of hydrogen on fully occupied Wyckoff positions 6*h* and 2*d*.

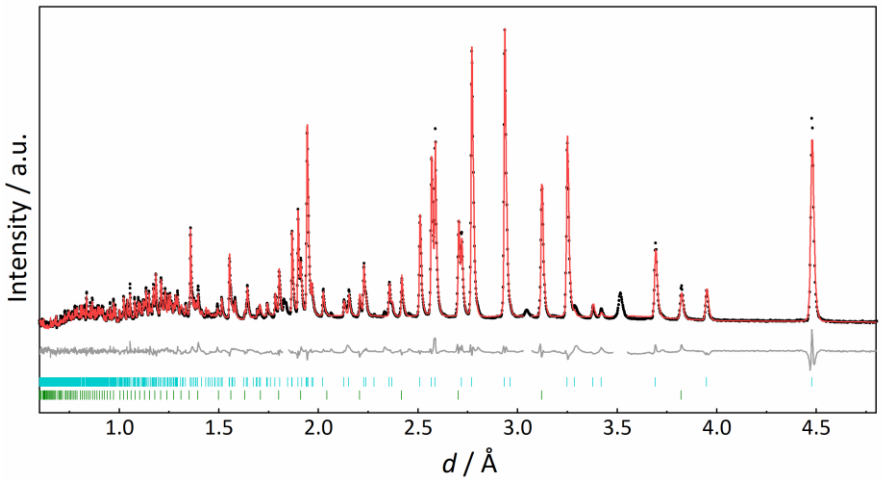

Figure 3.2. Rietveld refinement of $Sr_{13}[^{11}BN_2]_6D_{6.8}H_{1.2}$ based on time-of-flight neutron powder diffraction data collected at the high-resolution backscattering detector bank with the average $2\vartheta = 153°$. The black, red and gray lines mark the experimental and calculated data and their difference, respectively. The Bragg markers indicate $Sr_{13}[^{11}BN_2]_6D_{6.8}H_{1.2}$ (top, 94.7(3) wt-%) and $Sr_3B_2N_4$ (bottom, 5.4(1) wt-%).

Due to minor hydrogen impurities in the starting material ^{11}BN (elemental analysis results are listed in Table S3.2), the sample could not be completely deuterated, resulting in a sum formula of $Sr_{13}[^{11}BN_2]_6D_{6.8}H_{1.2}$. Both hydrogen positions show a similar mixed occupancy of about 84% D and 16% ^{1}H, which implies a formal scattering length of 5.0 fm at each position. As a deuterium deficiency with 75% vacancies would lead to the exact same scattering length, further analyses were necessary to support the mixed occupation with hydrogen. Infrared spectroscopy (Figure S3.1) shows that both ^{1}H and D vibrations are shifted by a factor of √2 due to the difference in atomic mass, indicating the presence of ^{1}H in the sample. Additionally, the ^{1}H MAS NMR data show the same two signals as the non-deuterated compound (Figure S3.2 and Figure 3.5). Taking

these analyses and charge balance into account, a deuterium deficiency cannot be fully excluded but seems unlikely. Similarly, the related compound Sr_2BN_2H already showed the same issue upon deuteration, resulting in a partially mixed occupation of ^1H and D.[16] The atomic positions, occupations and displacement parameters of XRD and neutron data refinements of $Sr_{13}[BN_2]_6H_8$ and $Sr_{13}[^{11}BN_2]_6D_{6.8}H_{1.2}$, respectively, are listed in Tables S3.3 and S3.4 in the Appendix.

Table 3.1. Crystallographic data of the single-crystal XRD refinement and Rietveld refinement based on neutron powder diffraction data of $Sr_{13}[BN_2]_6H_8$ and $Sr_{13}[^{11}BN_2]_6D_{6.8}H_{1.2}$, respectively. Standard deviations are given in parentheses.

formula	**$Sr_{13}[BN_2]_6H_8$**	**$Sr_{13}[^{11}BN_2]_6D_{6.8}H_{1.2}$**
formula mass / g·mol^{-1}	1380.10	1386.95
space group	$P6_3/m$ (no. 176)	
lattice parameters / Å	a = 13.6724(3) b = 3.8831(1)	a = 13.6797(1) b = 3.8853(4)
cell volume / Å^3	628.63(3)	629.67(1)
formula units / cell	1	
calculated density / g·cm^{-3}	3.646	3.657
diffractometer	Bruker D8 Venture	ISIS, WISH
radiation	Mo-Kα	neutrons (*tof*)
temperature / K	297	298
refined parameters	37	47
GoF	1.141	6.129
R indices	$R1$ ($I \geq 2\sigma(I)$) = 0.0177 $wR2$ ($I \geq 2\sigma(I)$) = 0.0336 $R1$ (all data) = 0.0233 $wR2$ (all data) = 0.0345	R_p = 0.0360 R_{wp} = 0.0398 R_{exp} = 0.0065 R_{Bragg} = 0.0474

3.2.3 Structure Description

$Sr_{13}[BN_2]_6H_8$ reveals a three-dimensional network of hydride and nitridoborate anions, connected by strontium cations (Figure 3.3a). Along the *c* axis, all atoms build one-dimensional stacks. The $[BN_2]^{3-}$ units are coordinated by eight strontium cations which build a channel-like network incorporating the hydride ions. Sr1 is coordinated as a slightly distorted $Sr(N_5H)$ octahedron, while Sr2 shows a 10-fold coordination by two full $[BN_2]^{3-}$ units, one N^{3-} of another $[BN_2]^{3-}$ unit and three H^- ions (Figure 3.3b). The Sr–N bond lengths are in the range of 2.541(3)–3.061(3) Å, agreeing with literature data.[18–20] In the middle of the Sr_7H_6 stars in the corners of the unit cell appears a strontium split position (Sr3) with 50% occupancy, trigonally planar coordinated by hydride ions. The slightly bent $[BN_2]^{3-}$ units are coordinated in a bicapped trigonal prism (Figure 3.3c), as already observed in β-$Ba_3[BN_2]_2$.[21] The N–B–N angle is 166.8(4)° and the B–N bond lengths range from 1.329(6) to 1.339(5) Å, in good agreement with other nitridoborates.[17,19] The hydride anions are trigonally planar and distorted tetrahedrally (Figure 3.3d) coordinated by strontium, showing bond lengths of 2.13(5)–2.60(5) Å, in accord with literature values.[16,22]

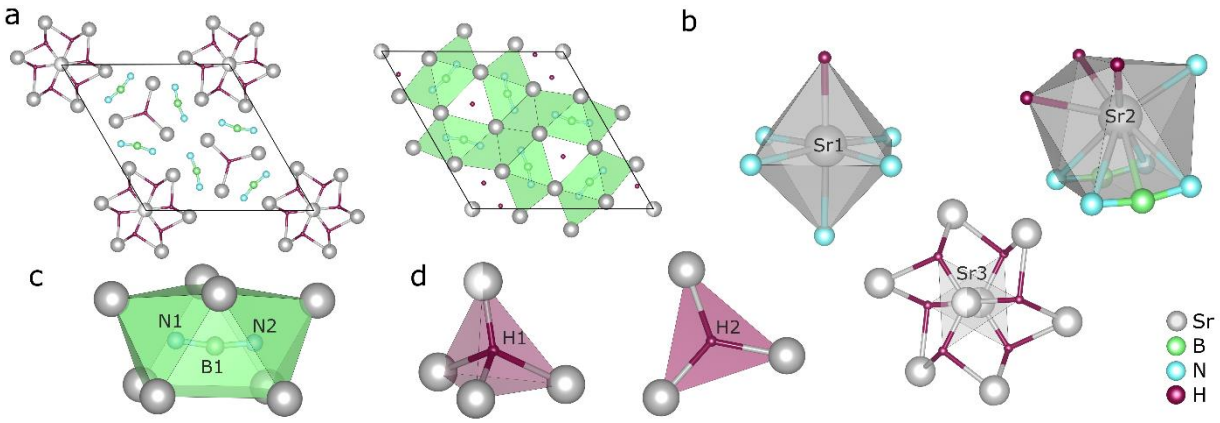

Figure 3.3. (a) Depiction of the crystal structure of $Sr_{13}[BN_2]_6H_8$ viewing along [001] (b) $Sr(N_5H)$ octahedron, $Sr(N_5B_2H_3)$ polyhedron and Sr_7H_6 star with the strontium split position in the center (c) $[BN_2]^{3-}$ unit coordinated by strontium as a bicapped trigonal prism (d) H^- anions distorted tetrahedrally and trigonally planar coordinated by strontium atoms. The Sr atoms are displayed in gray, B in green, N in blue and H in purple.

The formation of a previously unknown structure type, differentiates $Sr_{13}[BN_2]_6H_8$ from other nitridoborates such as the closely related nitridoborate hydrides Ca_2BN_2H and Sr_2BN_2H.[16,17] Most alkali and alkaline earth nitridoborates crystallize in the cubic structure types of $Sr_3[BN_2]_2$

and $LiCa_4[BN_2]_3$, showing a high symmetry and linear $[BN_2]^{3-}$ units.[23,24] In contrast, nitridoborate halides often exhibit slightly bent $[BN_2]^{3-}$ units and lower symmetry, building a more versatile group of akin structures.[19,25,26] As hydrides are closely related to halides – especially fluorides – the class of nitridoborate hydrides follows this trend. By combining known building blocks into a novel network type, $Sr_{13}[BN_2]_6H_8$ extends the family of structural intriguing nitridoborate compounds.

3.2.4 Vibrational Spectroscopy

IR and Raman spectroscopy are other suited methods to support the structure model due to the vibrational activity of both hydride and nitridoborate anions.[17,27,28] The experimental FTIR spectrum of $Sr_{13}[BN_2]_6H_8$ (Figure 3.4) agrees well with the simulated one obtained by DFT calculations at the PBE0 level of theory, showing the characteristic vibrations of the $[BN_2]^{3-}$ units and H^- atoms. The N–B–N vibrations are visible at 1668 cm^{-1} (antisymmetrical stretching, ν_2) and 600 cm^{-1} (in- and out-of- plane bending, ν_3), according to other known nitridoborates.[16,17] The hydride in-plane and out-of-plane vibrations arise at 1002, 889, 851 and 767 cm^{-1}, also in good agreement with literature.[16] Minor contaminations of $Sr_3B_2N_4$ cause the weak band at 1724 cm^{-1}. Furthermore, the presence of a NH^- or OH^- species can be ruled out, as there are no vibrational bands detectable in the region of 3600–3200 cm^{-1} (Figure S3.3).

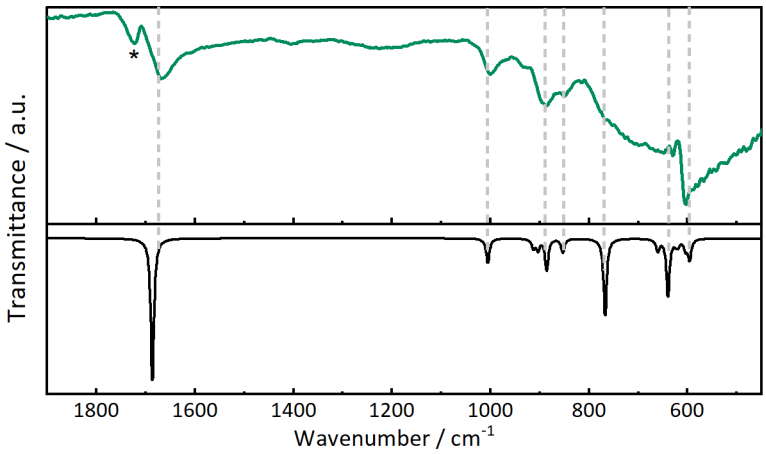

Figure 3.4. Experimental (top) and simulated (bottom) FTIR spectrum of $Sr_{13}[BN_2]_6H_8$. The band marked with an asterisk arises from the IR active side phase $Sr_3B_2N_4$.

The Raman spectrum of the title compound (Figure S3.4 in the Appendix) shows the symmetrical N–B–N stretching and H^- in-plane vibration at 1061 cm^{-1} as well as the N–B–N in-plane bending

and H^- in-plane vibration at 615 and 591 cm^{-1}. The expected hydride in-plane and out-of-plane vibrations in the region of 800–900 cm^{-1} remain rather broad and unresolved in contrast to the simulated spectrum. Below 300 cm^{-1}, the N–B–N in-plane and out-of-plane vibrations as well as the isotropic lattice vibrations are observable. The plane of the vibrations is described by the Sr atoms and the assignment of all vibrations is listed in Tables S3.5 and S3.6.

3.2.5 MAS NMR

^1H and ^{11}B MAS NMR measurements were performed to support the proposed structure model. The ^1H spectrum (Figure 3.5, left) shows two signals at 6.4 and 5.4 ppm, which is consistent with the presence of two crystallographically independent hydrogen positions in the structure. The signals are shifted towards the lower magnetic field, an effect already observed for other salt-like hydride species.[27,29,30] The MAS spectrum of ^{11}B (I = 3/2) shows the central-transition resonance, which exhibits second order broadening due to the quadrupolar interaction (Figure 3.5, right). The position of this resonance line is determined by the quadrupolar interaction and the chemical shift, so a fit of the spectrum is required to extract the numerical values of these NMR parameters. This was done using the DMFIT program, and the resulting values are listed in Table 3.2.[31] For comparison, we have fitted the previously published ^{11}B NMR spectrum of Sr_2BN_2H, which also contains slightly bent $[BN_2]^{3-}$ ions.[16] The ^{11}B MAS NMR spectrum of the related compound $SrBa_8[BN_2]_6$ published by Seidel et al. provides another comparison.[32] As expected for the nearly linear structural motif of N–B–N, the quadrupole coupling constant is rather large, with values beyond 3 MHz, rarely observed in periodic solids.[33] In contrast, the asymmetry parameter is close to zero, reflecting the axial symmetry of the $[BN_2]^{3-}$ ions, which are indeed perfectly linear in $SrBa_8[BN_2]_6$. The slight bend of the N–B–N units in the other compounds could tentatively correlate to an increase in the asymmetry parameter (Table 3.2). However, it should be noted that the quality of the ^{11}B spectra recorded for all listed compounds is not sufficient to determine the asymmetry parameter with high accuracy.

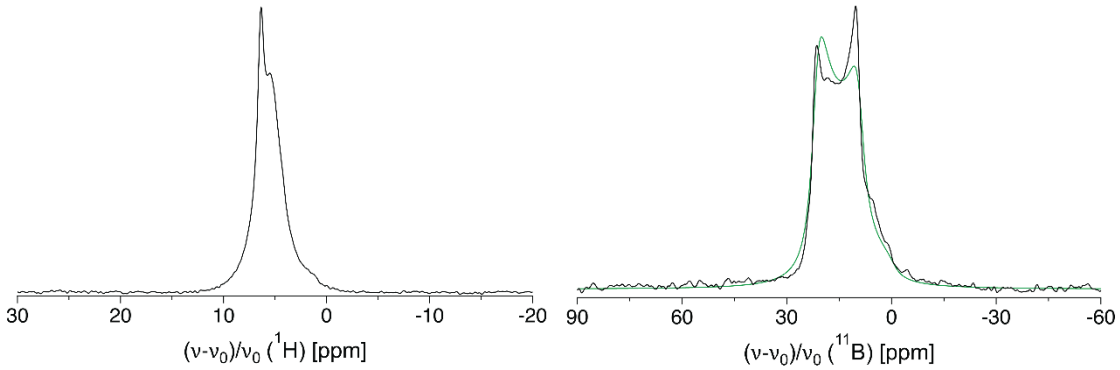

Figure 3.5. MAS NMR spectra of $Sr_{13}[BN_2]_6H_8$ at 20 kHz spinning frequency. ^{1}H (left) and ^{11}B spectrum (right), the latter shown with the best fitting result (green line).

Table 3.2. Calculated values of the chemical shift, quadrupole coupling constant and asymmetry parameter for $SrBa_8[BN_2]_6$, Sr_2BN_2H and $Sr_{13}[BN_2]_6H_8$. *NMR parameters reported here for the first time.

compound	δ_{iso} /ppm	C_Q /MHz	η_Q	∢(N–B–N) /°	Ref.
$SrBa_8[BN_2]_6$	26.6	3.30	0.02	180	[32]
Sr_2BN_2H	23.6	3.31	0.04	174.9	[16]*
$Sr_{13}[BN_2]_6H_8$	25.2	3.25	0.09	166.8	this work*

3.2.6 Electronic Properties

Quantum chemical calculations at DFT-PBE0 level of theory were performed to analyze the electronic and vibrational properties of $Sr_{13}[BN_2]_6H_8$. However, due to the disorder of the Sr3 position, an ordered model of the experimentally determined crystal structure was employed. By lowering the symmetry to the space group *P*3 (no. 143), the disorder was removed and an averaged Sr3 position (Sr5 in the new model) was established. The ordered model was optimized and appears to be a local minimum with no imaginary frequencies. Compared to the experimental data, the optimized lattice parameters *a* and *c* of the ordered model deviate by −0.05 % and −0.2 %, respectively. The calculated electronic band structure (Figure 3.6, left) indicates a direct bandgap of 5.2 eV. This is reflected by the colorless and transparent appearance of $Sr_{13}[BN_2]_6H_8$, classifying this compound as an insulator. Similar to Sr_2BN_2H, mostly nitrogen states contribute to the top of the valence band in the projected density of states (Figure 3.6, right) with only minor contributions from the other elements.[16] However, the

hydrogen bands emerge predominantly at lower energies, contrary to other known multinary hydride compounds.[34,35]

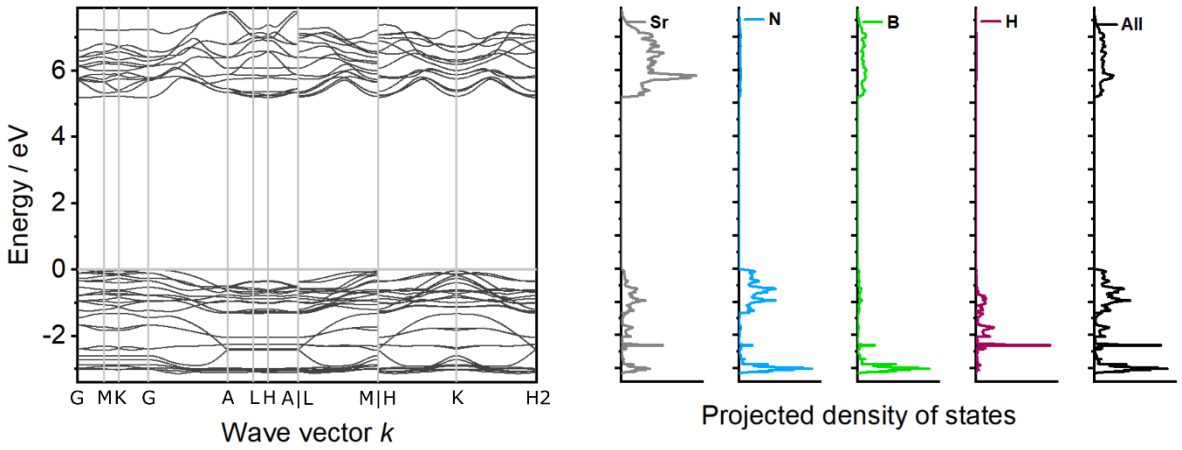

Figure 3.6. Electronic band structure and projected density of states of $Sr_{13}[BN_2]_6H_8$ calculated at the DFT-PBE0/TZVP level of theory.

3.3 Conclusion

In this contribution, we present the novel strontium nitridoborate hydride $Sr_{13}[BN_2]_6H_8$ accessed in a solid-state reaction of the respective binary nitrides and strontium hydride. The crystal structure was solved using a combination of single-crystal X-ray and neutron powder diffraction data, revealing a novel three-dimensional network of nitridoborate and hydride anions connected by strontium cations. The powerful and necessary method of neutron diffraction confirms the atomic positions of hydrogen and corroborates the crystal structure in the hexagonal space group $P6_3/m$ (no. 176). Together with other analyses such as MAS NMR and vibrational spectroscopy, we provide a complete structural and analytical proof of hydride anions in the compound. Quantum chemical DFT calculations support the experimental results and reveal the electronic structure of $Sr_{13}[BN_2]_6H_8$. Such hydrogen-rich compounds bear a promising potential to be utilized as hydride ion conducting materials, as it has been demonstrated for several other hydridic compounds.[36,37] Considering the substantial structural and functional diversity mentioned above, the family of multinary hydrides offers great potential for new intriguing applications.

3.4 Experimental Part

3.4.1 Synthesis

The preparation and analyses of all samples were performed in Argon-filled gloveboxes (Unilab, MBraun, Garching, H_2O < 1 ppm, O_2 < 1 ppm) due to the moisture and air sensitivity of the starting materials and products. Strontium subnitride was prepared in a radio frequency furnace (IG 10/600; Hüttinger Elektronik, Freiburg, Germany) from granulated strontium metal (Sigma-Aldrich, 99.99%) in nitrogen atmosphere at 1000 °C for 24 h, analogous to DiSalvo et al. but at an elevated temperature.[20] Strontium hydride and deuteride were synthesized from strontium metal (Sigma-Aldrich, 99.99%) in an autoclave reaction in hydrogen (Westfalen AG, 99.9%) or deuterium (Airliquide, 99.9%) atmosphere at 60 bar and 450 °C for 15 h.[35] Boron nitride and ^{11}boron nitride were obtained in an ammonia gas flow reaction of boric acid (Sigma-Aldrich, 99%) or ^{11}boric acid (Sigma-Aldrich, 99%) at 800 °C with 1 equiv. of urea (Sigma-Aldrich, > 99.5%) acting as a catalyst.[38] The title compound $Sr_{13}[BN_2]_6H_8$ and its analogous deuteride $Sr_{13}[^{11}BN_2]_6D_{6.8}H_{1.2}$ were synthesized in a solid-state reaction from Sr_2N, SrH_2 (SrD_2) and BN (^{11}BN) with a stoichiometry of 5:3:5. After grinding, the powder was transferred in a tantalum ampoule, which was then weld shut in an arc furnace (Handy-TIG 210 DC, LORCH, Auenwald-Mittelbrüden, Germany). The ampoule was subsequently placed in a silica tube and heated at 950 °C for 20 h in a tube furnace (Carbolite Gero, Neuhausen, Germany). The purity of all materials was analyzed by powder X-ray diffraction.

3.4.2 Single-Crystal XRD

A single crystal of $Sr_{13}[BN_2]_6H_8$ was isolated under argon atmosphere, transferred to a glass capillary and then sealed airtight. Diffraction data were collected on a Bruker D8 VENTURE diffractometer using a rotating anode and Mo-Kα radiation. The program package APEX3 was used for integration and absorption correction.[39–41] The structure solution and refinement was performed with SHELXS and SHELXL using direct methods and the least-squares method.[42,43] Deposition Number(s) 2239357 ($Sr_{13}[BN_2]_6H_8$) and 2239358 ($Sr_{13}[^{11}BN_2]_6D_{6.8}H_{1.2}$) contain(s) the supplementary crystallographic data for this paper. These data are provided free of charge by the joint Cambridge Crystallographic Data Centre and Fachinformationszentrum Karlsruhe Access Structures service.

3.4.3 Powder XRD

To analyze the bulk composition of each sample, the powder was ground and sealed in a glass capillary. The data were collected using a STOE Stadi P diffractometer with Cu-Kα_1 radiation, a Ge(111) monochromator, and a Mythen1K detector in modified Debye–Scherrer geometry. TOPAS6 was used for Rietveld refinements with a fundamental parameters approach and a shifted Chebychev function for the background.[44,45]

3.4.4 Neutron Powder Diffraction

The deuterated compound $Sr_{13}[^{11}BN_2]_6D_{6.8}H_{1.2}$ was loaded in a 6 mm vanadium can and then sealed with an indium wire. Time-of-flight neutron data were obtained using the WISH diffractometer at ISIS pulsed neutron source (STFC, Rutherford Appleton Laboratory, Harwell Campus, UK).[46] The program package FullProf was used for Rietveld refinement with a fundamental parameters approach and convolution of pseudo-Voigt with back-to-back exponential functions for profile fitting.[45,47] A coherent scattering length b_c = 6.65(4) fm was used for refining ^{11}B.[6]

3.4.5 FTIR Spectroscopy

Infrared spectra of the samples were collected on a Bruker Alpha II FTIR spectrometer using a diamond attenuated total reflectance (ATR) unit. All spectra were recorded in a glovebox in the range of 450–4000 cm^{-1} and with a resolution of 2 cm^{-1}.

3.4.6 Raman Spectroscopy

The Raman spectrum of a powder sample of $Sr_{13}[BN_2]_6H_8$ was measured with a Renishaw inVia Reflex Raman System in sealed glass capillaries in the range of 100–1200 cm^{-1} using a laser with a wavelength of λ = 532 nm and a charge-coupled device detector.

3.4.7 MAS NMR

Solid-state MAS NMR data were obtained using a 2.5 mm ZrO_2 rotor in a Bruker 500 AVANCE-III spectrometer operating at 500 MHz. The spectra were recorded at a spinning frequency of 20 kHz using a 2.5 µs 90° pulse, and were referenced indirectly to ^1H in 100 % TMS.

3.4.8 Quantum Chemical Calculations

The geometry, electronic and vibrational properties of the title compound were studied by density functional theory calculations conducted with the CRYSTAL17 program package at the DFT-PBE0 level of theory.[48–50] A full description of the computational analysis can be found in the Appendix.

3.5 Acknowledgements

The authors gratefully acknowledge the ISIS Neutron and Muon Source for granting beamtime (Proposal no. 2220086) and Christian Minke (Department of Chemistry, LMU Munich) for the MAS NMR measurements. Open Access funding enabled and organized by Projekt DEAL.

3.6 References

[1] B. Chao, L. Klebanoff, Hydrogen Storage in Interstitial Metal Hydrides, CRC Press, Florida **2012**.
[2] N. Kunkel, H. Kohlmann, *J. Phys. Chem. C* **2016**, *120*, 10506–10511.
[3] A. J. E. Rowberg, C. G. V. d Walle, *ACS Appl. Energ. Mater.* **2021**, *4*, 6348– 6355.
[4] Y. Yu, W. Zhang, H. Cao, T. He, P. Chen, *Trends Chem.* **2022**, *4*, 935–947.
[5] W. I. F. David, K. Shankland, L. B. McCusker, C. Baerlocher, Structure Determination from Powder Diffraction Data, University Press, Oxford **2002**.
[6] V. F. Sears, *Neutron News* **1992**, *3*, 26–37.
[7] L. Koester, Neutron Scattering Lengths and Fundamental Neutron Interactions, Springer Verlag, Berlin **1977**.
[8] K. Higashi, M. Ochi, Y. Nambu, T. Yamamoto, T. Murakami, N. Yamashina, C. Tassel, Y. Matsumoto, H. Takatsu, C. M. Brown, H. Kageyama, *Inorg. Chem.* **2021**, *60*, 11957–11963.
[9] A. V. Irodova, E. Suard, *J. Alloys Compd*. **1999**, *291*, 184–189.
[10] R. Sato, H. Saitoh, N. Endo, S. Takagi, M. Matsuo, K. Aoki, S.-I. Orimo, *Appl. Phys. Lett.* **2013**, *102*, 091901.
[11] C. Weidenthaler, T. J. Frankcombe, M. Felderhoff, *Inorg. Chem.* **2006**, *45*, 3849–3851.
[12] F. Altorfer, W. Bührer, B. Winkler, G. Coddens, R. Essmann, H. Jacobs, *Solid State Ionics* **1994**, *70*, 272–277.
[13] H. Kageyama, K. Hayashi, K. Maeda, J. P. Attfield, Z. Hiroi, J. M. Rondinelli, K. R. Poeppelmeier, *Nat. Commun.* **2018**, *9*, 772.
[14] C. E. Messer, *J. Solid State Chem.* **1970**, *2*, 144–155.
[15] Y. Iwasaki, N. Matsui, K. Suzuki, Y. Hinuma, M. Yonemura, G. Kobayashi, M. Hirayama, I. Tanaka, R. Kanno, *J. Mater. Chem. A* **2018**, *6*, 23457–23463.
[16] S. L. Wandelt, A. Karnas, A. Mutschke, N. Kunkel, C. Ritter, W. Schnick, *Inorg. Chem.* **2022**, *61*, 12685–12691.

[17] M. Somer, Ö. Yaren, O. Reckeweg, Y. Prots, W. Carrillo-Cabrera, *Z. Anorg. Allg. Chem.* **2004**, *630*, 1068–1073.
[18] S. G. Jantz, R. Erdmann, S. Hariyani, J. Brgoch, H. A. Höppe, *Chem. Mater.* **2020**, *32*, 8587–8594.
[19] F. Rohrer, R. Nesper, *J. Solid State Chem.* **1998**, *135*, 194–200.
[20] O. Reckeweg, F. J. DiSalvo, *Solid State Sci.* **2002**, *4*, 575–584.
[21] O. Reckeweg, F. J. DiSalvo, M. Somer, *J. Alloys Compd.* **2003**, *361*, 102–107.
[22] B. Blaschkowski, T. Schleid, *Z. Anorg. Allg. Chem.* **2007**, *633*, 2644–2648.
[23] H. Womelsdorf, H.-J. Meyer, *Z. Anorg. Allg. Chem.* **1994**, *620*, 262–265.
[24] M. Somer, U. Herterich, J. Curda, W. Carrillo-Cabrera, A. Zürn, K. Peters, H. G. von Schnering, *Z. Anorg. Allg. Chem.* **2000**, *626*, 625–633.
[25] M. Somer, M. N. Kütükcü, R. C. Gil, H. Borrmann, W. Carrillo-Cabrera, *Z. Anorg. Allg. Chem.* **2004**, *630*, 1015–1021.
[26] I. Kokal, U. Aydemir, Y. Prots, W. Schnelle, L. Akselrud, P. Höhn, M. Somer, *Z. Kristallogr.* **2011**, *226*, 633–639.
[27] A. Mutschke, G. M. Bernard, M. Bertmer, A. J. Karttunen, C. Ritter, V. K. Michaelis, N. Kunkel, *Angew. Chem. Int. Ed.* **2021**, *60*, 5683–5687.
[28] A. Mutschke, A. Schulz, M. Bertmer, C. Ritter, A. J. Karttunen, G. Kieslich, N. Kunkel, *Chem. Sci.* **2022**, *13*, 7773–7779.
[29] Y. Ruiz-Morales, G. Schreckenbach, T. Ziegler, *Organometallics* **1996**, *15*, 3920–3923.
[30] K. Hayashi, P. V. Sushko, Y. Hashimoto, A. L. Shluger, H. Hosono, *Nat. Commun.* **2014**, *5*, 3515.
[31] D. Massiot, F. Fayon, M. Capron, I. King, S. L. Calvé, B. Alonso, J. O. Durand, B. Bujoli, Z. Gan, G. Hoatson, *Magn. Reson. Chem.* **2002**, *40*, 70–76.
[32] S. Seidel, T. Dierkes, T. Jüstel, C. Benndorf, H. Eckert, R. Pöttgen, *Dalton Trans.* **2016**, *45*, 12078–12086.
[33] Y.-T. A. Wong, D. L. Bryce, *Annu. Rep. NMR Spectrosc.* **2018**, *93*, 213–279.
[34] T. Wu, A. Ishikawa, T. Honda, H. Tamatsukuri, K. Ikeda, T. Otomo, S. Matsuishi, *RSC Adv.* **2020**, *9*, 5282–5287.
[35] T. Wylezich, R. Valois, M. Suta, A. Mutschke, C. Ritter, A. Meijerink, A. J. Karttunen, N. Kunkel, *Chem. Eur. J.* **2020**, *26*, 11742–11750.
[36] Q. Bai, X. He, Y. Zhu, Y. Mo, *ACS Appl. Energ. Mater.* **2018**, *1*, 1626–1634.
[37] T. Hirose, T. Mishina, N. Matsui, K. Suzuki, T. Saito, T. Kamiyama, M. Hirayama, R. Kanno, *ACS Appl. Energ. Mater.* **2022**, *5*, 2968–2974.
[38] A. F. Holleman, N. Wiberg, Lehrbuch der Anorganischen Chemie, Walter de Gruyter, Berlin, Germany **2007**.
[39] Bruker-AXS, APEX3, Vers. 2016.5-0, Karlsruhe, Germany **2016**.
[40] Bruker-AXS, XPREP Reciprocal Space Exploration, Vers. 6.12, Karlsruhe, Germany **2001**.
[41] G. M. Sheldrick, SADABS Version 2: Multi-Scan Absorption Correction, Bruker-AXS, Madison, Wisconsin, USA **2012**.
[42] G. M. Sheldrick, SHELXS - A Program for Crystal Structure Solution, University of Göttingen, Göttingen, Germany **1997**.

[43] G. M. Sheldrick, *Acta Crystallogr.* **2008**, *A64*, 112–122.
[44] A. Coelho, TOPAS-Academic V6.1, Coelho Software, Brisbane, Australia **2007**.
[45] H. M. Rietveld, *J. Appl. Crystallogr.* **1969**, *2*, 65–71.
[46] L. C. Chapon, P. Manuel, P. G. Radaelli, C. Benson, L. Perrott, S. Ansell, N. J. Rhodes, D. Raspino, D. Duxbury, E. Spill, J. Norris, *Neutron News* **2011**, *22*, 22–25.
[47] J. Rodriguez-Carvajal, *Physica B+C* **1993**, *192*, 55–69.
[48] R. Dovesi, A. Erba, R. Orlando, C. M. Zicovich-Wilson, B. Civalleri, L. Maschio, M. Rérat, S. Casassa, J. Baima, S. Salustro, B. Kirtman, *Wiley Interdiscip. Rev.: Comput. Mol. Sci.* **2018**, *8*, e1360.
[49] J. P. Perdew, K. Burke, M. Ernzerhof, *Phys. Rev. Lett.* **1996**, *77*, 3865–3868.
[50] C. Adamo, V. Barone, *J. Chem. Phys.* **1999**, *110*, 6158–6170.

4 Combining Nitridoborates, Nitrides and Hydrides – Synthesis and Characterization of the Multianionic $Sr_6N[BN_2]_2H_3$

Published in: *Angew. Chem. Int. Ed.* **2023**, e202313564

Authors: Sophia L. Wandelt, Alexander Mutschke, Dmitry Khalyavin, Robert Calaminus, Jennifer Steinadler, Bettina V. Lotsch, and Wolfgang Schnick

DOI: https://doi.org/10.1002/anie.202313564

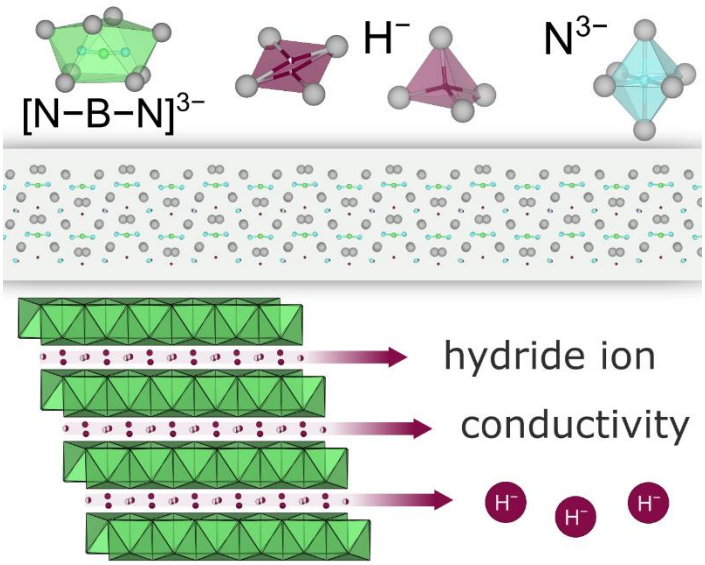

Abstract. Multianionic metal hydrides, which exhibit a wide variety of physical properties and complex structures, have recently attracted growing interest. Here we present $Sr_6N[BN_2]_2H_3$, prepared in a solid-state ampoule reaction at 800 °C, as the first combination of nitridoborate, nitride and hydride anions within a single compound. The crystal structure was solved from single-crystal X-ray and neutron powder diffraction data in space group $P2_1/c$ (no. 14), revealing a three-dimensional network of undulated layers of nitridoborate units, strontium atoms and hydride together with nitride anions. Magic angle spinning (MAS) NMR and vibrational spectroscopy in combination with quantum chemical calculations further confirm the structure model. Electrochemical measurements suggest the existence of hydride ion conductivity, allowing the hydrides to migrate along the layers.

4.1 Introduction

Metal hydrides gained significant interest in research over the last decades, acting as catalysts, luminescent materials or hydride ion conductors.[1–3] Next to their intriguing physical properties, metal hydrides are characterized by a large structural diversity that comprises manifold coordination environments and bonding partners of the hydrogen anion.[4] It can be surrounded by the respective metal cations in a linear, trigonal planar, tetrahedral, trigonal bipyramidal or even octahedral fashion.[5–8] In such materials, the respective metal hydride bond lengths vary from 1.6 to 3.0 Å. Introducing other metals or non-metals can even lead to complex anions such as $[BH_4]^-$ or $[NiH_4]^{4-}$.[9,10] Similarly, the nitride anion shows a wide variety of coordination environments. It is often found in complex $[NH_4]$, $[BN_x]$, $[PN_4]$ or $[SiN_4]$ moieties, but can also appear as an isolated N^{3-} ion. Binary metal nitrides hereby comprise diverse structural environments, ranging from coordination number two (linear) up to nine (capped quadratic antiprism).[11–18] The metal nitride distances differ significantly from 1.4 to 2.8 Å.

The incorporation of other anions into the respective compound provides a new platform of structures and functionalities. By combining different ionic radii, polarizabilities and electronegativities within one material, its properties can be tailored on demand.[19] While oxide hydrides and fluoride hydrides are the most prominent classes of multinary hydrides due to their high stability and easy accessibility, the field of nitride hydrides just established itself as functionally and structurally diverse. For instance, Ba_5CrN_4H and $Ca_6[Cr_2N_6]H$ show catalytic activity and magnetism, while Ca_2NH and Sr_2LiH_2N convince with hydrogen storage capacity and ion conductivity, respectively.[20–23] At the same time, they form diverse structures comprising complex $[Cr_2N_6]^{11-}$ anions or double chains of edge-sharing $N(Sr_5Li)$ and $H(Sr_5Li)$ octahedra. Nitridoborate hydrides containing complex $[N–B–N]^{3-}$ ions are another emerging group of structurally intriguing salt-like metal hydrides.[24] Starting with Ca_2BN_2H in 2004, this class combines highly stable nitridoborate ions next to the elusive hydride ions within one material.[25,26] When it comes to multinary compounds with three or more different anions, the hydride family is only sparsely explored yet, with $SmH_{0.78}OF_{0.22}$ and $Sr_2LiHOCl_2$ being just two recent members.[27,28] Due to the high reactivity and omnipresent abundance of oxygen, this class exclusively consists of hydride oxides. Neither an oxide-free nor a complex anion containing compound was found to date with such a multianionic composition.

In this contribution, we present the strontium nitridoborate nitride hydride $Sr_6N[BN_2]_2H_3$, which connects the two emerging fields of nitride hydrides and nitridoborate hydrides. Moreover, the oxide-free heteroanionic compound containing H^-, N^{3-} and $[BN_2]^{3-}$ anions possibly exhibits two-dimensional hydride ion conductivity.

4.2 Results and Discussion

4.2.1 Synthesis and Structure Elucidation

$Sr_6N[BN_2]_2H_3$ was obtained in a solid-state reaction of stoichiometric amounts of Sr_2N, SrH_2 and $Sr_3B_2N_4$ in a tantalum ampoule at 800 °C, yielding colorless block-like crystals. The crystal structure was partially solved based on single-crystal X-ray diffraction (XRD) data (Table 4.1), in which only the crystallographic positions of Sr, B and N could be determined reliably with X-ray data due to the low scattering power of hydrogen. Rietveld refinement based on powder XRD data of the bulk sample shows SrH_2 (5.5(2) wt %) and $Sr_3B_2N_4$ (2.1(1) wt %) as minor side phases (Figure S4.1 in the Appendix).

To reliably locate the hydrogen position in the structure, time-of-flight neutron powder diffraction data of the isotypic deuterated compound $Sr_6N[^{11}BN_2]_2D_3$ were collected. Additional isotope substitution with ^{11}B was necessary to avoid neutron absorption caused by ^{10}B. Rietveld refinement based on neutron powder diffraction data (Table 4.1, Figure S4.2) corroborate the proposed structure model with deuterium on two crystallographically independent sites coordinated by strontium atoms. While D1 is located on a fully occupied position inside a tetrahedron, D2 shows a split position with 50% occupancy within a distorted square planar coordination environment (Figure 4.1). Due to its comparatively large coordination sphere, the hydride anion shifts toward shorter Sr–H distances, resulting in two strongly distorted trigonal planar coordinated positions. The difference Fourier map calculated from the refined neutron diffraction data with unoccupied deuterium positions ($Sr_6N[^{11}BN_2]_2\square_3$) exhibits accordingly two distinct maxima of the core density at the D2 position (Figure 4.1). Crystallographic data of the X-ray and neutron refinements are listed in Tables S4.1 and S4.2.[29]

Table 4.1. Crystallographic data of the single-crystal XRD refinement and Rietveld refinement based on neutron powder diffraction data of $Sr_6N[BN_2]_2H_3$ and $Sr_6N[^{11}BN_2]_2D_3$, respectively.

formula	**$Sr_6N[BN_2]_2H_3$**	**$Sr_6N[^{11}BN_2]_2D_3$**
space group	$P2_1/c$ (no. 14)	
lattice parameters / Å, °	a = 6.6778(8) b = 11.387(1) c = 7.7311(9) β = 107.459(5)	a = 6.6821(2) b = 11.3884(4) c = 7.7416(2) β = 107.534(2)
cell volume / Å^3	560.8(1)	561.75(3)
formula units / unit cell	2	
molecular weight / g·mol^{-1}	620.41	623.81
temperature / K	293(2)	298(1)
diffractometer	Bruker D8 Venture	WISH @ ISIS
radiation	Mo-Kα (λ = 0.71973 Å)	neutrons, *time-of-flight*
refined parameters	69	70
GoF	1.077	8.240
R indices	$R1[I \geq 2\sigma(I)]$ = 0.0220 $wR2[I \geq 2\sigma(I)]$ = 0.0499 $R1$(all data) = 0.0262 $wR2$(all data) = 0.0509	R_p = 0.0411 R_{wp} = 0.0591 R_{exp} = 0.0072 R_{Bragg} = 0.0661

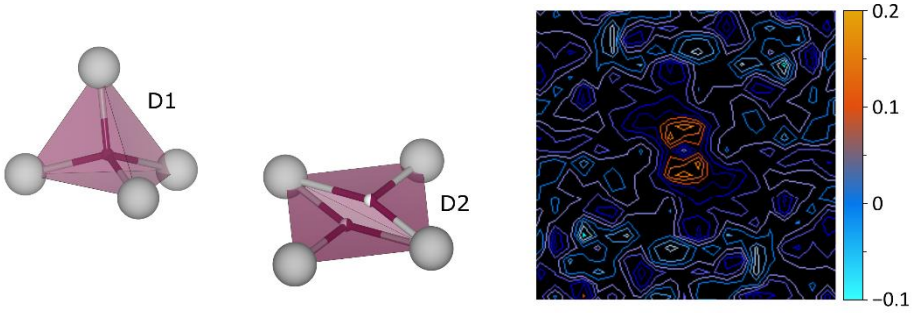

Figure 4.1. Illustration of the deuteride coordination spheres in $Sr_6N[^{11}BN_2]_2D_3$ (left), where the hydride atoms and polyhedra are displayed in purple and the Sr atoms in gray. Fourier map calculated from neutron diffraction data at the crystallographic position of D2 (right), the orange lines indicate residual core density.

4.2.2 Structure Description

$Sr_6N[BN_2]_2H_3$ exhibits a three-dimensional network consisting of alternating undulated layers of $[BN_2]^{3-}$ units, Sr atoms and hydride together with nitride anions (Figure 4.2a). Two of the Sr ions show a distorted octahedral coordination by two hydride and four nitrogen anions (Figure 4.2b), whereas the third Sr is found inside a $Sr(N_5B_2H_3)$ polyhedron, as previously seen in $Sr_{13}[BN_2]_6H_8$.[24] The coordination sphere of the $[BN_2]^{3-}$ units can be described as a bicapped trigonal prism (Figure 4.2c) which is also found in β-$Ba_3[BN_2]_2$.[30] The $[BN_2]^{3-}$ unit itself is slightly bent with an N–B–N angle of 169.4(5)° and shows N–B bond lengths of 1.329(7)–1.353(7) Å, which are in good agreement with other known nitridoborates.[31,32] The isolated N^{3-} ions are octahedrally coordinated by Sr atoms (Figure 4.2c) with expected Sr–N bond lengths of 2.549(4)–2.685(4) Å.[32,33] As mentioned above, the hydride ions are coordinated tetrahedrally and in a distorted trigonal planar fashion by Sr^{2+} (Figure 4.1). Both show Sr–H bond lengths of 2.47(1)–2.79(1) Å in accordance with literature data.[26,34,35]

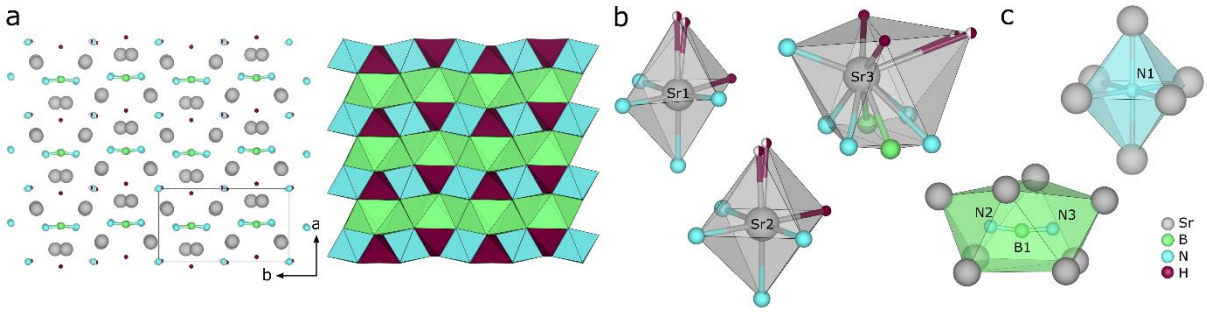

Figure 4.2. Illustration of the crystal structure of $Sr_6N[BN_2]_2H_3$. (a) Alternating undulated layers of Sr atoms, $[BN_2]^{3-}$ units and hydride and nitride anions (left) and respective polyhedra (right), both viewed along [001]. (b) $Sr(N_4H_2)$ octahedra and $Sr(N_5B_2H_3)$ polyhedron, (c) octahedrally coordinated N^{3-} anion and $[BN_2]^{3-}$ unit coordinated by strontium atoms in a bicapped trigonal prism. The Sr atoms and respective polyhedra are displayed in gray, N in blue, B in green and H in purple.

Firstly, $Sr_6N[BN_2]_2H_3$ seems to be structurally related to the compounds $(Sr_6N)[MN_2][CN_2]_2$ (*M* = Co, Fe, Cu) and $M_2[CN_2]Cl_2$ (*M* = Sr, Eu), which feature the same layer-like structure and isoelectronic $[N–C–N]^{2-}$ units.[36–39] But taking a closer look at the network reveals that the coordination polyhedra and orientation of the $[CN_2]^{2-}$ units along the layers vary significantly from those of our $[BN_2]^{3-}$ units. However, the compounds AE_3BX_2 (*AE* = Ca or Sr, *B* = $[C_3]^{4-}$ or $[CBN]^{4-}$ and *X* = Cl or Br) show more structural similarities to our title compound $Sr_6N[BN_2]_2H_3$.[40–42] The isoelectronic allenylide and carbonitridoborate units show a similar arrangement and

coordination polyhedra as our nitridoborate units. The *X*1 position is equally to the H1 position tetrahedrally coordinated by the respective alkaline earth metals, whereas *X*2 is inside a quadratic planar environment. However, as the strontium ions are shifted in $Sr_6N[BN_2]_2H_3$, the nitride and H2 ions are octahedrally and distorted trigonally planar coordinated, respectively.

4.2.3 MAS NMR

Our proposed structure model is further validated by ^{1}H and ^{11}B MAS NMR measurements. The ^{1}H spectrum (Figure 4.3, left) shows a main signal at 6.6 ppm originating from the two crystallographically independent H^- positions within the structure. Since the local environments of both positions are very similar, the chemical shift values are expected to be almost identical. In addition, homonuclear dicouplings between the hydrides lead to a broadening of the resonance lines, so that the two contributions are not resolved in the MAS spectrum. However, the shift of the ^{1}H resonance position towards positive δ_{iso} values is usually characteristic for protonic hydrogen and negative values are expected for hydrides. But as already observed in other metal hydrides and further discussed by Hosono et al., the metal–hydride distances have a significant influence on the chemical shift, resulting in the observed positive δ_{iso} for salt-like hydrides.[26,43–45] Minor impurities of Sr_2NH and an unknown side phase cause the two additional signals at 7.0 and 1.2 ppm, respectively.

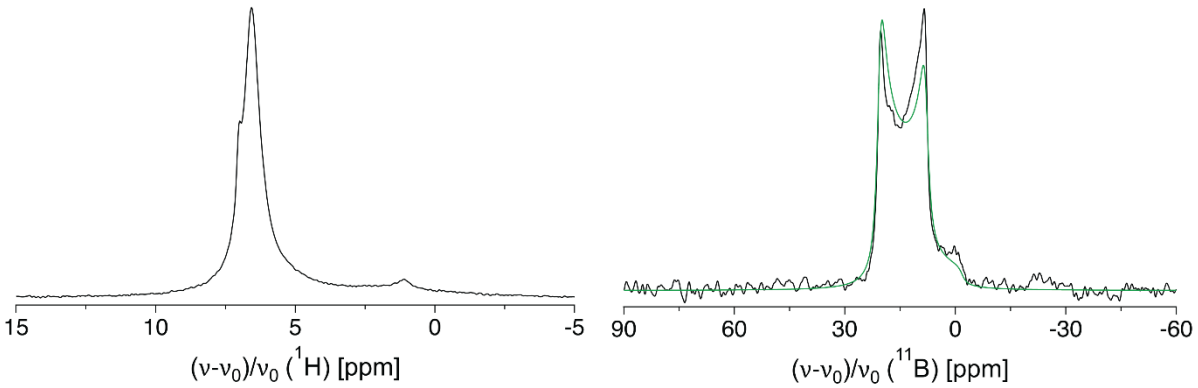

Figure 4.3. ^{1}H (left) and ^{11}B (right) MAS NMR spectrum of $Sr_6N[BN_2]_2H_3$ at 20 kHz spinning frequency. The best fitting result of the ^{11}B signal is shown as a green line.

The shape of the central transition signal in the ^{11}B MAS spectrum (Figure 4.3, right) is dominated by the interaction between the quadrupolar moment of ^{11}B (I = 3/2) and the electric field gradient (EFG) within the unit cell. Due to the asymmetric charge distribution around the B

atoms in the $[BN_2]^{3-}$ units, the observed line shape exhibits a characteristic broadening and is consistent with a single crystallographic site. Using the DMFIT program, values for the quadrupolar coupling constant (3.28 MHz) and the asymmetry parameter (0.05) were obtained as well as an isotropic chemical shift of 24.3 ppm.[46] Considering a N–B–N bond angle of 169.4°, these results fit nicely into the series of NMR parameters reported so far for nearly linear $[BN_2]^{3-}$ units in other nitridoborates.[24,47]

4.2.4 Vibrational Spectroscopy

As hydride and the complex nitridoborate anions can both be infrared and Raman active, vibrational spectroscopy is another suitable method to analyze our compound. The experimental FTIR spectrum of $Sr_6N[BN_2]_2H_3$ (Figure 4.4) agrees well with the simulated one, which was obtained by DFT calculations at the PBE0 level of theory. The strong bands of the N–B–N vibrations arise at 1652 cm^{-1} (antisymmetrical stretching, ν_2) and 599 cm^{-1} (out-of-plane bending, ν_3), which agrees well with the literature, as the ν_2 and ν_3 vibrations are usually expected at around 1700 and 600 cm^{-1}, respectively.[48] Hydride in-plane and out-of-plane vibrations, in which the hydride ion vibrates inside its strontium coordination sphere, can be observed at 919, 815 and 697 cm^{-1}, agreeing with literature.[24,25] The weak band at 1725 cm^{-1} is caused by N–B–N vibrations of the side phase $Sr_3B_2N_4$. Furthermore, any OH or NH species can be excluded, as there are no vibrations visible in the region of 3600–3200 cm^{-1} (Figure S4.3).

The Raman spectrum is also in good agreement with the simulated one (Figure S4.4). At 1057 cm^{-1} appears the strong N–B–N symmetrical stretching (ν_2), which is also in good accordance with related compounds.[49] Between 600 and 623 cm^{-1} the H^- out-of-plane vibrations and the N–B–N out-of-plane bending (ν_3) are detectable. Below 300 cm^{-1}, the bands of the isotropic lattice vibrations are visible. The plane of the different vibrations is described by the respective layers of nitridoborate and hydride ions. The assignment of IR and Raman vibrations can be found in Tables S4.3 and S4.4.

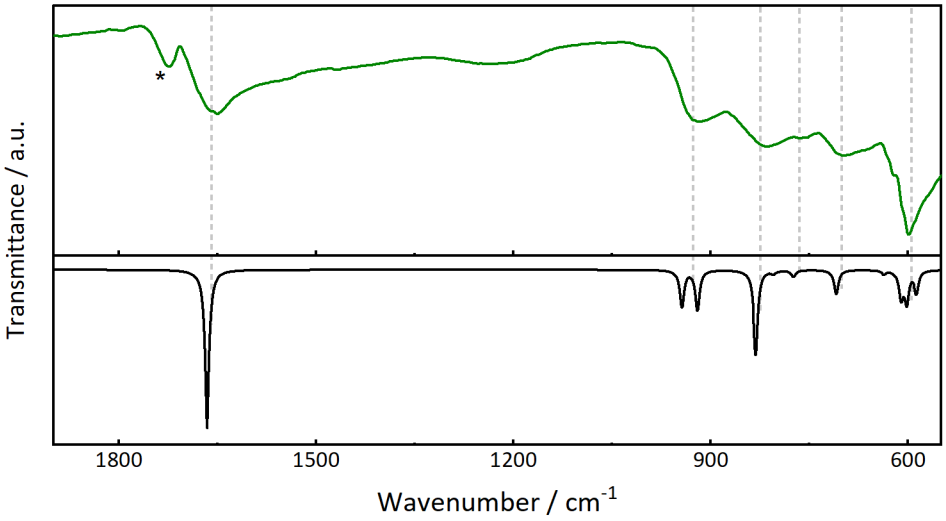

Figure 4.4. Experimental (top) and simulated (obtained by DFT-PBE0 calculations, bottom) FTIR spectrum of $Sr_6N[BN_2]_2H_3$. The band marked with an asterisk arises from the side phase $Sr_3B_2N_4$.

4.2.5 Hydride Ion Conductivity

As the layer-like structure provides a suitable prerequisite for two-dimensional migration of the hydride ions, we performed electrochemical impedance spectroscopy (EIS) and chronopotentiometry to evaluate possible ionic conductivity. The EIS measurement (Figure S4.5) shows an imperfect semicircle without a polarization tail, indicating a mixed ionic and electronic conductor. Taking both conduction processes into account, a fit of the spectrum revealed an electronic conductivity of 6.3×10^{-10} S/cm and an ionic conductivity of 3.3×10^{-9} S/cm at 75 °C.[50] To further confirm the conductivity values, we performed chronopotentiometry measurements (Figure S4.7), which yielded a similar value for the electronic conductivity and a smaller value for the ionic conductivity. The difference is discussed in the Appendix.

Taking a closer look on the thermal displacement ellipsoids from X-ray and neutron diffraction data, the ones of the hydride ions are rather large and elongated, whereas all other atoms are in a normal range. Therefore, we assume that hydride ions are the conducting species in our compound. Moreover, softBV calculations support this thesis, as they yield a low activation barrier for H^- and rather large values for Sr^{2+} (Figures S4.8 and S4.9).[51–53] Further details of the measurements and calculations can be found in the Appendix. Compared to other hydride ion conductors such as $Sr_2LiH_{2.2}O_{0.2}N_{0.8}$ (7.2×10^{-6} S/cm at 300 °C) or La_2LiHO_3 (3.85×10^{-6} S/cm at 275 °C), $Sr_6N[BN_2]_2H_3$ shows a lower conductivity, which may be attributed to the relatively low measurement temperature of 75 °C.[54-55] However, the ionic conductivity at 300 °C can be

estimated using the Arrhenius equation, yielding an ionic conductivity of 5.8×10^{-7} S/cm at 300 °C (Figure S4.10), which is in the range of other known hydride ion conductors.

4.2.6 Electronic Properties

The electronic structure of $Sr_6N[BN_2]_2H_3$ was investigated by quantum chemical calculations that were performed at the DFT-PBE0 level of theory. The crystal structure was optimized and determined to be a true local minimum without imaginary frequencies. The optimized lattice parameters *a*, *b*, *c*, and β deviate by −0.6%, −0.05%, −0.6% and 0.1%, respectively, from the experimental data. The calculated electronic band structure (Figure S4.11, left) reveals a direct bandgap of 4.1 eV, which agrees with the transparent and colorless appearance of $Sr_6N[BN_2]_2H_3$. Similarly to the two other nitridoborate hydrides Sr_2BN_2H and $Sr_{13}[BN_2]_6H_8$, the projected density of states (Figure S4.11, right) shows nitrogen at the top of the valence band with small contributions of Sr.[24,26] Interestingly, since both N and Sr states contribute to the top of the valence band, covalent interactions of N with Sr are indicated. This is also suggested by bond overlap population analysis (see Appendix) which indeed reveal considerable overlap between the isolated N^{3-} and Sr^{2+}.

4.3 Conclusion

Summing up, we have obtained the new strontium nitridoborate nitride hydride $Sr_6N[BN_2]_2H_3$ from a solid-state reaction at 800 °C. Combining single-crystal X-ray and neutron powder diffraction data, the crystal structure was elucidated. It reveals a novel three-dimensional network consisting of alternating undulated layers of strontium atoms, $[BN_2]^{3-}$ units and N^{3-} together with H^- ions. Further analyses such as MAS NMR, vibrational spectroscopy and quantum chemical calculations complement the structural analysis. Additionally, the new compound seems to exhibits ionic conductivity, enabling the hydride ions to migrate in a two-dimensional manner along the [011] plane.

4.4 Experimental Part

4.4.1 Synthesis

The bulk powder of $Sr_6N[BN_2]_2H_3$ and isotypic $Sr_6N[^{11}BN_2]_2D_3$ were synthesized by a solid-state reaction in a tantalum ampoule. Preparation and analyses of all samples were performed in an Ar-filled glovebox (Unilab, MBraun, Garching, $H_2O < 1$ ppm, $O_2 < 1$ ppm) due to the air and moisture sensitivity of the starting materials and products. $Sr_6N[BN_2]_2H_3$ and its analogue deuteride $Sr_6N[^{11}BN_2]_2D_3$ were synthesized from Sr_2N, $Sr_3B_2N_4$ ($Sr_3{}^{11}B_2N_4$) and SrH_2 (SrD_2) with a stoichiometry of 1:1:1.5. The starting materials were ground and filled into a tantalum ampoule, which was subsequently welded shut in an arc furnace (Handy-TIG 210 DC, LORCH, Auenwald-Mittelbrüden, Germany). The ampoule was further placed in a silica tube and then heated at 800 °C for 15 h in a tube furnace (Carbolite Gero, Neuhausen, Germany). Sr_2N was synthesized in a radio frequency furnace (IG 10/600; Hüttinger Elektronik, Freiburg, Germany), in which granulated Sr metal (Sigma-Aldrich, 99.99%) was heated in a tungsten crucible under nitrogen atmosphere at 1000 °C for 24 h. The reaction was carried out according to DiSalvo et al. but at an elevated temperature.[33] $Sr_3B_2N_4$ and $Sr_3{}^{11}B_2N_4$ were as well prepared in a radio frequency furnace, starting from Sr_2N and BN or ^{11}BN, respectively, in a ratio of 3:4 reacting at 1200 °C under nitrogen atmosphere for 20 h. BN and ^{11}BN were synthesized at 800 °C in an ammonia gas flow reaction of H_3BO_3 (Sigma-Aldrich, ≥ 99%) or $H_3{}^{11}BO_3$ (Sigma-Aldrich, ≥ 99%) with 1 equiv. of $CO(NH_2)_2$ (Sigma-Aldrich, > 99.5%) acting as a catalyst.[56] SrH_2 and SrD_2 were obtained from the reaction of Sr metal (Sigma-Aldrich, 99.99%) with H_2 (Westfalen AG, 99.9%) or D_2 (Airliquide, 99.8%) at 450 °C and 60 bar for 15 h in a self-made autoclave consisting of hardened Alloy 718.[57] The purity of all starting materials was analyzed by means of powder X-ray diffraction.

4.4.2 Single-Crystal XRD

For the structure determination of $Sr_6N[BN_2]_2H_3$, a single crystal was isolated and transferred into an airtight glass capillary. XRD data were collected on a Bruker D8 VENTURE TXS diffractometer with a rotating anode using Mo-Kα radiation and a combination of ϕ- and ω-scans. The data were integrated and absorption corrected (multiscan-method) using the program package APEX3.[58–60] SHELXS and SHELXL were used for structure solution (direct methods) and structure refinement using the least-squares method.[61,62]

4.4.3 Powder XRD

To prove the bulk composition of the starting materials and the product, the respective powder was ground and then sealed in a glass capillary. Diffraction data were collected on a STOE Stadi P diffractometer using Cu-Kα_1 radiation, a Ge(111) monochromator, and a Mythen1K detector in modified Debye-Scherrer geometry. Rietveld refinements were performed with the TOPAS6 package using a fundamental parameters approach and a shifted Chebyshev polynomial for modeling the background.[63,64]

4.4.4 Neutron Powder Diffraction

For neutron diffraction, the bulk powder of the deuterated compound $Sr_6N[^{11}BN_2]_2D_3$ was transferred into a 6 mm vanadium can and then sealed airtight with indium wire. Time-of-flight neutron data were collected on the WISH diffractometer at ISIS pulsed neutron source (STFC, Rutherford Appleton Laboratory, Harwell Campus, UK).[65] The Rietveld refinement of the collected pattern was performed with the program package FullProf, using a fundamental parameters approach and a convolution of pseudo-Voigt with back-to-back exponential functions for profile fitting.[64,66] A coherent scattering length b_c = 6.65(4) fm was used for refining ^{11}B.[67]

4.4.5 MAS NMR

Solid-state MAS NMR data of ^{1}H and ^{11}B were collected on a Bruker 500 AVANCE-III spectrometer operating at 500.2 MHz using a 2.5 mm ZrO_2 rotor. The spectra were acquired at a spinning frequency of 20 kHz with TMS (δ = 0 ppm) as a reference for the chemical shift.

4.4.6 FTIR Spectroscopy

Infrared spectra were obtained using a Bruker Alpha II FTIR spectrometer with a diamond attenuated total reflectance (ATR) unit. The spectra were recorded in an Ar-filled glovebox with a resolution of 2 cm^{-1} in the range of 450–4000 cm^{-1}.

4.4.7 Raman Spectroscopy

The Raman spectrum was acquired of a polycrystalline sample sealed in a glass capillary by a Renishaw inVia Reflex Raman System. Spectra were obtained in the range of 100–1200 cm^{-1} using a laser with a wavelength of λ = 532 nm and a charge-coupled device detector.

4.4.8 Conductivity Measurements

The sample was ground thoroughly prior to measurement and compacted by uniaxial cold pressing (1000 MPa/2 t) into a pellet of 0.346 mm thickness and 5 mm diameter. The pellet was contacted with indium foil to enhance electrode/sample-contact. No reactions were observed between the metal and the sample. All electrochemical measurements were performed using an Ivium compactstat.h and a TSC SW closed impedance cell (rhd instruments) under argon. Electrochemical impedance spectroscopy (EIS) was performed in a two-electrode setup, while the chronopotentiometry (CP) was performed in a pseudo-four-electrode setup. All measurements were conducted at a pressure of 720 kPa. For the impedance measurement, an AC voltage of 100 mV was applied. Impedance measurements were carried out in a temperature range between 25 °C and 75 °C and in a frequency range between 1 MHz and 0.01 Hz but due to noise the data was capped at 1 Hz for fitting. Activation energies were determined using the modified Arrhenius equation.[68] The impedance spectra were analyzed using the RelaxIS3 software from rhd instruments. For the calculation of the activation energies of the respective migrating ion, the program softBV was used.[51–53]

4.4.9 Quantum Chemical Calculations

To study the geometry, electronic and vibrational properties of $Sr_6N[BN_2]_2H_3$, density functional theory calculations at the DFT-PBE0 level of theory were conducted by the CRYSTAL17 program package.[69–71] In general, triple zeta polarized Gaussian type basis sets were used. Solely for Sr split valence polarized basis sets were used, as this is expected to be sufficient for only two valence electrons. All respective basis sets have been derived from the molecular Karlsruhe def2 basis sets and prior works.[57,72,73] The disordered H2 position (4*e*) was resolved by replacing the respective atoms fully occupied at the 2*b* position, representing an averaged position. The reciprocal space of the ordered model was sampled using 5x5x3 Monkhorst-Pack-type k-meshes.[74] The coulomb and exchange integrals were evaluated by tightened tolerance

(TOLINTEG) factors of 8, 8, 8, 8 and 16. For the evaluation of the electronically optimized structure, the atomic positions and lattice parameters were fully optimized within the constraints of the space group symmetry. The optimized lattice parameters *a*, *b*, *c*, and *β* were found to deviate by −0.6%, −0.05%, −0.6% and 0.1% from the experimental model respectively. Bond population overlap was determined by Mullikan population analysis. The band paths of the reciprocal space for the determination the electronic band structure were obtained by the Seek-path webservice.[75,76] Lastly, the harmonic frequencies and the respective Raman and IR intensities were simulated using the computational schemes implemented in the CRYSTAL17 program package.[77–79] As the input model was found to not exhibit imaginary frequencies, this ordered model appears as a true local energetic minimum. Raman intensities were calculated for polycrystalline powder samples with a Raman laser wavelength of $\lambda = 532$ nm and an experimental temperature of T = 298.15 K. The final IR and Raman spectra were simulated using a Lorentzian profile for the IR spectrum, a pseudo-Voigt profile (50:50 – Lorentzian:Gaussian) for the Raman spectrum and a FWHM of 8 cm^{-1} for both simulations. Additionally, a second ordered model was tested in comparison. This ordered model was derived by creating a 2x1x1 supercell and removing half of the hydrogen positions of the former 4*e* position, resolving the disorder. The computational processes were as described above. The lattice parameters 2*a*, *b*, *c*, and *β* differed by −1.3%, 0%, −0.6% and -1.12% respectively from the experimental input model. This structure was also found to be a true local minimum with no imaginary frequencies, validating both input structures as possible models for theoretical calculations. The electronic band structure and the simulated IR and Raman spectra shown in the manuscript and Appendix were derived from the smaller ordered model. The CIFs of both optimized structures can be found appended at the end of the Appendix.

4.5 Acknowledgements

The authors gratefully acknowledge the ISIS Neutron and Muon Source for granting beamtime (proposal no. 2220086) and financial support by the DFG under Germany's Excellence Strategy - EXC 2089/1-390776260 (e-conversion). Robert Calaminus gratefully acknowledges the German Federal Ministry of Education and Research (BMBF) for their financial support through the FestBatt project 03XP0430B. The authors thank Christian Minke (Department of Chemistry, LMU Munich) for the MAS NMR measurements.

4.6 References

[1] M. Kitano, J. Kujirai, K. Ogasawara, S. Matsuishi, T. Tada, H. Abe, Y. Niwa, H. Hosono, *J. Am. Chem. Soc.* **2019**, *141*, 20344–20353.

[2] N. Kunkel, H. Kohlmann, *J. Phys. Chem. C* **2016**, *120*, 10506−10511.

[3] Y. Yu, W. Zhang, H. Cao, T. He, P. Chen, *Trends Chem.* **2022**, *4*, 935–947.

[4] C. Janiak, H.-J. Meyer, D. Gudat, R. Alsfasser, E. Riedel, *Moderne Anorganische Chemie*, De Gruyter, Berlin, **2012**.

[5] R. Sato, H. Saitoh, N. Endo, S. Takagi, M. Matsuo, K. Aoki, S.-I. Orimo, *Appl. Phys. Lett.* **2013**, *102*, 091901.

[6] C. Weidenthaler, T. J. Frankcombe, M. Felderhoff, *Inorg. Chem.* **2006**, *45*, 3849−3851.

[7] T. V. Blankenship, M. J. Dickman, L. J. v. d. Burgt, S. E. Latturner, *Inorg. Chem.* **2015**, *54*, 914−921.

[8] F. Altorfer, W. Bührer, B. Winkler, G. Coddens, R. Essmann, H. Jacobs, *Solid State Ion.* **1994**, *70*, 272−277.

[9] G. Renaudin, L. Guénée, K. Yvon, *J. Alloys Compd.* **2003**, *350*, 145–150.

[10] M. Matsuo, A. Remhof, P. Martelli, R. Caputo, M. Ernst, Y. Miura, T. Sato, H. Oguchi, H. Maekawa, H. Takamura, A. Borgschulte, A. Züttel, S.-I. Orimo, *J. Am. Chem. Soc.* **2009**, *131*, 16389–16391.

[11] X. Zhao, K. J. Range, *J. Alloys Compd.* **2000**, *296*, 72–74.

[12] A. Brager, *Acta Physicochim. URSS* **1937**, *7*, 699–706.

[13] G. A. Jeffrey, G. S. Parry, R. L. Mozzi, *J. Chem. Phys.* **1956**, *25*, 1024–1031.

[14] P. Eckerlin, A. Rabenau, *Z. Anorg. Allg. Chem.* **1960**, *304*, 218–229.

[15] D. Fischer, Z. Cancarevic, J. C. Schön, M. Jansen, *Z. Anorg. Allg. Chem.* **2004**, *630*, 156–160.

[16] J. Hao, Q. L. Cui, G. Zou, J. Liu, X. Li, Y. Li, Q. L. Zhou, D. Iiu, M. Li, F. Li, W. W. Lei, W. Chen, Y. Ma, *Inorg. Chem.* **2009**, *48*, 9737–9741.

[17] E. Zintl, G. Brauer, *Z. Elektrochem. Angew. Phys. Chem.* **1935**, *41*, 102–107.

[18] G. V. M. Vajenine, X. Wang, I. Efthimiopoulos, S. Karmakar, K. Syassen, M. Hanfland, *Phys. Rev. B* **2009**, *79*, 224107.

[19] H. Kageyama, K. Hayashi, K. Maeda, J. P. Attfield, Z. Hiroi, J. M. Rondinelli, K. R. Poeppelmeier, *Nat. Commun.* **2018**, *9*, 772.

[20] Y. Guan, W. Zhang, Q. Wang, C. Weidenthaler, A. Wu, W. Gao, Q. Pei, H. Yan, J. Cui, H. Wu, S. Feng, R. Wang, H. Cao, X. Ju, L. Liu, T. He, J. Guo, P. Chen, *Chem Catal.* **2021**, *1*, 1042–1054.

[21] M. S. Bailey, M. N. Obrovac, E. Baillet, T. K. Reynolds, D. B. Zax, F. J. DiSalvo, *Inorg. Chem.* **2003**, *42*, 5572–5578.

[22] P. Chen, Z. Xiong, J. Luo, J. Lin, K. L. Tan, *Nature* **2002**, *420*, 302–304.

[23] G. Jiang, N. Matsui, T. Mezaki, Y. Toda, K. Suzuki, M. Hirayama, T. Saito, T. Kamiyama, R. Kanno, *J. Solid State Chem.* **2022**, *310*, 123051.

[24] S. L. Wandelt, A. Mutschke, D. Khalyavin, J. Steinadler, W. Schnick, *Chem. Eur. J.* **2023**, e202301241.

[25] M. Somer, Ö. Yaren, O. Reckeweg, Y. Prots, W. Carrillo-Cabrera, *Z. Anorg. Allg. Chem.* **2004**, *630*, 1068–1073.

[26] S. L. Wandelt, A. Karnas, A. Mutschke, N. Kunkel, C. Ritter, W. Schnick, *Inorg. Chem.* **2022**, *61*, 12685–12691.

[27] N. Zapp, H. E. Fischer, H. Kohlmann, *Inorg. Chem.* **2021**, *60*, 17775–17782.

[28] Z. Wei, H. Ubukata, C. Zhong, C. Tassel, H. Kageyama, *Inorg. Chem.* **2023**, *62*, 799–800.

[29] Depositions numbers 2279203 ($Sr_6N[BN_2]_2H_3$) and 2279204 ($Sr_6N[^{11}BN_2]_2D_3$) contain the supplementary crystallographic data for this paper. These data are provided free of charge by the joint Cambridge Crystallographic Data Centre and Fachinformationszentrum Karlsruhe Access Structures Service.

[30] O. Reckeweg, F. J. DiSalvo, M. Somer, *J. Alloys Compd.* **2003**, *361*, 102–107.

[31] M. Häberlen, J. Glaser, H.-J. Meyer, *J. Solid State Chem.* **2005**, *178*, 1478–1487.

[32] S. F. Matar, A. F. A. Alam, R. Pöttgen, *Z. Naturforsch. B* **2017**, *72*, 433–439.

[33] O. Reckeweg, F. J. DiSalvo, *Solid State Sci.* **2002**, *4*, 575–584.

[34] B. Blaschkowski, T. Schleid, *Z. Anorg. Allg. Chem.* **2007**, *633*, 2644–2648.

[35] F. Rohrer, R. Nesper, *J. Solid State Chem.* **1998**, *135*, 194–200.

[36] J. K. Bendyna, P. Höhn, W. Schnelle, R. Kniep, *Sci. Technol. Adv. Mater.* **2007**, *8*, 393–398.

[37] J. K. Bendyna, P. Höhn, R. Kniep, *Z. Kristallogr.* **2009**, *224*, 5–6.

[38] W. P. Clark, R. Niewa, *Z. Anorg. Allg. Chem.* **2020**, *646*, 114–119.

[39] W. Liao, R. Dronskowski, *Z. Anorg. Allg. Chem.* **2005**, *631*, 496–498.

[40] H. Womelsdorf, H.-J. Meyer, *Z. Anorg. Allg. Chem.* **1994**, *620*, 258–261.

[41] H.-J. Meyer, *Z. Anorg. Allg. Chem.* **1991**, *593*, 185–192.

[42] H.-J. Meyer, *Z. Anorg. Allg. Chem.* **1991**, *594*, 113–118.

[43] A. Mutschke, G. M. Bernard, M. Bertmer, A. J. Karttunen, C. Ritter, V. K. Michaelis, N. Kunkel, *Angew. Chem. Int. Ed.* **2021**, *60*, 5683–5687.

[44] K. Hayashi, P. V. Sushko, Y. Hashimoto, A. L. Shluger, H. Hosono, *Nat. Commun.* **2014**, *5*, 3515.

[45] A. Mutschke, A. Schulz, M. Bertmer, C. Ritter, A. J. Karttunen, G. Kieslich, N. Kunkel, *Chem. Sci.* **2022**, *13*, 7773–7779.

[46] D. Massiot, F. Fayon, M. Capron, I. King, S. L. Calvé, B. Alonso, J. O. Durand, B. Bujoli, Z. Gan, G. Hoatson, *Magn. Reson. Chem.* **2002**, *40*, 70–76.

[47] S. Seidel, T. Dierkes, T. Jüstel, C. Benndorf, H. Eckert, R. Pöttgen, *Dalton Trans.* **2016**, *45*, 12078–12086.

[48] R. Pöttgen, O. Reckeweg, *Z. Kristallogr.* **2017**, *232*, 653–668.

[49] I. Kokal, U. Aydemir, Y. Prots, W. Schnelle, L. Akselrud, P. Höhn, M. Somer, *Z. Kristallogr.* **2011**, *226*, 633–639.

[50] R. A. Huggins, *Ionics* **2002**, *8*, 300–313.

[51] H. Chen, L. L. Wong, S. Adams, *Acta Crystallogr.* **2019**, *B75*, 18–33.

[52] H. Chen, S. Adams, *IUCrJ* **2017**, *4*, 614–625.

[53] L. L. Wong, K. C. Phuah, R. Dai, H. Chen, W. S. Chew, S. Adams, *Chem. Mater.* **2021**, *33*, 625–641.

[54] A. J. E. Rowberg, L. Weston, C. G. V. d. Walle, *J. Phys. Chem. C* **2021**, *125*, 2250–2256.

[55] Y. Iwasaki, N. Matsui, K. Suzuki, Y. Hinuma, M. Yonemura, G. Kobayashi, M. Hirayama, I. Tanaka, R. Kanno, *J. Mater. Chem. A* **2018**, *6*, 23457–23463.

[56] A. F. Holleman, N. Wiberg, *Lehrbuch der Anorganischen Chemie*, De Gruyter, Berlin, Germany, **2007**.

[57] T. Wylezich, R. Valois, M. Suta, A. Mutschke, C. Ritter, A. Meijerink, A. J. Karttunen, N. Kunkel, *Chem. Eur. J.* **2020**, *26*, 11742–11750.

[58] G. M. Sheldrick, SADABS Version 2: Multi-Scan Absorption Correction, Bruker-AXS, Madison, Wisconsin, USA, **2012**.

[59] Bruker-AXS, XPREP Reciprocal Space Exploration, Vers. 6.12, Karlsruhe, Germany, **2001**.

[60] Bruker-AXS, APEX3, Vers. 2016.5-0, Karlsruhe, Germany, **2016**.

[61] G. M. Sheldrick, *Acta Crystallogr.* **2008**, *A64*, 112–122.

[62] G. M. Sheldrick, SHELXS – A Program for Crystal Structure Solution, University of Göttingen, Göttingen, Germany, **1997**.

[63] A. Coelho, TOPAS-Academic V6.1, Coelho Software, Brisbane, Australia, **2007**.

[64] H. M. Rietveld, *J. Appl. Crystallogr.* **1969**, *2*, 65–71.

[65] L. C. Chapon, P. Manuel, P. G. Radaelli, C. Benson, L. Perrott, S. Ansell, N. J. Rhodes, D. Raspino, D. Duxbury, E. Spill, J. Norris, *Neutron News* **2011**, *22*, 22–25.

[66] J. Rodriguez-Carvajal, *Physica B* **1993**, *192*, 55–69.

[67] V. F. Sears, *Neutron News* **1992**, *3*, 26–37.

[68] A. D. McNaught, A. Wilkinson, *IUPAC. Compendium of Chemical Terminology*, Blackwell Scientific Publications, Oxford, **1997**.

[69] J. P. Perdew, K. Burke, M. Ernzerhof, *Phys. Rev. Lett.* **1996**, *77*, 3865–3868.

[70] C. Adamo, V. Barone, *J. Chem. Phys.* **1999**, *110*, 6158–6170.

[71] R. Dovesi, A. Erba, R. Orlando, C. M. Zicovich-Wilson, B. Civalleri, L. Maschio, M. Rérat, S. Casassa, J. Baima, S. Salustro, B. Kirtman, *Wiley Interdiscip. Rev.-Comput. Mol. Sci.* **2018**, *8*, e1360.

[72] F. Weigend, R. Ahlrichs, *Phys. Chem. Chem. Phys.* **2005**, *7*, 3297–3305.

[73] A. J. Karttunen, T. Tynell, M. Karppinen, *J. Phys. Chem. C* **2015**, *119*, 13105–13114.

[74] H. J. Monkhorst, J. D. Pack, *Phys. Rev. B* **1976**, *13*, 5188–5192.

[75] A. Togo, I. Tanaka, **2018**, arXiv:1808.01590.

[76] Y. Hinuma, G. Pizzi, Y. Kumagai, F. Oba, I. Tanaka, *Comput. Mater. Sci.* **2017**, *128*, 140–184.

[77] F. Pascale, C. M. Zicovich-Wilson, F. L. Gejo, B. Civalleri, R. Orlando, R. Dovesi, *J. Comput. Chem.* **2004**, *25*, 888–897.

[78] C. M. Zicovich-Wilson, F. Pascale, C. Roetti, V. R. Saunders, R. Orlando, R. Dovesi, *J. Comput. Chem.* **2004**, *25*, 1873–1881.

[79] L. Maschio, B. Kirtman, M. Rérat, R. Orlando, R. Dovesi, *J. Chem. Phys.* **2013**, *139*, 164101.

[80] J. T. S. Irvine, D. C. Sinclair, A. R. West, *Adv. Mater 2* **1990**, *3*, 132–138.

5 $Ba_{12}[BN_2]_{6.67}H_4$ – A Disordered Anti-Skutterudite filled with Nitridoborate Anions

Published in: *Angew. Chem. Int. Ed.* **2023**, e202316469

Authors: Sophia L. Wandelt, Alexander Mutschke, Dmitry Khalyavin, Jennifer Steinadler, Antti J. Karttunen, and Wolfgang Schnick

DOI: https://doi.org/10.1002/anie.202316469

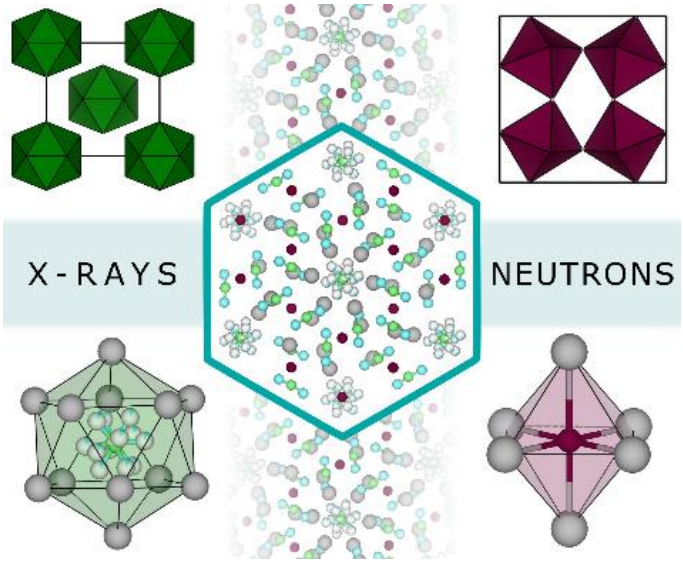

Abstract. Skutterudites are of high interest in current research due to their diversity of structures comprising empty, partially filled and filled variants, mostly based on metallic compounds. We herein present $Ba_{12}[BN_2]_{6.67}H_4$, forming a non-metallic filled anti-skutterudite. It is accessed in a solid-state ampoule reaction from barium subnitride, boron nitride and barium hydride at 750 °C. Single-crystal X-ray and neutron powder diffraction data allowed to elucidate the structure in the cubic space group $Im\bar{3}$ (no. 204). The barium and hydride atoms form a three-dimensional network consisting of corner-sharing HBa_6 octahedra and Ba_{12} icosahedra. Slightly bent $[BN_2]^{3-}$ units are located in the icosahedra and the voids in-between. ^{1}H and ^{11}B magic angle spinning (MAS) NMR experiments and vibrational spectroscopy further support the structure model. Quantum chemical calculations coincide well with experimental results and provide information about the electronic structure of $Ba_{12}[BN_2]_{6.67}H_4$.

5.1 Introduction

The class of skutterudites are of high interest in research due to their convincing thermoelectric properties.[1–3] Regular AB_3 skutterudites, such as the archetype $CoAs_3$, can be derived from the ReO_3 structure and consist of tilted corner-sharing AB_6 octahedra.[4] The tilting results in large B_{12} icosahedra, which form a body-centered cubic package. In the partially filled variant of this structure type, the crystallographic position in the center of these icosahedra is occupied. With the general sum formula LM_4X_{12}, such compounds usually consist of a rare-earth metal *L*, a transition metal *M* and a pnictogen *X*, with $LaFe_4P_{12}$ or $CeFe_4Sb_{12}$ being just two examples.[5-6] While phosphorus or antimony (*X*) form the base lattice, iron (*M*) is placed in the octahedral voids and lanthanum or cerium (*L*) inside the icosahedra. Such filled skutterudites are known as low-cost thermoelectrics.[7] For high efficiency, these materials are desired to have low thermal and high electronic conductivity. The heavy atom inside the icosahedra of filled skutterudites acts as a source for lattice phonon scattering, which reduces the thermal conductivity.[8] For example, the voids in $CoSb_3$ can be occupied to enhance its thermoelectric properties and possible n- or p-type doping of the cobalt or antimony sites allows further modification of the material.[9,10] However, the icosahedra are mostly filled with metal atoms, resulting in metal compounds or mixed compounds with metallic regions. Taking a closer look on the structure of such partially filled skutterudites, another void between the octahedra and icosahedra is noticeable. While being empty in the majority of skutterudites, it can be occupied, e.g., by triatomic anions such as an allenylide or carbodiimide unit in $Ba_{12}InC_{18}H_4$, $Ca_{12}InC_{13-x}$ and $(Ba_6N_{5/6})_2[NbN_4][CN_2]_6$.[11,12] These compounds all crystallize in an anti-type of the skutterudite structure with barium or calcium as the base lattice and hydrides, carbides and nitrides, respectively, filling the octahedral voids. In the icosahedra, metallic indium atoms or niobium nitride tetrahedra are found. Although the nitridoborate anion is isoelectronic to $[C_3]^{4-}$ and $[CN_2]^{2-}$, has similar bond lengths and often forms related structures, no skutterudites containing $[BN_2]^{3-}$ units are reported so far. Similarly, hydride skutterudites are also only little known, with metallic $Ba_{12}InC_{18}H_4$ being the solely representative. In general, skutterudite structures are widely dominated by metals or partially metallic compounds and variants without any metallic character are very sparsely explored yet.

We herein report on $Ba_{12}[BN_2]_{6.67}H_4$, the first barium nitridoborate hydride crystallizing as a non-metallic anti-skutterudite filled with $[BN_2]^{3-}$ anions. The combination of single-crystal X-ray and neutron powder diffraction experiments together with MAS NMR and vibrational spectroscopy provides a comprehensive structural analysis and allows to reliably determine light hydride ions next to heavy barium atoms. Moreover, $Ba_{12}[BN_2]_{6.67}H_4$ continues the series of reported calcium and strontium nitridoborate hydrides.

5.2 Results and Discussion

5.2.1 Synthesis and Structure Elucidation

$Ba_{12}[BN_2]_{6.67}H_4$ was obtained in a solid-state ampoule reaction at 750 °C, which yielded block-like crystals up to 100 µm in length. The precursors Ba_2N, BaH_2 and h-BN were used in a 1:1:1 ratio, implying an excess of Ba_2N and BaH_2. As Ba_2N readily reacts with the tantalum ampoule, the Ba surplus was necessary to achieve a high phase content of our compound. The synthesis temperature of 750 °C was chosen to compromise the low reactivity of BN at lower temperatures and the unwanted side reaction of Ba_2N at higher temperatures.

With single-crystal X-ray diffraction (XRD) data, the structure was partially solved (Table 5.1). As hydrogen is a very weak X-ray scatterer, the crystallographic positions of only barium, nitrogen and boron could be determined reliably. Time-of-flight neutron powder diffraction data of the isotope modified compound $Ba_{12}[^{11}BN_2]_{6.67}H_4$ were acquired to corroborate the crystal structure (Table 5.1) with the hydride ions on a fully occupied 8*c* position. To avoid neutron absorption from ^{10}B, the synthesis was performed with ^{11}B-enriched reactants. The crystallographic data of both compounds can be found in Table S5.1 and S5.2.[13] Rietveld refinement based on X-ray and neutron diffraction data of the bulk sample shows BaH_2 as a side phase (Figure S5.1 and S5.2 in the Appendix).

Table 5.1. Crystallographic data of refinements based on single-crystal X-ray and neutron powder diffraction data of $Ba_{12}[BN_2]_{6.67}H_4$ and $Ba_{12}[^{11}BN_2]_{6.67}H_4$, respectively.

formula	**$Ba_{12}[BN_2]_{6.67}H_4$**	**$Ba_{12}[^{11}BN_2]_{6.67}H_4$**
space group	$Im\bar{3}$ (no. 204)	
lattice parameters / Å	a = 11.065(3)	a = 11.0753(1)
cell volume / Å^3	1354.7(11)	1358.54(2)
formula units / unit cell	2	
molecular weight / g·mol^{-1}	1910.98	1916.13
temperature / K	293(2)	298(1)
diffractometer	Bruker D8 Venture	WISH @ ISIS
radiation	Mo-Kα (λ = 0.71973 Å)	neutrons, *time-of-flight*
refined parameters	22	45
GoF	1.216	9.191
R indices	$R1[I \geq 2\sigma(I)]$ = 0.0230 $wR2[I \geq 2\sigma(I)]$ = 0.0490 $R1$(all data) = 0.0248 $wR2$(all data) = 0.0494	R_p = 0.0211 R_{wp} = 0.0270 R_{exp} = 0.0029 R_{Bragg} = 0.0115

5.2.2 Structure Description

The crystal structure of $Ba_{12}[BN_2]_{6.67}H_4$ can be described as a stuffed anti-skutterudite with HBa_6 octahedra and Ba_{12} icosahedra, which are partially filled with disordered $[BN_2]^{3-}$ units (Figure 5.1a). In the voids between the icosahedra, additional nitridoborate units are found. The barium atoms are irregularly coordinated by two hydrogen, three boron and six nitrogen atoms (Figure 5.1b). The Ba–N and Ba–H distances are with 2.714(9)–3.100(7) and 2.930(1) Å in good agreement with comparable compounds reported in literature, which show bond lengths of 2.78–2.92 and 2.77–2.99 Å, respectively.[14–16] The nitridoborate unit outside the icosahedra is coordinated in a bicapped trigonal prism, as already found in several other nitridoborates (Figure 5.1b).[17,18] They are slightly bent with a N–B–N angle of 169.9(2)° and a B–N bond length of 1.329(9) Å, agreeing with a typical B–N distance of 1.30–1.38 Å.[19,20] $Ba_{12}InC_{18}H_4$ and $(Ba_6N_{5/6})_2[NbN_4][CN_2]_6$ are isotypic to $Ba_{12}[BN_2]_{6.67}H_4$ and feature the same anti-skutterudite

structure with similar lattice parameters (11.145 and 11.258 Å).[11,12] Rewriting their sum formulas as $Ba_{12}[In][C_3]_6H_4$, $Ba_{12}[NbN_4][CN_2]_6N_{1.67}$ and $Ba_{12}[BN_2]_{0.67}[BN_2]_6H_4$, the structural similarities become clearer. They all form similar ABa_6 octahedra (A = H^- or N^{3-}) and Ba_{12} icosahedra with either indium atoms, NbN_4 tetrahedra or $[BN_2]^{3-}$ units in the center. The voids in-between are filled with allenylide ($[C_3]^{4-}$), carbodiimide ($[CN_2]^{2-}$) or nitridoborate ($[BN_2]^{3-}$) anions, respectively, which are all isoelectronic and show similar bond lengths and angles.

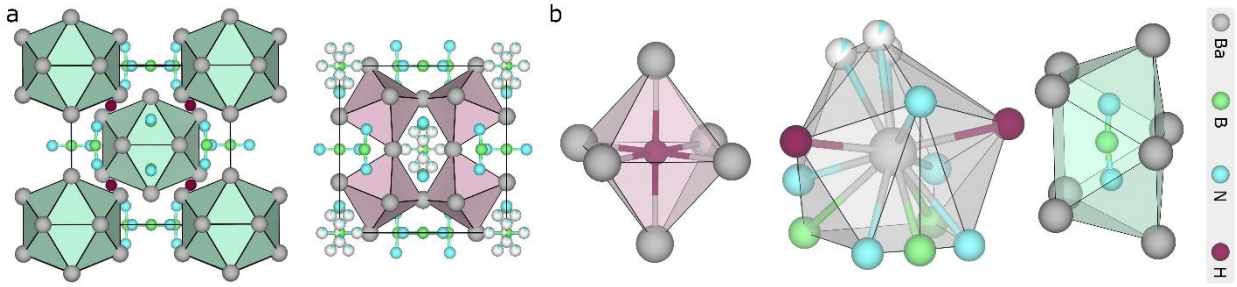

Figure 5.1. Depiction of the crystal structure of $Ba_{12}[BN_2]_{6.67}H_4$ (a) viewed along [100]. (b) HBa_6 octahedron, $Ba(B_3N_6H_2)$ polyhedron and $[BN_2]^{3-}$ unit coordinated by barium atoms in a bicapped trigonal prism. The Ba atoms and respective polyhedra are displayed in gray, B in green, N in blue and H in purple.

Taking a closer look on the nitridoborate unit inside the Ba_{12} icosahedra (Figure 5.2), both X-ray and neutron data show large displacement ellipsoids for the nitrogen atom N2. When keeping this position unoccupied, the residual electron density forms a sphere around the boron atom in the center (Figure 5.2). The "B–e^-" distance is 1.3 Å, which resembles a typical B–N bond length found in linear or slightly bent $[BN_2]^{3-}$ units.[19] We therefore assume that inside this icosahedron, the nitridoborate unit is disordered. As low temperature powder XRD measurements (Figure S5.3) do not show any ordering or change of the structure, we anticipate a statistic, not a dynamic disorder.

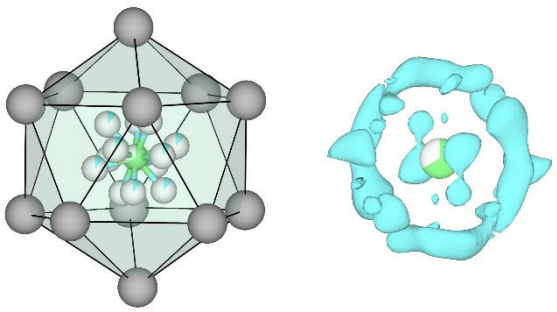

Figure 5.2. Disordered $[BN_2]^{3-}$ unit inside the Ba_{12} icosahedron (left) and residual electron density (blue) around the boron atom (green) in the center, when the nitrogen position is unoccupied. For this depiction, the crystal structure was refined in $P\bar{1}$ to reduce symmetry effects.

Due to the rather large and symmetric coordination sphere formed by the twelve barium atoms, the $[BN_2]^{3-}$ unit cannot be fixated at one position and several different orientations are energetically equivalent. For the refinements, we constrained N2 on a 24*g* position, whereas the multiplicity renders 12 possible N2 positions and therefore 6 orientations of the $[BN_2]^{3-}$ unit inside the icosahedron. In the diffraction patterns are no additional reflections at small angles visible, which renders a possible ordered variant with a superstructure as unlikely. Moreover, the isotypic compound $(Ba_6N_{5/6})_2[NbN_4][CN_2]_6$ forms the same Ba_{12} icosahedron with a disordered NbN_4 tetrahedron in the center.[12] However, to achieve charge neutrality, the whole nitridoborate unit in our salt-like compound is only to two thirds occupied. This results in 67% occupancy for B2 and 11% occupancy for N2. Due to the disorder, these site occupation factors were constrained on the respective values for both XRD and neutron refinements.

5.2.3 MAS NMR

For further validation of the proposed structure model, MAS NMR measurements were performed. The ^{1}H spectrum (Figure 5.3, left) shows a main signal at 8.2 ppm, which agrees with a single crystallographic site of hydrogen, and a broad shoulder which will be discussed below. A shift of the resonance line towards positive values of δ_{iso} is usually expected for protonic hydrogen, but it has been reported that such a chemical shift can also be observed for anionic species, depending on the metal-hydride distance.[17,21,22] We also calculated the δ_{iso} with Density Functional Theory (DFT-PBE method, GIPAW method, see Appendix for full computational details). An ordered structural model was derived for the quantum chemical calculations (further description in the Appendix). The calculated ^{1}H isotropic chemical shift for this structure model is 7.6 ppm, very close to the experimental value. The broad shoulder at around 9.5 ppm belongs to the side phase BaH_2 and an unknown impurity causes the small signal at around 1.2 ppm.

Due to the quadrupolar moment of ^{11}B (I = 3/2) and the strong anisotropy of its electronic environment, the central transition resonance in the ^{11}B spectrum (Figure 5.3, right) shows a significant second-order broadening. In principle, the structure contains two boron sites with B1 sitting on a fully occupied Wyckoff 12*e* position and B2 on 2*a* with only 67% occupancy, anticipating two signals in the NMR spectrum with a 9:1 intensity ratio. However, since the immediate chemical environment of the two crystallographic sites of boron is almost identical, we expect the positions and shape of these two signals to be very similar, resulting in only one

detectable resonance for both positions, which is indeed the case. The experimental spectrum was thus fitted with a single line shape, using the program DMFIT.[23] This provided values for the isotropic chemical shift δ_{iso} and the quadrupolar coupling constant C_Q of 25.0 ppm and 3.21 MHz, respectively. As the $[BN_2]^{3-}$ units are with an N–B–N angle of 170° only slightly bent, the asymmetry parameter η_Q obtained by the fitting routine is close to zero (0.13). These results are in good agreement with the NMR parameters for other linear or slightly bent $[BN_2]^{3-}$ units.[17,24] The isotropic ^{11}B shift calculated with the DFT-PBE method is 20.7 ppm, in reasonable agreement with the experimental δ_{iso} value.

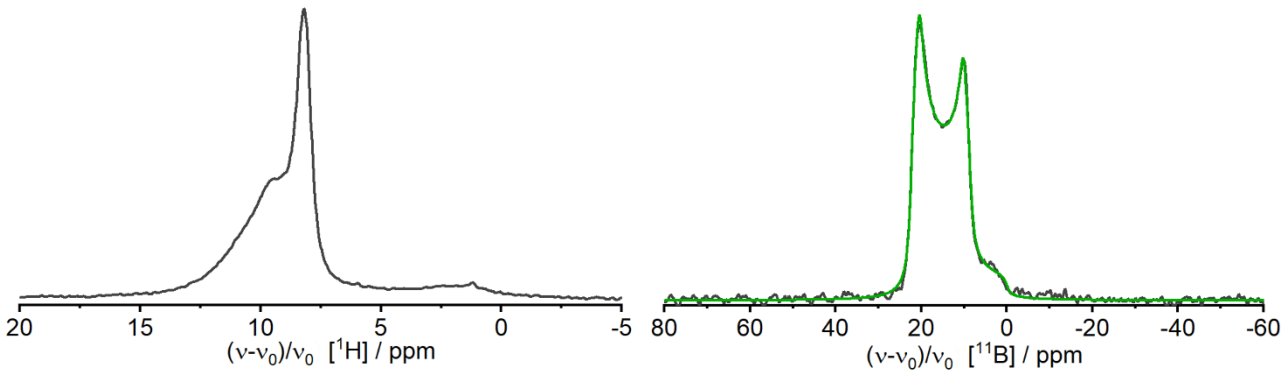

Figure 5.3. ^{1}H and ^{11}B MAS NMR spectra of $Ba_{12}[BN_2]_{6.67}H_4$ at 20 kHz spinning frequency, showing the experimental data in black and the fit of the ^{11}B signal in green.

5.2.4 Vibrational Spectroscopy

IR and Raman spectra of the title compounds were measured and compared to the respective theoretical spectrum, obtained from quantum chemical calculations with DFT-PBE0 method. The FTIR spectrum (Figure 5.4, left) is in good agreement with the simulated one, showing the expected N–B–N and Ba–H vibrations. Due to the larger coordination sphere and lower multiplicity of the nitridoborate unit in the icosahedra ($[N–B–N]_i$), its vibrations appear at smaller wavenumbers and with less intensity compared to the ones of the nitridoborate unit outside the icosahedra ($[N–B–N]_o$). Their strong antisymmetrical stretching vibrations (ν_2) are visible at 1645 and 1550 cm^{-1}. The weaker symmetrical stretching (ν_1) and bending (ν_3) arise at 1025, 590 and 565 cm^{-1}, respectively. Between 790 and 660 cm^{-1}, the Ba–H vibrations are observable. Furthermore, the full FTIR spectrum (Figure S5.4) does not show any N–H or O–H vibrations, excluding the presence of such species.

The Raman spectrum (Figure 5.4, right) shows the intense symmetrical stretching vibrations (ν_1) at 995 and 1050 cm^{-1} and the N–B–N bending (ν_3) between 580 and 630 cm^{-1}. The Ba–H vibrations appear rather broad at around 520 cm^{-1}. All N–B–N vibrations are in the expected range for linear or slightly bent $[BN_2]^{3-}$ units.[17,19,25] The assignment of the vibrations can be found in Tables S5.3 and S5.4. As allenylide and carbodiimide anions are also IR and Raman active, the spectra of the isotypic compounds $Ba_{12}InC_{18}H_4$ and $(Ba_6N_{5/6})_2[NbN_4][CN_2]_6$, show the same symmetrical and antisymmetrical stretching and bending vibrations.[11,12] Due to their different bond lengths, the vibrational bands are shifted toward higher or lower energies, respectively.

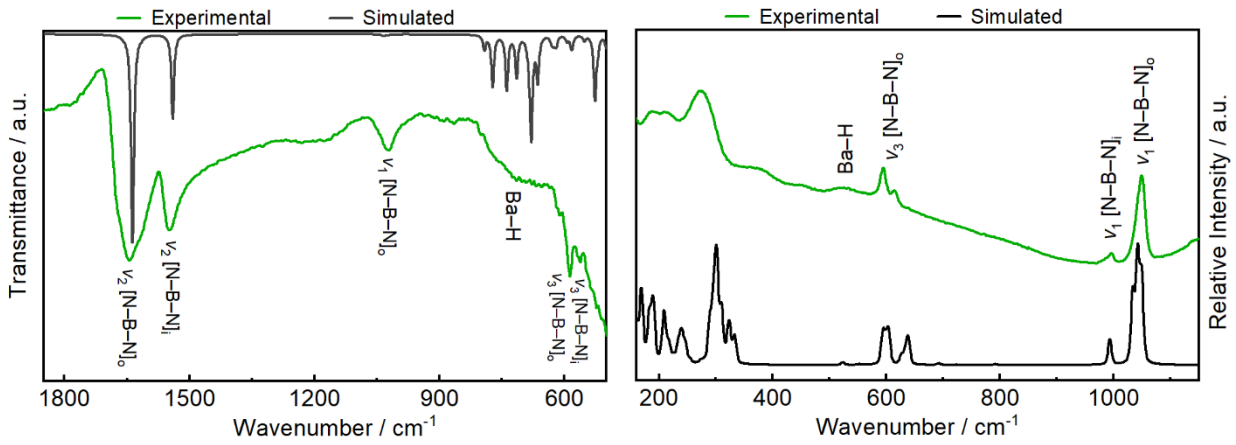

Figure 5.4. Experimental and simulated (obtained with DFT-PBE0 method) FTIR (left) and Raman (right) spectrum of $Ba_{12}[BN_2]_{6.67}H_4$, showing the Ba–H and N–B–N vibrations of the nitridoborate units inside ($[N–B–N]_i$) and outside the icosahedra ($[N–B–N]_o$).

5.2.5 Electronic Properties

To investigate the electronic structure of $Ba_{12}[BN_2]_{6.67}H_4$, quantum chemical calculations with DFT-PBE0 method were performed. To remove the disorder of the nitridoborate unit in the icosahedra, the symmetry was lowered to space group $P\bar{3}$ (no. 147). After optimizing the crystal structure of the ordered model, no imaginary frequencies were detected and the structure was determined to be relaxed at a local energetic minimum. The electronic band structure (Figure S5.5 in the Appendix) shows an indirect bandgap of 5.1 eV, agreeing with the colorless appearance of the compound, classifying it as an insulator. The projected density of states shows nitrogen at the top of the valence band, similar to other known nitridoborate hydrides.[17,26]

5.3 Conclusion

Summing up, we present the novel barium nitridoborate hydride $Ba_{12}[BN_2]_{6.67}H_4$ synthesized in a solid-state ampoule reaction. A combination of single-crystal X-ray and neutron powder diffraction data allowed elucidating the crystal structure. The title compound crystallizes as a non-metallic filled anti-skutterudite with HBa_6 octahedra and Ba_{12} icosahedra. Nitridoborate units are located in the icosahedra and the voids in-between, creating a three-dimensional network. MAS NMR measurements and vibrational spectroscopy helped to confirm the proposed structure model. The experimental results were supported by quantum chemical calculations, which also revealed the electronic structure. While most skutterudites are metallic species, $Ba_{12}[BN_2]_{6.67}H_4$ is one of very few compounds featuring non-metal atoms inside and outside the icosahedra. However, further substitution of the different motifs of such filled skutterudites opens up a large field of structurally intriguing compounds. To $[BN_2]^{3-}$ isoelectronic anions such as $[C_3]^{4-}$ and $[CN_2]^{2-}$ already formed similar structures, which can be further modified with other related building units such as $[CBN]^{4-}$ or $[BO_2]^-$. Moreover, $Ba_{12}[BN_2]_{6.67}H_4$ extends the series of nitridoborate hydrides, which have only been reported for calcium and strontium so far.

5.4 Experimental Part

5.4.1 Synthesis

All samples of $Ba_{12}[BN_2]_{6.67}H_4$ and $Ba_{12}[^{11}BN_2]_{6.67}H_4$ were synthesized from Ba_2N (31.9 mg, 0.111 mmol), BaH_2 (15.4 mg, 0.111 mmol) and BN (2.8 mg, 0.11 mmol) or ^{11}BN (2.8 mg, 0.11 mmol), respectively. The starting materials were ground and filled in a tantalum ampoule (3 cm length, 1 cm diameter), which was welded shut in an arc furnace (Handy-TIG 210 DC, LORCH, Auenwald-Mittelbrüden, Germany). The ampoule was placed in a silica tube and then heated for 15 h at 750 °C in a tube furnace (Carbolite Gero, Neuhausen, Germany). Ba_2N (Materion, 99.7%) and BaH_2 (Materion, 99.9%) were used as received. The synthesis of BN and ^{11}BN was performed in an ammonia gas flow reaction, starting with H_3BO_3 (Sigma-Aldrich, ≥ 99%) or $H_3{}^{11}BO_3$ (Sigma-Aldrich, ≥ 99% ^{11}B) using 1 equiv. of $OC(NH_2)_2$ (Sigma-Aldrich, > 99.5%) acting as a catalyst.[27] The purity of the starting materials was analyzed with powder X-ray diffraction. The preparation and analyses of the samples were performed in an Ar-filled glovebox (Unilab

MBraun, Garching H_2O < 1 ppm, O_2 < 1 ppm), because the starting materials as well as the products are air and moisture sensitive.

5.4.2 Single-Crystal XRD

To determine the crystal structure of $Ba_{12}[BN_2]_{6.67}H_4$, a single crystal was isolated and transferred into an airtight glass capillary. The data were acquired on a Bruker D8 VENTURE TXS diffractometer using Mo-Kα radiation with a rotating anode and a combination of ϕ- and ω-scans. The integration and absorption correction (multiscan method) were conducted with APEX3.[28–30] SHELXS and SHELXL were used for structure solution (direct methods) and structure refinement with the least-squares method.[31,32]

5.4.3 Powder XRD

The bulk composition of the starting materials and the products was confirmed with Powder XRD. For the measurements, the respective bulk powder was ground and sealed in a glass capillary. Diffraction data were acquired on a STOE Stadi P diffractometer using Cu-Kα_1 radiation with a Ge(111) monochromator and a Mythen1K detector in modified Debye-Scherrer geometry. Rietveld refinements were conducted using the TOPAS6 package with a fundamental parameters approach and a shifted Chebyshev polynomial for modeling the background.[33,34]

5.4.4 Neutron Powder Diffraction

For neutron powder diffraction measurements, a sample of $Ba_{12}[^{11}BN_2]_{6.67}H_4$ was transferred into a 6 mm vanadium cylinder and sealed airtight with indium wire. Although ^1H causes some incoherent scattering, it was not substituted with ^2H to obtain a better contrast between H, N and B. Time-of-flight neutron data were acquired on the WISH diffractometer at ISIS pulsed neutron source (STFC, Rutherford Appleton Laboratory, Harwell Campus, UK).[35] The Rietveld refinement of the collected pattern was conducted using the program package FullProf, with a fundamental parameters approach and a convolution of pseudo-Voigt with back-to-back exponential functions for profile fitting.[34,36] A coherent scattering length b_c = 6.65(4) fm was used for refining ^{11}B.[37]

5.4.5 MAS NMR

^{1}H and ^{11}B solid-state MAS NMR data of $Ba_{12}[BN_2]_{6.67}H_4$ were acquired in a 2.5 mm ZrO_2 rotor on a Bruker 500 AVANCE-III spectrometer operating at 500.2 MHz. The spectra were recorded at a spinning frequency of 20 kHz and indirectly referenced to ^{1}H in 100% TMS at −0.1240 ppm.

5.4.6 FTIR Spectroscopy

Infrared spectra of $Ba_{12}[BN_2]_{6.67}H_4$ were obtained using a Bruker Alpha II FTIR spectrometer with a diamond attenuated total reflectance (ATR) unit. The spectra were recorded in an Ar-filled glovebox with a resolution of 2 cm^{-1} in the range of 450–4000 cm^{-1}.

5.4.7 Raman Spectroscopy

The Raman spectrum was acquired of a powder sample of $Ba_{12}[BN_2]_{6.67}H_4$ sealed in a glass capillary by a Renishaw inVia Reflex Raman System. Spectra were obtained in the range of 100–1200 cm^{-1} using a laser with a wavelength of λ = 532 nm and a charge-coupled device detector.

5.4.8 Quantum Chemical Calculations

The geometry, electronic and vibrational properties of $Ba_{12}[BN_2]_{6.67}H_4$ were investigated by density functional theory (DFT) calculations with the DFT-PBE0 method using the CRYSTAL17 program package.[38–40] Due to the unordered nature of the compound, an ordered model had to be derived. Therefore, the surplus, partially occupied N atoms (N2, 24*g*) within the central icosahedral voids were removed, to only leave a single discrete $[BN_2]^{3-}$ unit within the respective void. This lowered the symmetry from $Im\bar{3}$ (no.204) to rhombohedral $R\bar{3}$ (no. 148) with cell parameters of a = 15.6557 and c = 9.5871 Å in the hexagonal setup. This yields a unit cell with a 50 % larger volume (Z = 2 → Z = 3). Eventually, one third of the $[BN_2]^{3-}$ units within the icosahedral voids was then removed to match the experimentally determined occupation of 0.66 within this polyhedron. The symmetry accordingly decreased from rhombohedral $R\bar{3}$ (no. 148) to trigonal $P\bar{3}$ (no. 147), giving an electron precise, ordered model. For the quantum chemical calculations, triple-ζ-valence+polarized gaussian type basis sets were used for all elements except barium, where split-valence+polarized basis sets were considered to be sufficient. The basis sets have been derived from the molecular Karlsruhe def2 basis sets and have been reported previously.[41–44] The reciprocal space of the ordered model was sampled using 2x2x4 Monkhorst-Pack-type *k*-mesh and the Coulomb and exchange integrals were evaluated by

tightened tolerance (TOLINTEG) factors of 8, 8, 8, 8 and 16.[45] The atomic positions and lattice parameters were fully optimized within the constraints of the space group symmetry. The optimized lattice parameters were determined to be a = 15.51 and c = 9.60 Å, deviating −0.92 % and +0.1 % from the ordered experimental model, respectively. For the determination of the electronic band structure, k-paths within the reciprocal space were obtained by the SeeK-path webservice.[46,47] To evaluate the harmonic frequencies and simulate the respective Raman and IR intensities, computational schemes implemented in the CRYSTAL17 program package were used.[48–50] The ordered input model did not show any imaginary frequencies, and appears as a true local energetic minimum, attributing this compound at least metastability. Raman intensities were eventually calculated for polycrystalline powder samples with an experimental Raman laser wavelength of λ = 532 nm and an measuring temperature T = 298.15 K. IR and Raman spectra were lastly simulated applying a Lorentzian profile for the IR spectrum and a pseudo-Voigt profile (50:50 – Lorentzian:Gaussian) for the Raman spectrum A FWHM of 8 cm^{-1} was used both simulations.

The solid-state NMR shielding tensors of the ordered model described above were calculated with the DFT-PBE method using the CASTEP program package and the GIPAW formalism as implemented in CASTEP-NMR.[38,51–54] Ultrasoft pseudopotentials generated with the on-the-fly scheme were applied together with a plane-wave basis set.[54] The kinetic energy cutoff was set to 630 eV. The reciprocal space was sampled using 2×2×2 Monkhorst-Pack-type k-mesh. The NMR shielding tensor was calculated at the DFT-PBE0 optimized geometry. Molecular $BF_3.Et_2O$ optimized at the DFT-PBE0/def2-TZVP level of theory was used as a reference system for calculating the ^{11}B NMR shifts.[55] The GIPAW calculations on $BF_3.Et_2O$ were carried out in a primitive orthorhombic cell (a = 19.2 Å, b = 18.3 Å, c = 18.2 Å) using a plane-wave basis set cut-off of 630 eV and Γ-point for reciprocal space sampling. The isotropic ^{11}B shielding of $BF_3.Et_2O$ is 93.42 ppm. Molecular $SiMe_4$ was used as a reference system for calculating the ^1H NMR shifts. The calculations on $SiMe_4$ were carried out in a primitive cubic cell (a = 15 Å) using a plane-wave basis set cut-off of 700 eV and Γ-point for reciprocal space sampling. The structure of the $SiMe_4$ molecule was relaxed within the T_d point group. The isotropic ^1H shielding of $SiMe_4$ is 31.01 ppm. For comparison with experimental isotropic ^1H and ^{11}B chemical shifts, the weighted average of the shifts calculated for the H and B atoms in the lower-symmetry ordered model was used. The ^1H shifts calculated for the ordered model varied between 7.2 and 7.8 ppm, while the variation for ^{11}B shifts was from 19.3 to 21.4 ppm.

5.5 Acknowledgements

The authors gratefully acknowledge the ISIS Neutron and Muon Source for granting beamtime (proposal no. 2220086), Christian Minke (Department of Chemistry, LMU Munich) for the MAS NMR measurements and Thomas Bräuniger (also LMU Munich) for helpful discussions of the resulting spectra.

5.6 References

[1] G. Rogl, P. Rogl, *Curr. Opin. Green Sustain.* **2017**, *4*, 50–57.
[2] M. Rull-Bravo, A. Moure, J. F. Fernández, M. Martín-González, *RSC Adv.* **2015**, *5*, 41653–41667.
[3] Z.-Y. Liu, J.-L. Zhu, X. Tong, S. Niu, W.-Y. Zhao, *J. Adv. Ceram.* **2020**, *9*, 647–673.
[4] N. Mandel, J. Donohue, *Acta Crystallogr.* **1971**, *B27*, 2288–2289.
[5] W. Jeitschko, D. Braun, *Acta Crystallogr.* **1977**, *B33*, 3401–3406.
[6] D. T. Morelli, G. P. Meisner, *J. Appl. Phys.* **1995**, *77*, 3777–3781.
[7] B. C. Sales, D. Mandrus, R. K. Williams, *Science* **1996**, *272*, 1325–1328.
[8] X. Shi, J. Yang, J. R. Salvador, M. Chi, J. Y. Cho, H. Wang, S. Bai, J. Yang, W. Zhang, L. Chen, *J. Am. Chem. Soc.* **2011**, *133*, 7837–7846.
[9] S. Q. Bai, Y. Z. Pei, L. D. Chen, W. Q. Zhang, X. Y. Zhao, J. Yang, *Acta Mater.* **2009**, *57*, 3135–3139.
[10] Y. Tang, Z. M. Gibbs, L. A. Agapito, G. Li, H.-S. Kim, M. B. Nardelli, S. Curtarolo, G. J. Snyder, *Nat. Mater.* **2015**, *14*, 1223–1228.
[11] T. V. Blankenship, M. J. Dickman, L. J. v. d. Burgt, S. E. Latturner, *Inorg. Chem.* **2015**, *54*, 914−921.
[12] O. Reckeweg, M. Somer, F. J. DiSalvo, *Z. Naturforsch.* **2007**, *62b*, 1246–1250.
[13] Depositions numbers 2300675 ($Ba_{12}[BN_2]_{6.67}H_4$) and 2300676 ($Ba_{12}[^{11}BN_2]_{6.67}H_4$) contain the supplementary crystallographic data for this paper. These data are provided free of charge by the joint Cambridge Crystallographic Data Centre and Fachinformationszentrum Karlsruhe Access Structures Service.
[14] F. Altorfer, W. Bührer, B. Winkler, G. Coddens, R. Essmann, H. Jacobs, *Solid State Ion.* **1994**, *70*, 272−277.
[15] F. Takeiri, A. Watanabe, A. Kuwabara, H. Nawaz, N. I. P. Ayu, M. Yonemura, R. Kanno, G. Kobayashi, *Inorg. Chem.* **2019**, *58*, 4431−4436.
[16] N. W. Falb, J. N. Neu, T. Besara, J. B. Whalen, D. J. Singh, T. Siegrist, *Inorg. Chem.* **2019**, *58*, 3302–3307.
[17] S. L. Wandelt, A. Mutschke, D. Khalyavin, J. Steinadler, W. Schnick, *Chem. Eur. J.* **2023**, e202301241.
[18] O. Reckeweg, F. J. DiSalvo, M. Somer, *J. Alloys Compd.* **2003**, *361*, 102–107.
[19] R. Pöttgen, O. Reckeweg, *Z. Kristallogr.* **2017**, *232*, 653–668.

[20] S. F. Matar, A. F. A. Alam, R. Pöttgen, *Z. Naturforsch. B* **2017**, *72*, 433–439.
[21] K. Hayashi, P. V. Sushko, Y. Hashimoto, A. L. Shluger, H. Hosono, *Nat. Commun.* **2014**, *5*, 3515.
[22] A. Mutschke, G. M. Bernard, M. Bertmer, A. J. Karttunen, C. Ritter, V. K. Michaelis, N. Kunkel, *Angew. Chem. Int. Ed.* **2021**, *60*, 5683–5687.
[23] D. Massiot, F. Fayon, M. Capron, I. King, S. L. Calvé, B. Alonso, J. O. Durand, B. Bujoli, Z. Gan, G. Hoatson, *Magn. Reson. Chem.* **2002**, *40*, 70–76.
[24] S. Seidel, T. Dierkes, T. Jüstel, C. Benndorf, H. Eckert, R. Pöttgen, *Dalton Trans.* **2016**, *45*, 12078–12086.
[25] M. Somer, Ö. Yaren, O. Reckeweg, Y. Prots, W. Carrillo-Cabrera, *Z. Anorg. Allg. Chem.* **2004**, *630*, 1068–1073.
[26] S. L. Wandelt, A. Karnas, A. Mutschke, N. Kunkel, C. Ritter, W. Schnick, *Inorg. Chem.* **2022**, *61*, 12685–12691.
[27] A. F. Holleman, N. Wiberg, *Lehrbuch der Anorganischen Chemie*, De Gruyter, Berlin, Germany, **2007**.
[28] Bruker-AXS, APEX3, Vers. 2016.5-0, Karlsruhe, Germany, **2016**.
[29] G. M. Sheldrick, SADABS Version 2: Multi-Scan Absorption Correction, Bruker-AXS, Madison, Wisconsin, USA, **2012**.
[30] Bruker-AXS, XPREP Reciprocal Space Exploration, Vers. 6.12, Karlsruhe, Germany, **2001**.
[31] G. M. Sheldrick, SHELXS - A Program for Crystal Structure Solution, University of Göttingen, Göttingen, Germany, **1997**.
[32] G. M. Sheldrick, *Acta Crystallogr.* **2008**, *A64*, 112–122.
[33] A. Coelho, TOPAS-Academic V6.1, Coelho Software, Brisbane, Australia, **2007**.
[34] H. M. Rietveld, *J. Appl. Crystallogr.* **1969**, *2*, 65–71.
[35] L. C. Chapon, P. Manuel, P. G. Radaelli, C. Benson, L. Perrott, S. Ansell, N. J. Rhodes, D. Raspino, D. Duxbury, E. Spill, J. Norris, *Neutron News* **2011**, *22*, 22–25.
[36] J. Rodriguez-Carvajal, *Physica B* **1993**, *192*, 55–69.
[37] V. F. Sears, *Neutron News* **1992**, *3*, 26–37.
[38] J. P. Perdew, K. Burke, M. Ernzerhof, *Phys. Rev. Lett.* **1996**, *77*, 3865–3868.
[39] C. Adamo, V. Barone, *J. Chem. Phys.* **1999**, *110*, 6158–6170.
[40] R. Dovesi, A. Erba, R. Orlando, C. M. Zicovich-Wilson, B. Civalleri, L. Maschio, M. Rérat, S. Casassa, J. Baima, S. Salustro, B. Kirtman, *Wiley Interdiscip. Rev.-Comput. Mol. Sci.* **2018**, *8*, e1360.
[41] F. Weigend, R. Ahlrichs, *Phys. Chem. Chem. Phys.* **2005**, *7*, 3297–3305.
[42] S. Ivlev, V. Sobolev, M. Hoelzel, A. J. Karttunen, T. Müller, I. Gerin, R. Ostvald, F. Kraus, *Eur. J. Inorg. Chem.* **2014**, *36*, 6261–6267.
[43] T. Wylezich, R. Valois, M. Suta, A. Mutschke, C. Ritter, A. Meijerink, A. J. Karttunen, N. Kunkel, *Chem. Eur. J.* **2020**, *26*, 11742–11750.
[44] A. J. Karttunen, T. Tynell, M. Karppinen, *J. Phys. Chem. C* **2015**, *119*, 13105–13114.
[45] H. J. Monkhorst, J. D. Pack, *Phys. Rev. B* **1976**, *13*, 5188–5192.
[46] A. Togo, I. Tanaka, **2018**, arXiv:1808.01590.

[47] Y. Hinuma, G. Pizzi, Y. Kumagai, F. Oba, I. Tanaka, *Comput. Mater. Sci.* **2017**, *128*, 140–184.

[48] F. Pascale, C. M. Zicovich-Wilson, F. L. Gejo, B. Civalleri, R. Orlando, R. Dovesi, *J. Comput. Chem.* **2004**, *25*, 888–897.

[49] C. M. Zicovich-Wilson, F. Pascale, C. Roetti, V. R. Saunders, R. Orlando, R. Dovesi, *J. Comput. Chem.* **2004**, *25*, 1873–1881.

[50] L. Maschio, B. Kirtman, M. Rérat, R. Orlando, R. Dovesi, *J. Chem. Phys.* **2013**, *139*, 164101.

[51] S. J. Clark, M. D. Segall, C. J. Pickard, P. J. Hasnip, M. I. J. Probert, K. Refson, M. C. Payne, *Z. Kristallogr. – Cryst. Mater.* **2005**, *220*, 567.

[52] C. J. Pickard, F. Mauri, *Phys. Rev. B* **2001**, *63*, 245101.

[53] J. R. Yates, C. J. Pickard, F. Mauri, *Phys. Rev. B* **2007**, *76*, 024401.

[54] D. Vanderbilt, *Phys. Rev. B* **1990**, *41*, 7892–7895.

[55] R. K. Harris, E. D. Becker, S. M. C. d. Menezes, R. Goodfellow, P. Granger, *Pure Appl. Chem.* **2001**, *73*, 1795–1818.

6 Conclusion and Outlook

In this work, the class of nitridoborate hydrides was expanded by four new compounds, namely Sr_2BN_2H, $Sr_{13}[BN_2]_6H_8$, $Sr_6N[BN_2]_2H_3$ and $Ba_{12}[BN_2]_{6.67}H_4$ (Figure 6.1). As discussed in Chapter 1.4, hydride, nitride and nitridoborate compounds show a distinct range of synthesis conditions. Addressing this issue, a new route to nitridoborate hydrides was established within this work. Using metal hydrides in combination with hexagonal boron nitride and metal subnitrides in a solid-state ampoule reaction provided ideal conditions to obtain the desired compounds. The subnitride is activating the inert boron nitride and the chosen temperature range of 750 to 950 °C is still low enough to avoid excessive hydrogen diffusion out of the ampoule.

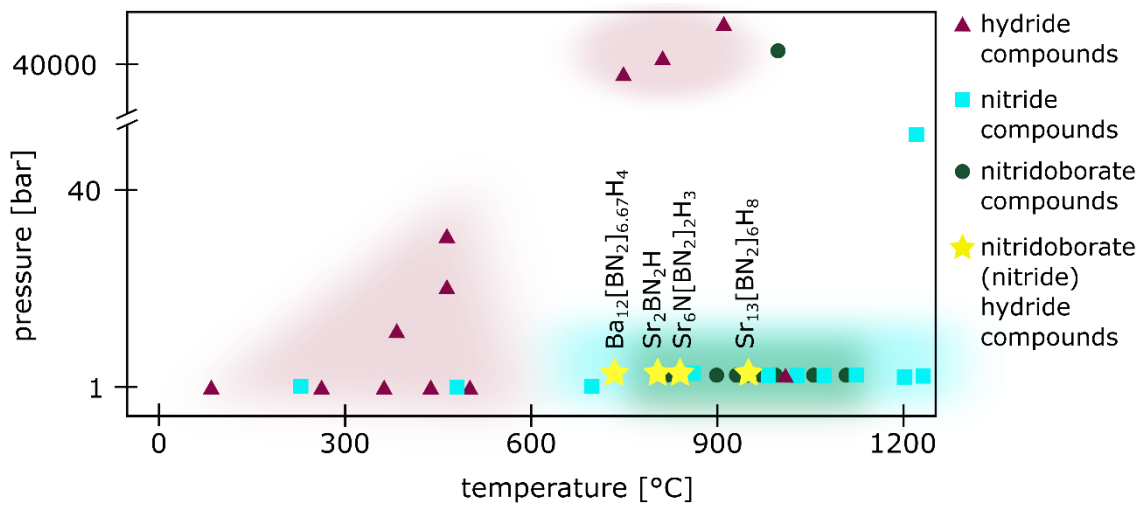

Figure 6.1. Schematic depiction of the different synthesis conditions of nitridoborate, nitride hydride and nitridoborate (nitride) hydride compounds. A full list of all nitridoborate, nitride and hydride compounds and their syntheses are found in Chapter 8.1. The synthesis conditions of the four new nitridoborate (nitride) hydride compounds are found in Chapter 2–5.

After establishing the right synthesis route, the new compounds were further examined to determine their crystal structure. A routinely workflow of X-ray and neutron diffraction, vibrational spectroscopy, and MAS NMR measurements as well as quantum chemical calculations was conducted to characterize each compound. First, the structure solution was performed based on single-crystal X-ray diffraction data, refining all atoms except hydrogen. Due to its low X-ray scattering power, neutron powder diffraction data were essential to determine the crystallographic positions of the hydride atoms reliably. To avoid incoherent scattering and

neutron absorption from ^{1}H and ^{10}B, respectively, the compounds were synthesized with ^{2}H and ^{11}B. Second, vibrational spectroscopy was performed to support the proposed structure models. The characteristic N–B–N as well as the Sr–H/N or Ba–H stretching and bending vibrations were observed and compared with the respective simulated spectra, obtained by DFT calculations at the PBE0 level of theory. Third, ^{1}H and ^{11}B MAS NMR measurements were conducted to further validate the presence of hydrogen and boron in the structure and their number of crystallographic positions. Moreover, a fit of the signal in the ^{11}B spectrum allowed to determine the isotropic chemical shift δ_{iso}, the quadrupolar coupling constant C_Q and the asymmetry parameter η_Q. Although ^{11}B NMR spectroscopy is a commonly used analysis method for boron compounds, mostly trigonally or tetrahedrally coordinated boron is examined.[1] A closer investigation and calculation of the NMR parameters of linear or slightly bent $[BN_2]^{3-}$ units are only once reported so far.[2] In this work, the isotropic shift of four new compounds containing twofold coordinated boron was calculated (Figure 6.2).

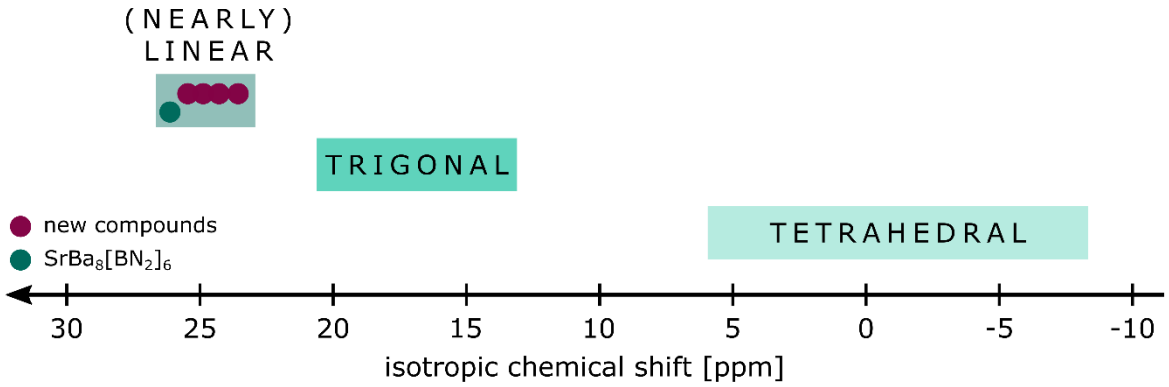

Figure 6.2. ^{11}B isotropic chemical shift ranges for tetrahedral and trigonal coordination environments as well as the values of the reported compound $SrBa_8[BN_2]_6$ (δ_{iso} = 26.6 ppm) and the four new compounds Sr_2BN_2H (23.6 ppm), $Sr_{13}[BN_2]_6H_8$ (25.2 ppm), $Sr_6N[BN_2]_2H_3$ (24.3 ppm) and $Ba_{12}[BN_2]_{6.67}H_4$ (25.0 ppm).[1,2]

To conclude the structural analysis of the new compounds, quantum chemical calculations at the PBE0 level of theory were performed to investigate the electronic structure. All four appeared as insulators with a direct or indirect bandgap of 4 to 5 eV and showed nitrogen at the top of the valence band of the projected density of states.

Taking a closer look on the sum formulas of these new compounds, it becomes obvious that – next to their similar precursor ratios and synthesis temperatures – they all have a very similar stoichiometry (Figure 6.3). The *AE*:[BN_2]:H ratio is around 2:1:1 with $Sr_{13}[BN_2]_6H_8$ and $Sr_6N[BN_2]_2H_3$ being hydride richer, whereas $Ba_{12}[BN_2]_{6.67}H_4$ has a higher nitridoborate content. However, all compounds crystallize in a different structure type, with $Sr_{13}[BN_2]_6H_8$ even building an unknown structure type and $Sr_6N[BN_2]_2H_3$ and $Ba_{12}[BN_2]_{6.67}H_4$ building new variants of known structures. Despite the same building units and repeating coordination environments of the present anions and cations, the resulting three-dimensional networks differ significantly.

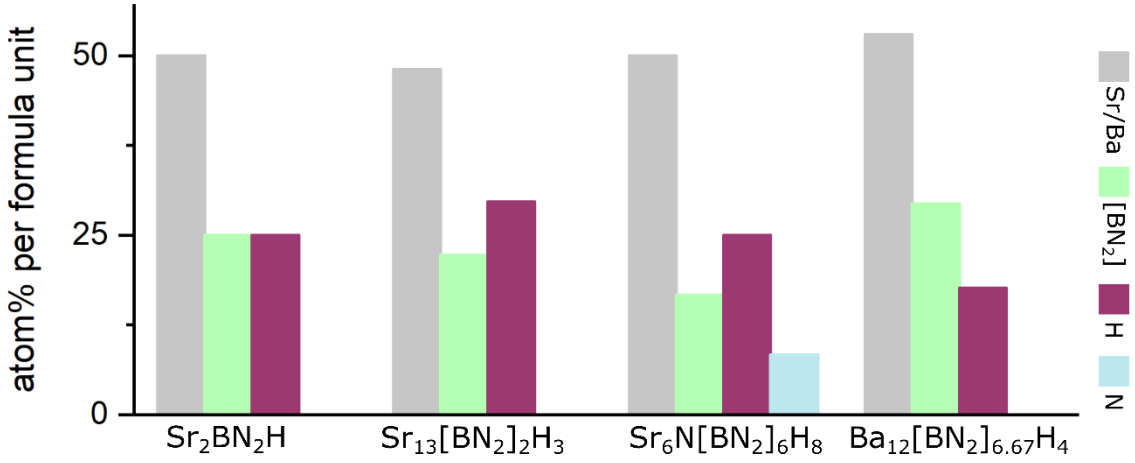

Figure 6.3. Comparison of the atom percentage per formula unit of the different structural building units in the four new compounds.

The first strontium nitridoborate hydride Sr_2BN_2H extends the series Sr_2BN_2X with *X* = F, Cl, Br, I. In agreement with the known hydride-fluoride analogy, Sr_2BN_2H and Sr_2BN_2F crystallize isotypically in the space group *Pnma* (no. 62), while the other halide compounds all form their own structure type.[3–5] Despite their same stoichiometry, the coordination environments of the anions vary. Within the series H/F–Cl–Br–I, the coordination number of the $[BN_2]^{3-}$ unit decreases from 8 (bicapped trigonal prism) to 6 (trigonal antiprism). At the same time, the coordination of the halide increases from 4 (tetrahedral) to 6 (octahedral) with increasing radius. Of the M_2BN_2H series, only the isotypic calcium compound has been investigated so far.[6] Although some nitridoborate halides of magnesium and barium are already known, no hydridic compound was reported as yet.

The second strontium nitridoborate hydride $Sr_{13}[BN_2]_6H_8$, however, forms its own structure type with no halide relatives. Crystallizing in the hexagonal space group $P6_3/m$ (no. 176), it has a highly symmetric network with trigonally planar and tetrahedrally coordinated hydrides and slightly bent $[BN_2]^{3-}$ units in a bicapped trigonal prism.

The third compound in this series, $Sr_6N[BN_2]_2H_3$, is not only a nitridoborate hydride but also contains isolated nitride ions. Among the group of multianionic metal hydrides, containing two more distinct anions, it is the first compound that is oxide-free and includes a complex anion. It shows a novel three-dimensional network with connected layers of N^{3-} and H^- ions, strontium cations and $[BN_2]^{3-}$ units. Moreover, the hydride ions are allowed to migrate along these layers, resulting in hydride ion conductivity at elevated temperatures.
The fourth compound in the row and the first barium nitridoborate hydride $Ba_{12}[BN_2]_{6.67}H_4$ shows a highly symmetric cubic structure and octahedrally coordinated hydride ions and Ba_{12} icosahedra. The structure type can be defined as a filled anti-skutterudite, in which barium and hydrogen build the main structure and the $[BN_2]^{3-}$ units occupy the icosahedra as well as the free voids in-between. However, the well-explored skutterudites mainly consist of metallic compounds with empty icosahedra and such a stuffed version with non-metals is rather unusual.

Although the class of nitridoborate (nitride) hydrides was expanded significantly through this work, there is still an open field of structural and functional intriguing materials. As hydrides tend to build fluoride-analogue structures and nitridoborates have manifold isoelectronic relatives, their combination provides an infinite pool of possibilities to generate novel compounds with known structural motifs. Moreover, the nitridoborate (nitride) hydrides in this work were only focused on calcium, strontium and barium: the incorporation of lanthanides or even transition metals could further lead to new materials. Next to diverse structural moieties, the practical application of nitridoborates bears a promising potential; acting as a proof-of-principle, $Sr_6N[BN_2]_2H_3$ set the first milestone for hydride ion conducting materials in this compound class. Additionally, hydrides, nitrides and nitridoborates are known for their luminescent properties upon doping with lanthanides, which makes the group of nitridoborate hydrides even more worthwhile for further investigations.

Considering the distinct synthetic routes of hydrides, nitrides and nitridoborates, the solid-state ampoule reaction proved itself as suitable for the reported new compounds. However, high-pressure high-temperature syntheses already yielded various materials containing hydride, nitride or nitridoborate anions on their own. As the temperatures are high enough to activate the inert boron nitride and the high partial pressure restricts hydrogen diffusion out of the crucible, this method has a high potential to unite these three distinct anions. Choosing the right precursors and synthesis conditions could lead to novel compounds with unforeseen structures and functionalities.

References:

[1] T. Bräuniger, M. Jansen, *Z. Anorg. Allg. Chem.* **2013**, *639*, 857–879.

[2] S. Seidel, T. Dierkes, T. Jüstel, C. Benndorf, H. Eckert, R. Pöttgen, *Dalton Trans.* **2016**, *45*, 12078–12086.

[3] F. Rohrer, R. Nesper, *J. Solid State Chem.* **1998**, *135*, 194–200.

[4] I. Kokal, U. Aydemir, Y. Prots, W. Schnelle, L. Akselrud, P. Höhn, M. Somer, *Z. Kristallogr.* **2011**, *226*, 633–639.

[5] F. E. Rohrer, R. Nesper, *J. Solid State Chem.* **1999**, *142*, 187–191.

[6] M. Somer, Ö. Yaren, O. Reckeweg, Y. Prots, W. Carrillo-Cabrera, *Z. Anorg. Allg. Chem.* **2004**, *630*, 1068–1073.

7 Summary

7.1 Strontium Nitridoborate Hydride Sr_2BN_2H Verified by Single-Crystal X-ray and Neutron Powder Diffraction

Sophia L. Wandelt, Ayla Karnas, Alexander Mutschke, Nathalie Kunkel, Clemens Ritter, and Wolfgang Schnick, *Inorg. Chem.* **2022**, *61*, 12685–12691

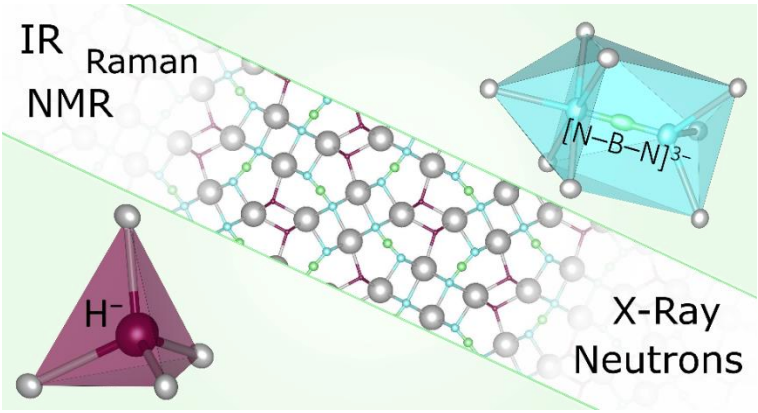

The combination of different anions in one materials allows tuning its physical and structural properties. As the nitridoborate and the hydride anion are substantial different regarding their syntheses and stabilities, their combination is rather unusual. After only one known member of this class, our compound Sr_2BN_2H is the second nitridoborate hydride to date. It was accessed in a solid-state reaction of Sr_2N, SrH_2 and BN at 850 °C as a gray, air- and moisture-sensitive powder. The crystal structure was partially solved from single-crystal X-ray diffraction data in the orthorhombic space group *Pnma* (no. 62) with a = 9.9164(2), b = 3.9079(1) and c = 10.1723(2) Å. It consists of a three-dimensional network of strontium ions and $[BN_2]^{3-}$ units. Neutron Powder diffraction data corroborated the structure model and revealed the positions of the hydride ions in the channels of the network. ^{1}H and ^{11}B magic angle spinning NMR further validate the structure model and FTIR as well as Raman spectroscopy measurements exhibit expected B–N and hydride vibrations. Quantum chemical calculations support the experimental findings and reveal the electronic structure of Sr_2BN_2H.

7.2 A Novel Nitridoborate Hydride $Sr_{13}[BN_2]_6H_8$ Elucidated from X-ray and Neutron Diffraction Data

Sophia L. Wandelt, Alexander Mutschke, Dmitry Khalyavin, Jennifer Steinadler, and Wolfgang Schnick, *Chem. Eur. J.* **2023**, e202301241

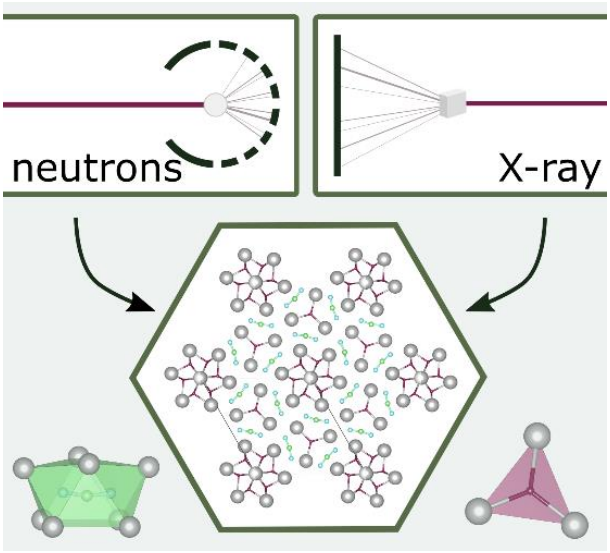

Metal hydrides convince with a variety of structural and functional materials, gaining interest over the last decades. The hydride anion only has two electrons and is therefore usually not reliably detectable with X-ray diffraction experiments. As neutrons interact with the core of the atom, it is possible to determine the crystallographic positions of hydrogen with neutron diffraction. Using this technique, it was possible to elucidate the structure of our new nitridoborate hydride $Sr_{13}[BN_2]_6H_8$. Being the third nitridoborate hydride so far, it further expands this little-explored compound class. Single-crystal X-ray diffraction data allowed to solve the structure in the hexagonal space group $P6_3/m$ (no. 176) with a = 13.6724(3) and c = 3.8831(1) Å. Neutron powder diffraction data revealed two crystallographic positions of hydride ions, building a three-dimensional network with the strontium ions and $[BN_2]^{3-}$ units. ^1H and ^{11}B Magic angle spinning NMR further validate our structure model with expectedly one signal for each crystallographic position. FTIR and Raman spectroscopy show typical B–N and hydride vibrations. Quantum chemical calculations support the experimental outcome and provide insight in the electronic structure of $Sr_{13}[BN_2]_6H_8$.

7.3 Combining Nitridoborates, Nitrides and Hydrides – Synthesis and Characterization of the Multianionic $Sr_6N[BN_2]_2H_3$

Sophia L. Wandelt, Alexander Mutschke, Dmitry Khalyavin, Robert Calaminus, Jennifer Steinadler, Bettina V. Lotsch, and Wolfgang Schnick, *Angew. Chem. Int. Ed.* **2023**, e202313564

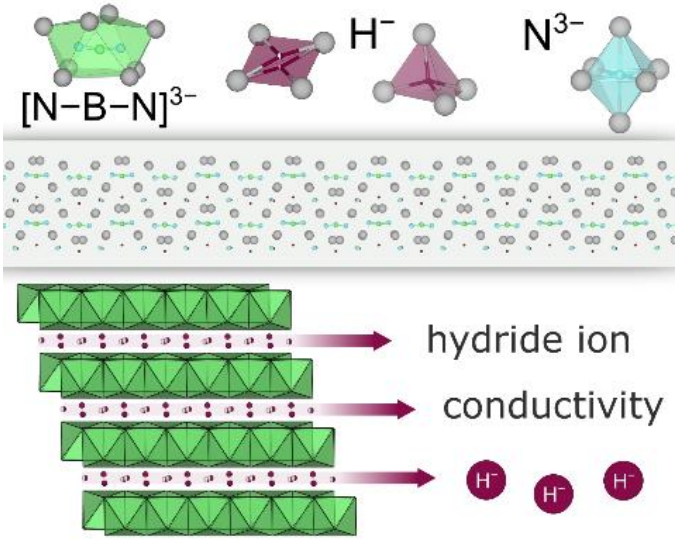

The compound class of metal hydrides attracted growing interest over the last decades, demonstrating their widespread applicability with intriguing features such as hydrogen storage capacity, magnetism or high hydride ion conductivity. Moreover, due to the large range of coordination spheres and bonding partners of the hydride anion, metal hydrides exhibit a vast variety of structural motifs. Being the first compound to simultaneously contain $[BN_2]^{3-}$, N^{3-} as well as H^- anions, the novel compound $Sr_6N[BN_2]_2H_3$ further expands the structural diversity of metal hydrides. Its crystal structure was elucidated from single-crystal X-ray and neutron powder diffraction data in the space group $P2_1/c$ (no. 14) with a = 6.6778(8) Å, b = 11.387(1) Å, c = 7.7311(9) Å and β = 107.459(5)°. The three-dimensional network shows a layer-like structure with undulated planes of strontium cations, nitridoborate anions and nitride together with hydride anions. Along these layers, the hydride ions seem to migrate through the crystal lattice, which was supported by electrochemical impedance spectroscopy measurements. Magic angle spinning NMR and vibrational spectroscopy further corroborate the structural analysis of our compound. Additionally, quantum chemical calculations provide information about the electronic structure and support the experimental outcome.

7.4 $Ba_{12}[BN_2]_{6.67}H_4$ – A Disordered Anti-Skutterudite filled with Nitridoborate Anions

Sophia L. Wandelt, Alexander Mutschke, Dmitry Khalyavin, Jennifer Steinadler, Antti J. Karttunen, and Wolfgang Schnick, *Angew. Chem. Int. Ed.* **2023**, e202316469

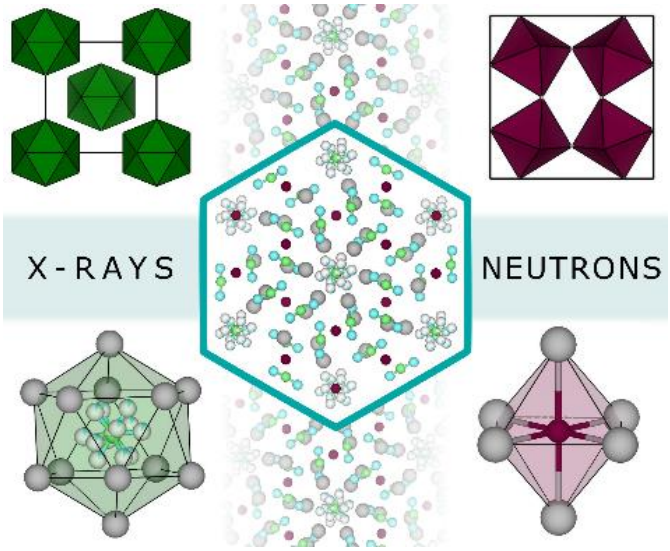

The family of skutterudites caught growing attention over the last years, comprising a diversity of structures with empty, partially filled and filled variants. Derived from the ReO_3 type, classic AB_3 skutterudites comprise tilted corner-sharing AB_6 octahedra, which result in empty B_{12} icosahedra. The latter are often occupied by additional metals or non-metals to modify the structure. Between the octahedra and icosahedra, other voids are present, which remain empty in the majority of such structures. However, skutterudites are primarily formed by metals, resulting in intermetallic phases or mixed compounds with metallic regions. $Ba_{12}[BN_2]_{6.67}H_4$ is the first barium nitridoborate hydride and crystallizes as a non-metallic filled anti-skutterudite. Single-crystal X-ray and neutron powder diffraction data allowed elucidating the crystal structure in the space group $Im\bar{3}$ (no. 204) with a = 11.065(3) Å. The structure consists of corner-sharing HBa_6 octahedra and Ba_{12} icosahedra, whereas nitridoborate units occupy the icosahedra and the voids in-between. Vibrational spectroscopy and magic angle spinning NMR measurements further confirm the structural motifs. Quantum chemical calculations support the experimental findings and show the electronic structure of $Ba_{12}[BN_2]_{6.67}H_4$.

8 Appendix

8.1 Supporting Information for Chapter 1

Table S1.1. List of the mentioned triatomic $[A–B–C]^{x–}$ anions with typical bond lengths and angles.

sum formula	name	bond lengths / Å	*A–B–C* angle / °	references
$[N_3]^-$	azide	1.15–1.17	180	[1,2]
$[OCN]^-$	cyanate	1.16–1.21	180	[2,3]
$[CNO]^-$	fulminate	1.13–1.27	180	[4]
$[CN_2]^{2-}$	carbodiimide	1.21–1.24	168–180	[5–7]
$[BO_2]^-$	borate	1.21–1.26	180	[8,9]
$[C_3]^{4-}$	allenylide	1.30–1.35	169–171	[10–11]
$[BN_2]^{3-}$	nitridoborate	1.31–1.39	186–180	[12]
$[CBN]^{4-}$	carbonitridoborate	1.35–1.44	175–180	[13,14]
$[BC_2]^{5-}$	carboborate	1.44–1.48	164–180	[15,16]

Table S1.2. List of nitridoborate compounds with their respective synthesis temperature and pressure.

compound(s)	temperature / °C	pressure	reference
Li_3BN_2	800	–	[17]
$Li_4Ba[BN_2]_2$	900	–	[18]
Ca_2BN_2F, Ca_2BN_2Cl, Sr_2BN_2F, Sr_2BN_2Cl	1000	–	[19]
Sr_2BN_2Br, Eu_2BN_2Br, Eu_2BN_2I	1000	–	[20]
$Ba_8[BN_2]_5F$	1000	–	[21]
Li_3BN_2, $Ca_3[BN_2]_2$, $Ba_3[BN_2]_2$	1000	–	[22]
Na_3BN_2	1000	4 GPa	[23]
$Mg_6Al_2[BN_2]_2N_4$, $Mg_7Si[BN_2]_2N_4$	1100	–	[24]
$SrBa_8[BN_2]_6$, $EuBa_8[BN_2]_6$	1100	–	[25]

Table S1.3. List of hydride compounds with their respective synthesis temperature and pressure.

compound	temperature / °C	pressure	reference
$Sr_5(BO_3)_3H$	RT	–	[26]
Ba_5CrN_4H	220	–	[27]
Sr_2LiNH_2	330	–	[28]
Na_3SO_4H	330	20 bar	[29]
$BaCeO_{3-x}N_yH_z$	400	–	[30]
$LiSrH_{3-x}F_x$	460	30 bar	[31]
NaH_xF_{1-x}	460	40 bar	[32]
$Sr_5(PO_4)_3H$	500	–	[33]
Mg_2NiH_4	750	2 GPa	[34]
Ba_2ScHO_3	800	3 GPa	[35]
$BaCrO_2H$	900	6 GPa	[36]
Ca_3SiN_3H	1050	–	[37]

Table S1.4. List of nitride compounds with their respective synthesis temperature and pressure.

compound	temperature / °C	pressure	reference
Ti_2AlN	1400	45 MPa	[38]
$Ba_5[CrN_4]N$	700	–	[39]
Ca_2NCl, Ca_2NBr	1120	–	[40]
$ZnGeN_2$	880	–	[41]
ZrNBr, ZrNI, HfNBr, HfNI	1050	4 GPa	[42]
Be_3N_2, Mg_3N_2, Ca_3N_2	1000, 1300	–	[43]
Cu_3N	250	–	[44]
Si_3N_4	1350	–	[45]
CeN	1000	–	[46]
CrN	385	–	[47]

References

[1] G. E. Pringle, D. E. Noakes, *Acta Crystallogr.* **1968**, *B24*, 262–269.

[2] S. B. Hendricks, L. Pauling, *J. Am. Chem. Soc.* **1925**, *47*, 2904–2920.

[3] E. Hennings, H. Schmidt, W. Voigt, *Z. Anorg. Allg. Chem.* **2011**, *637*, 1199–1202.

[4] W. Beck, *Eur. J. Inorg. Chem.* **2003**, *24*, 4275–4288.

[5] X. Liu, M. Krott, P. Müller, C. Hu, H. Lueken, R. Dronskowski, *Inorg. Chem.* **2005**, *44*, 3001−3003.

[6] O. Reckeweg, M. Somer, F. J. DiSalvo, *Z. Naturforsch.* **2007**, *62b*, 1246–1250.

[7] A. Williams, I. T. Ibrahim, *Chem. Rev.* **1981**, *81*, 589–636.

[8] H. A. Höppe, *Z. Naturforsch.* **2015**, *70*, 769–774.

[9] C. Huang, M. Mutailipu, F. Zhang, K. J. Griffith, C. Hu, Z. Yang, J. M. Griffin, K. R. Poeppelmeier, S. Pan, *Nat. Commun.* **2021**, *12*, 2597.

[10] T. V. Blankenship, M. J. Dickman, L. J. v. d. Burgt, S. E. Latturner, *Inorg. Chem.* **2015**, *54*, 914−921.

[11] H.-J. Meyer, *Z. Anorg. Allg. Chem.* **1991**, *593*, 186–192.

[12] R. Pöttgen, O. Reckeweg, *Z. Kristallogr.* **2017**, *232*, 653–668.

[13] M. Wörle, H. M. z. Altenschildesche, R. Nesper, *J. Alloys Compd.* **1998**, *264*, 107–114.

[14] H.-J. Meyer, *Z. Anorg. Allg. Chem.* **1991**, *594*, 113–118.

[15] H. Hillebrecht, F. D. Meyer, *Angew. Chem. Int. Ed.* **1996**, *35*, 2499–2500.

[16] O. Reckeweg, H.-J. Meyer, *Angew. Chem. Int. Ed.* **1998**, *37*, 3407–3410.

[17] K. Sahni, M. Ashuri, S. Emani, J. A. Kaduk, K. Németh, L. L. Shaw, *Ceram. Int.* **2018**, *44*, 7734–7740.

[18] S. Seidel, M. Somer, K. Kiraz, U. C. Rodewald, R. Pöttgen, *Z. Anorg. Allg. Chem.* **2017**, *643*, 1831–1835.

[19] F. Rohrer, R. Nesper, *J. Solid State Chem.* **1998**, *135*, 194–200.

[20] I. Kokal, U. Aydemir, Y. Prots, W. Schnelle, L. Akselrud, P. Höhn, M. Somer, *Z. Kristallogr.* **2011**, *226*, 633–639.

[21] F. E. Rohrer, R. Nesper, *J. Solid State Chem.* **1998**, *142*, 192–198.

[22] M. Somer, *Z. Naturforsch.* **1991**, *46b*, 1664–1668.

[23] J. Evers, M. Münsterkötter, G. Oehlinger, K. Polborn, B. Sendlinger, *J. Less-Common Met.* **1990**, *162*, L17.

[24] M. Ströbele, K. Dolabdjian, D. Enseling, D. Dutczak, B. Mihailova, T. Jüstel, H.-J. Meyer, *Eur. J. Inorg. Chem.* **2015**, *10*, 1716–1725.

[25] S. Seidel, T. Dierkes, T. Jüstel, C. Benndorf, H. Eckert, R. Pöttgen, *Dalton Trans.* **2016**, *45*, 12078–12086.

[26] T. Wylezich, R. Valois, M. Suta, A. Mutschke, C. Ritter, A. Meijerink, A. J. Karttunen, N. Kunkel, *Chem. Eur. J.* **2020**, *26*, 11742–11750.

[27] Y. Guan, W. Zhang, Q. Wang, C. Weidenthaler, A. Wu, W. Gao, Q. Pei, H. Yan, J. Cui, H. Wu, S. Feng, R. Wang, H. Cao, X. Ju, L. Liu, T. He, J. Guo, P. Chen, *Chem Catal.* **2021**, *1*, 1042–1054.

[28] D. M. Liu, Q. Q. Liu, T. Z. Si, Q. A. Zhang, *J. Alloys Compd.* **2010**, *495*, 272–274.

[29] A. Mutschke, G. M. Bernard, M. Bertmer, A. J. Karttunen, Clemens Ritter, V. K. Michaelis, N. Kunkel, *Angew. Chem. Int. Ed.* **2021**, *60*, 5683–5687.

[30] M. Kitano, J. Kujirai, K. Ogasawara, S. Matsuishi, T. Tada, H. Abe, Y. Niwa, H. Hosono, *J. Am. Chem. Soc.* **2019**, *141*, 20344–20353.

[31] N. Kunkel, H. Kohlmann, *J. Phys. Chem. C* **2016**, *120*, 10506−10511.

[32] T. D. Humphries, D. A. Sheppard, M. R. Rowles, M. V. Sofianos, C. E. Buckley, *J. Mater. Chem. A* **2016**, *4*, 12170–12178.

[33] A. Mutschke, T. Wylezich, C. Ritter, A. J. Karttunen, N. Kunkel, *Eur. J. Inorg. Chem.* **2019**, *48*, 5073–5076.

[34] R. Martínez-Coronado, M. Retuerto, B. Torres, M. J. Martínez-Lope, M. T. Fernández-Díaz, J. A. Alonso, *Int. J. Hydrog. Energy* **2013**, *38*, 5738−5745.

[35] F. Takeiri, A. Watanabe, A. Kuwabara, H. Nawaz, N. I. P. Ayu, M. Yonemura, R. Kanno, G. Kobayashi, *Inorg. Chem.* **2019**, *58*, 4431−4436.

[36] K. Higashi, M. Ochi, Y. Nambu, T. Yamamoto, T. Murakami, N. Yamashina, C. Tassel, Y. Matsumoto, H. Takatsu, C. M. Brown, H. Kageyama, *Inorg. Chem.* **2021**, *60*, 11957−11963.

[37] M. J. Dickman, B. V. G. Schwartz, S. E. Latturner, *Inorg. Chem.* **2017**, *56*, 9361–9368.

[38] N. J. Lane, S. C. Vogel, M. W. Barsoum, *J. Am. Ceram. Soc.* **2011**, *94*, 3473–3479.

[39] A. Tennstedt, R. Kniep, M. Hüber, W. Haase, *Z. Anorg. Allg. Chem.* **1995**, *621*, 511–515.

[40] A. Bowman, R. I. Smith, D. H. Gregory, *J. Solid State Chem*. **2005**, *178*, 1807–1817.

[41] Q.-H. Zhang, J. Wang, C.-W. Yeh, W.-C. Ke, R.-S. Liu, J.-K. Tang, M.-B. Xie, H.-B. Liang, Q. Su, *Acta Mater.* **2010**, *58*, 6728–6735.

[42] X. Chen, H. Fukuoka, S. Yamanaka, *J. Solid State Chem.* **2002**, *163*, 77–83.

[43] O. Reckeweg, F. J. DiSalvo, *Z. Anorg. Allg. Chem.* **2001**, *627*, 371–377.

[44] G. Paniconi, Z. Stoeva, H. Doberstein, R. I. Smith, B. L. Gallagher, D. H. Gregory, *Solid State Sci.* **2007**, *9*, 907–913.

[45] O. Glemser, K. Beltz, P. Naumann, *Z. Anorg. Allg. Chem.* **1957**, *291*, 51–66.

[46] H. Holleck, E. Smailos, F. Thümmler, *J. Nucl. Mater.* **1968**, *28*, 105–109.

[47] M. Widenmeyer, E. Meissner, A. Senyshyn, R. Niewa, *Z. Anorg. Allg. Chem.* **2014**, *640*, 2801–2808.

8.2 Supporting Information for Chapter 2

Table S2.1. Data of the Rietveld refinement based on powder XRD data from the Sr_2BN_2H bulk sample. Standard deviations are given in parentheses.

sum formula	**Sr_2BN_2H**
formula weight / g·mol^{-1}	215.08
crystal system	orthorhombic
space group	*Pnma* (no. 62)
lattice parameters / Å	*a* = 9.92597(7)
	b = 3.91269(3)
	c = 10.18142(8)
volume / Å^3	395.42(5)
Z	4
X-ray density / g·cm^{-3}	3.6127
diffractometer	STOE Stadi P
radiation	Cu-$K\alpha_1$ (λ = 1.54059 Å)
monochromator	Ge(111)
detector	Mythen1K
2ϑ range / °	5 ≤ 2ϑ ≤ 120
data points	7705
number of reflections	352
refined parameters	54
background function	shifted Chebyshev, 14 polynomials
R indices	R_p = 0.0545
	R_{wp} = 0.0777
	R_{exp} = 0.0375
	R_{Bragg} = 0.0248
GoF (χ^2)	2.0705

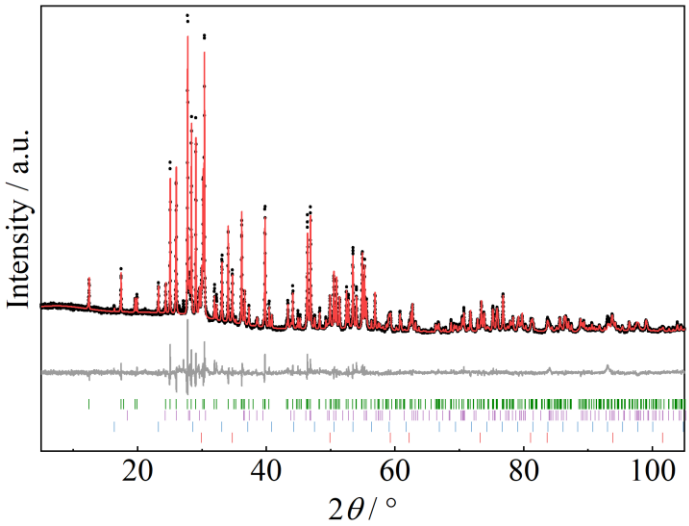

Figure S2.1. Rietveld refinement of powder XRD data of the bulk sample of $Sr_2{}^{11}BN_2D_{0.86}H_{0.14}$ prepared for neutron diffraction experiments (Cu-$K\alpha_1$ radiation, λ = 1.54059 Å). The black, red and gray lines indicate the experimental and calculated data and their difference, respectively. The Bragg markers denote from top to bottom: $Sr_2{}^{11}BN_2D_{0.86}H_{0.14}$ (79.9(5) wt %), SrO (7.4(2) wt %), $Sr_3B_2N_4$ (6.4(3) wt %) and SrD_2 (6.3(4) wt %).

Table S2.2. Details of the Rietveld refinement based on powder XRD data from the $Sr_2{}^{11}BN_2D_{0.86}H_{0.14}$ bulk sample. Standard deviations are given in parentheses.

sum formula	**$Sr_2{}^{11}BN_2D_{0.86}H_{0.14}$**
formula weight / g·mol^{-1}	216.28
crystal system	orthorhombic
space group	*Pnma* (no. 62)
lattice parameters / Å	*a* = 9.9229(1) *b* = 3.91394(5) *c* = 10.1841(1)
volume / Å^3	395.53(1)
Z	4
X-ray density / g·cm^{-3}	3.6198
diffractometer	STOE Stadi P
radiation	Cu-$K\alpha_1$ (λ = 1.54059 Å)
monochromator	Ge(111)
Detector	Mythen1K
2ϑ range / °	5 ≤ 2ϑ ≤ 120
data points	7705
number of reflections	352
refined parameters	52
background function	shifted Chebyshev, 14 polynomials
R indices	R_p = 0.0502 R_{wp} = 0.0708 R_{exp} = 0.0430 R_{Bragg} = 0.0264
GoF (χ^2)	1.6461

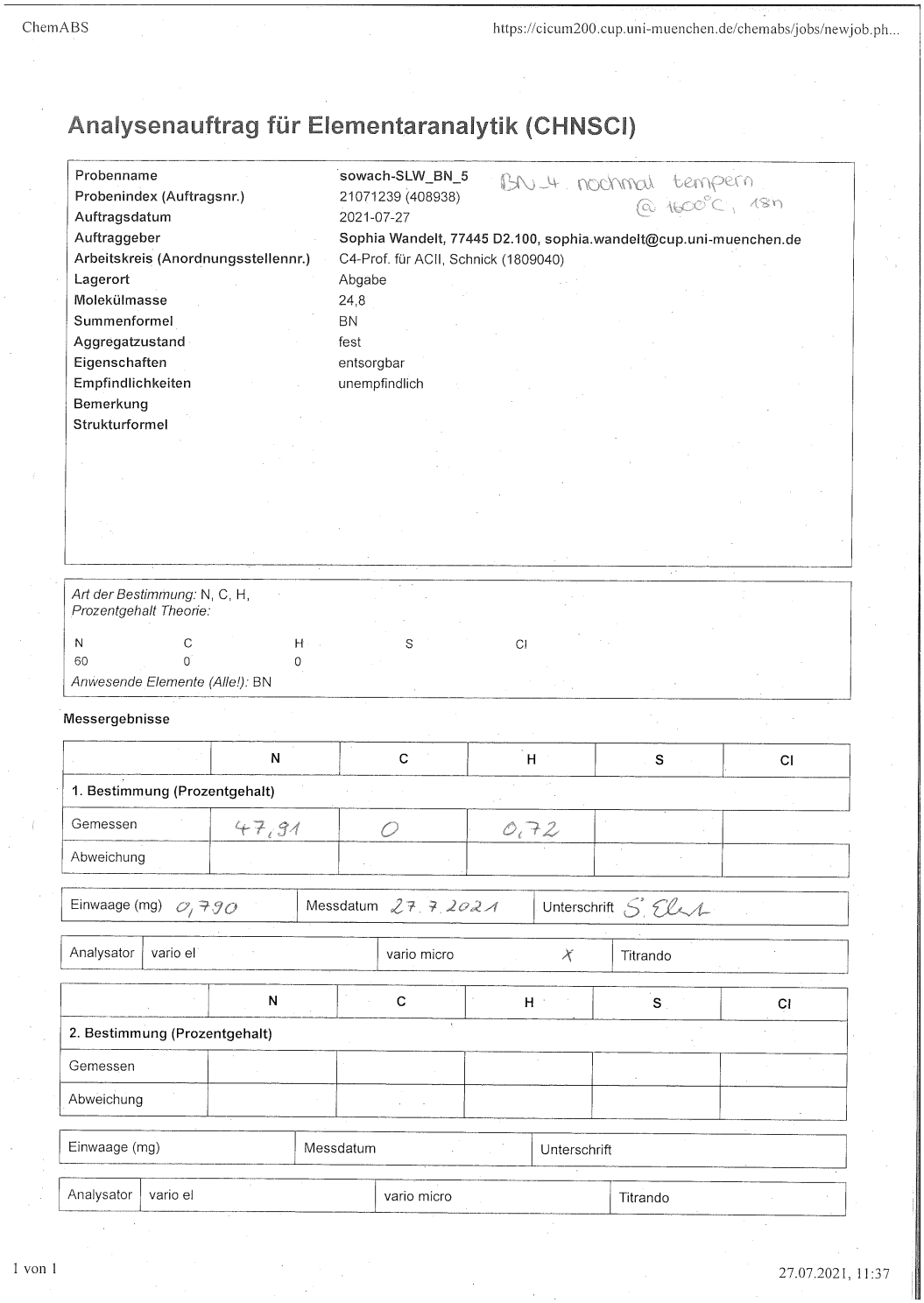

ChemABS https://cicum200.cup.uni-muenchen.de/chemabs/jobs/newjob.ph...

Analysenauftrag für Elementaranalytik (CHNSCl)

Probenname	**sowach-SLW_BN_5** BN_4 nochmal tempern @ 1600°C, 18h
Probenindex (Auftragsnr.)	21071239 (408938)
Auftragsdatum	2021-07-27
Auftraggeber	**Sophia Wandelt, 77445 D2.100, sophia.wandelt@cup.uni-muenchen.de**
Arbeitskreis (Anordnungsstellennr.)	C4-Prof. für ACII, Schnick (1809040)
Lagerort	Abgabe
Molekülmasse	24,8
Summenformel	BN
Aggregatzustand	fest
Eigenschaften	entsorgbar
Empfindlichkeiten	unempfindlich
Bemerkung	
Strukturformel	

Art der Bestimmung: N, C, H,
Prozentgehalt Theorie:

N	C	H	S	Cl
60	0	0		

Anwesende Elemente (Alle!): BN

Messergebnisse

	N	C	H	S	Cl
1. Bestimmung (Prozentgehalt)					
Gemessen	47,91	0	0,72		
Abweichung					

Einwaage (mg)	0,790	Messdatum	27.7.2021	Unterschrift	S. Elm

Analysator	vario el		vario micro	X	Titrando

	N	C	H	S	Cl
2. Bestimmung (Prozentgehalt)					
Gemessen					
Abweichung					

Einwaage (mg)	Messdatum	Unterschrift	

Analysator	vario el	vario micro		Titrando

1 von 1 27.07.2021, 11:37

Figure S2.2. Elemental analysis report of the precursor ^{11}BN, which shows a H content of 0.72 wt %.

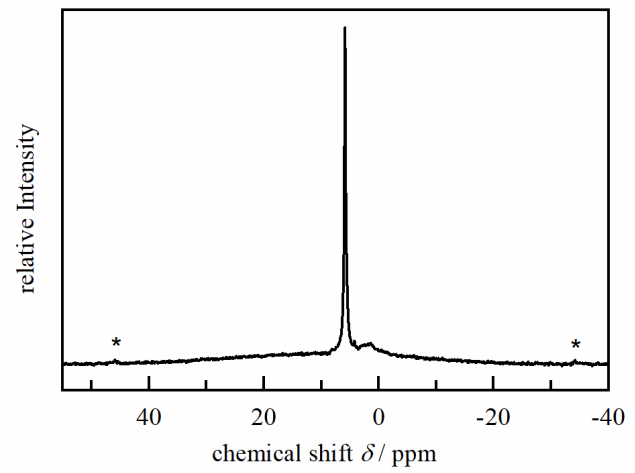

Figure S2.3. ^{1}H MAS NMR spectrum of $Sr_2{}^{11}BN_2D_{0.86}H_{0.14}$. A sharp signal at 5.8 ppm identical to Sr_2BN_2H (Figure 4 in the manuscript) confirms the presence of hydrogen in the sample. The diminished signal at 1.4 ppm arises from minor impurities.

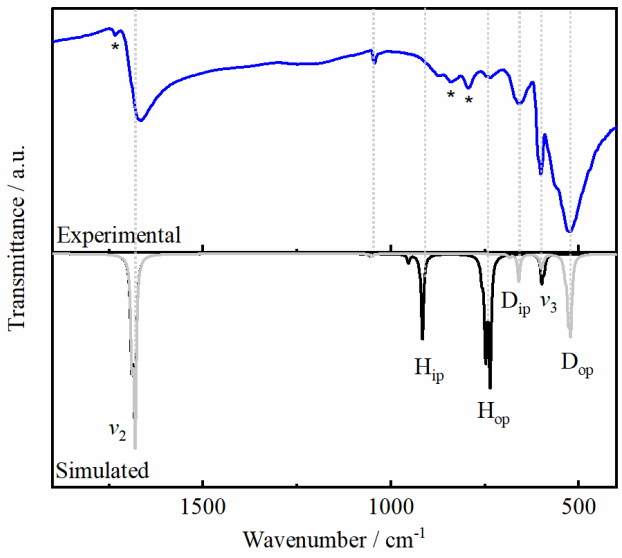

Figure S2.4. Experimental FTIR spectrum of $Sr_2{}^{11}BN_2D_{0.86}H_{0.14}$ (top, blue) and simulated FTIR spectrum (bottom) of Sr_2BN_2H (black) and Sr_2BN_2D (gray). The deuterium vibrations are shifted by the factor √2 in comparison to the hydride vibrations. Bands marked with an asterisk presumably arise from the byproduct $Sr_3B_2N_4$.

Table S2.3. Crystallographic data of Sr_2BN_2H obtained from single crystal XRD data. Standard deviations are given in parentheses.

atom	Wyckoff	*x*	*y*	*z*	*sof*
Sr1	4*c*	0.02744(2)	1/4	0.66085(3)	1
Sr2	4*c*	0.17851(3)	1/4	0.01695(3)	1
N1	4*c*	0.1452(2)	1/4	0.4321(2)	1
N2	4*c*	0.3166(3)	1/4	0.2296(2)	1
B1	4*c*	0.2271(3)	1/4	0.3262(3)	1
H1	4*c*	0.452(4)	1/4	0.601(4)	1

atom	U_{11}	U_{22}	U_{33}	U_{12}	U_{13}	U_{23}
Sr1	0.00865(11)	0.01041(12)	0.00855(12)	0.000	−0.00050(9)	0.000
Sr2	0.00790(11)	0.01042(12)	0.01373(13)	0.000	0.00109(10)	0.000
N1	0.0118(11)	0.0166(11)	0.0109(11)	0.000	−0.0011(9)	0.000
N2	0.0123(11)	0.0153(11)	0.0141(12)	0.000	0.0026(9)	0.000
B1	0.0093(12)	0.0067(12)	0.0144(15)	0.000	−0.0063(11)	0.000

Table S2.4. Crystallographic data of $Sr_2{}^{11}BN_2D_{0.86}H_{0.14}$ obtained from neutron powder diffraction data. Standard deviations are given in parentheses.

atom	Wyckoff	*x*	*y*	*z*	*sof*	U_{iso}
Sr1	4*c*	0.0282(4)	1/4	0.6654(4)	1	0.97(8)
Sr2	4*c*	0.1775(4)	1/4	0.0153(3)	1	1.29(8)
N1	4*c*	0.1446(3)	1/4	0.4317(3)	1	1.32(6)
N2	4*c*	0.3179(3)	1/4	0.2288(3)	1	1.39(8)
B1	4*c*	0.2264(4)	1/4	0.3275(5)	1	1.43(9)
D1	4*c*	0.4497(7)	1/4	0.6056(6)	0.857(8)	2.46(17)
H1	4*c*	0.4497(7)	1/4	0.6056(6)	0.143(8)	2.46(17)

Table S2.5. Bond lengths in Sr_2BN_2H obtained from single crystal XRD data. Standard deviations are given in parentheses.

atoms	bond length / Å	atoms	bond length / Å
Sr1–N1	2.603(2)	Sr1–Sr1	3.8499(4)
Sr1–N1	2.764(2)	Sr1–Sr2	3.8030(3)
Sr1–N2	2.588(2)	Sr1–Sr2	3.9042(4)
Sr2–N1	2.761(2)	Sr2–Sr2	3.9079(1)
Sr2–N2	2.561(3)	Sr1–H1	2.568(8)
Sr1–B1	3.194(2)	Sr2–H1	2.453(8)
Sr2–B1	2.909(2)	N1–B1	1.350(4)
Sr2–B1	3.182(3)	N2–B1	1.325(4)

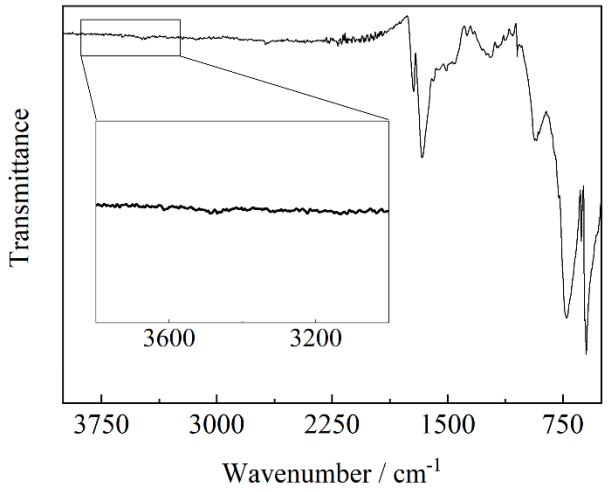

Figure S2.5. Full FTIR spectrum of Sr_2BN_2H. In the enlarged area at 3000–3800 cm^{-1} is no signal visible, which excludes the presence of N–H or O–H species.

Table S2.6. Assignment of infrared vibrations with frequency, irreducible representation and intensity obtained by quantum chemical calculations. The plane is described by the strontium atoms in the 4*c* positions (Table S2.3).

frequency/ cm^{-1}	**Γ_{irrep}**	**intensity/ $km \cdot mol^{-1}$**	**Assignment**
0	B_{2u}	0	isotropic lattice vibration
0	B_{3u}	0	isotropic lattice vibration
0	B_{1u}	0	isotropic lattice vibration
65	B_{2u}	5	isotropic lattice vibration
85	B_{1u}	2	isotropic lattice vibration
109	B_{3u}	4	isotropic lattice vibration
124	B_{2u}	12	isotropic lattice vibration
141	B_{1u}	1	isotropic lattice vibration
156	B_{2u}	1	isotropic lattice vibration
176	B_{1u}	18	isotropic lattice vibration
211	B_{1u}	1436	BN_2^{3-} in-plane vibration
230	B_{3u}	1224	BN_2^{3-} out-of-plane vibration
234	B_{2u}	1337	BN_2^{3-} in-plane vibration
265	B_{3u}	710	BN_2^{3-} out-of-plane vibration
278	B_{1u}	913	BN_2^{3-} in-plane vibration
284	B_{2u}	884	BN_2^{3-} in-plane vibration
298	B_{1u}	29	BN_2^{3-} in-plane vibration
338	B_{2u}	2	BN_2^{3-} in-plane vibration
617	B_{3u}	414	BN_2^{3-} out-of-plane bending (ν_3)
624	B_{2u}	416	BN_2^{3-} in-plane bending (ν_3)
624	B_{1u}	372	BN_2^{3-} in-plane bending (ν_3)
767	B_{3u}	3639	H^- out-of-plane vibration
779	B_{1u}	2795	H^- in-plane vibration
790	B_{2u}	534	H^- in-plane vibration
955	B_{2u}	2529	H^- in-plane vibration
993	B_{1u}	240	H^- in-plane vibration
1096	B_{2u}	1	symmetrical BN_2^{3-} stretching
1097	B_{1u}	64	symmetrical BN_2^{3-} stretching
1751	B_{1u}	5278	antisymmetrical BN_2^{3-} stretching (ν_2)
1760	B_{2u}	2679	antisymmetrical BN_2^{3-} stretching (ν_2)

Table S2.7. Assignment of Raman vibrations with frequency, irreducible representation and intensity obtained by quantum chemical calculations. The plane is described by the strontium atoms in the 4*c* positions (Table S2.3).

frequency/ cm^{-1}	**Γ_{irrep}**	**intensity/ km·mol^{-1}**	**Assignment**
45	B_{3g}	8	isotropic lattice vibration
80	B_{1g}	919	isotropic lattice vibration
81	A_g	18	isotropic lattice vibration
95	B_{2g}	38	isotropic lattice vibration
104	B_{2g}	0	isotropic lattice vibration
105	B_{1g}	12	isotropic lattice vibration
121	A_g	90	isotropic lattice vibration
124	A_g	373	isotropic lattice vibration
141	B_{3g}	108	isotropic lattice vibration
159	B_{3g}	87	isotropic lattice vibration
169	B_{3g}	15	isotropic lattice vibration
186	A_g	604	isotropic lattice vibration
219	A_g	274	BN_2^{3-} in-plane vibration
232	B_{2g}	179	BN_2^{3-} out-of-plane vibration
235	B_{1g}	56	BN_2^{3-} out-of-plane vibration
249	B_{3g}	5	BN_2^{3-} in-plane vibration
258	A_g	279	BN_2^{3-} in-plane vibration
262	B_{2g}	73	BN_2^{3-} out-of-plane vibration
263	B_{1g}	599	BN_2^{3-} out-of-plane vibration
291	B_{3g}	93	BN_2^{3-} in-plane vibration
310	A_g	538	BN_2^{3-} in-plane vibration
354	B_{3g}	117	BN_2^{3-} in-plane vibration
617	B_{1g}	66	BN_2^{3-} out-of-plane bending
618	B_{2g}	4	BN_2^{3-} out-of-plane bending
626	A_g	80	BN_2^{3-} in-plane bending
638	B_{3g}	1	BN_2^{3-} in-plane bending
848	B_{1g}	144	H^- out-of-plane vibration
848	B_{2g}	0	H^- out-of-plane vibration
872	A_g	162	H^- in-plane vibration
879	B_{3g}	39	H^- in-plane vibration
891	A_g	291	H^- in-plane vibration
898	B_{3g}	24	H^- in-plane vibration
1094	B_{3g}	156	symmetrical BN_2^{3-} stretching (ν_1)
1097	A_g	1000	symmetrical BN_2^{3-} stretching (ν_1)
1732	A_g	78	antisymmetrical BN_2^{3-} stretching
1815	B_{3g}	40	antisymmetrical BN_2^{3-} stretching

Optimized crystal structure of Sr_2BN_2H as CIF (DFT-PBE0/TZVP level of theory)

```
data_SR2BN2H
_audit_creation_method FINDSYM

_cell_length_a    9.8407725700
_cell_length_b    3.8956774300
_cell_length_c    10.2379655800
_cell_angle_alpha 90.0000000000
_cell_angle_beta  90.0000000000
_cell_angle_gamma 90.0000000000

_symmetry_space_group_name_H-M "P 21/n 21/m 21/a"
_symmetry_Int_Tables_number 62
_space_group.reference_setting '062:-P 2ac 2n'
_space_group.transform_Pp_abc a,b,c;0,0,0

loop_
_space_group_symop_id
_space_group_symop_operation_xyz
1 x,y,z
2 x+1/2,-y+1/2,-z+1/2
3 -x,y+1/2,-z
4 -x+1/2,-y,z+1/2
5 -x,-y,-z
6 -x+1/2,y+1/2,z+1/2
7 x,-y+1/2,z
8 x+1/2,y,-z+1/2

loop_
_atom_site_label
_atom_site_type_symbol
_atom_site_symmetry_multiplicity
_atom_site_Wyckoff_label
_atom_site_fract_x
_atom_site_fract_y
_atom_site_fract_z
_atom_site_occupancy
Sr1 Sr   4 c 0.52765  0.25000 0.34040  1.00000
Sr2 Sr   4 c 0.17952  0.25000 0.51792  1.00000
N1  N    4 c 0.14915  0.25000 -0.06914 1.00000
N2  N    4 c 0.31695  0.25000 0.72595  1.00000
B1  B    4 c 0.22989  0.25000 0.82422  1.00000
H1  H    4 c -0.04499 0.25000 0.39887  1.00000
```

8.3 Supporting Information for Chapter 3

Table S3.1. Crystallographic data of the Rietveld refinement of $Sr_{13}[BN_2]_6H_8$ based on powder XRD data. Standard deviations are given in parentheses.

sum formula	**$Sr_{13}[BN_2]_6H_8$**
formula weight / g·mol^{-1}	1380.10
crystal system	hexagonal
space group	$P6_3/m$ (no. 176)
lattice parameters / Å	a = 13.6922(1) c = 3.88729(4)
volume / Å^3	631.19(2)
Z	1
X-ray density / g·cm^{-3}	3.646
diffractometer	STOE Stadi P
radiation	Cu-$K\alpha_1$ (λ = 1.54059 Å)
monochromator	Ge(111)
detector	Mythen1K
2ϑ range / °	5 ≤ 2ϑ ≤ 122
data points	7839
number of reflections	386
refined parameters	53
background function	shifted Chebyshev, 18 polynomials
R indices	R_p = 5.591 R_{wp} = 7.547 R_{exp} = 6.006 R_{Bragg} = 2.959
GoF (χ^2)	1.257

Table S3.2. Elemental analysis (CHNS) results of the synthesized ^{11}BN (in wt %).

element	measured	expected
C	0	0
H	0.72	0
N	47.91	56
S	0	0

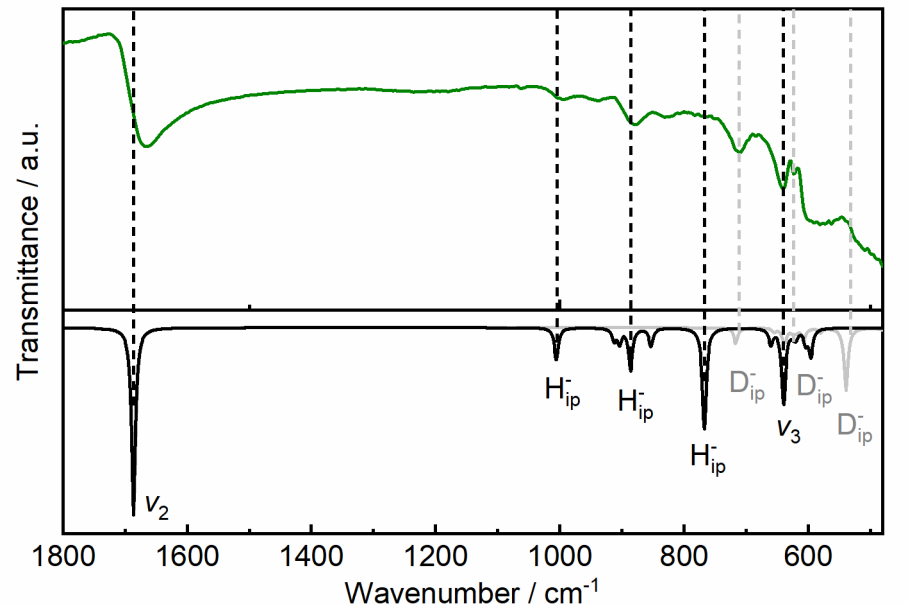

Figure S3.1. Experimental (top) FTIR spectrum of $Sr_{13}[^{11}BN_2]_6D_{6.8}H_{1.2}$ and simulated (bottom) spectra of $Sr_{13}[^{11}BN_2]_6D_8$ (gray) and $Sr_{13}[BN_2]_6H_8$ (black). The experimental spectrum shows both H and D vibrations shifted by the factor √2, indicating the presence of hydrogen in the sample.

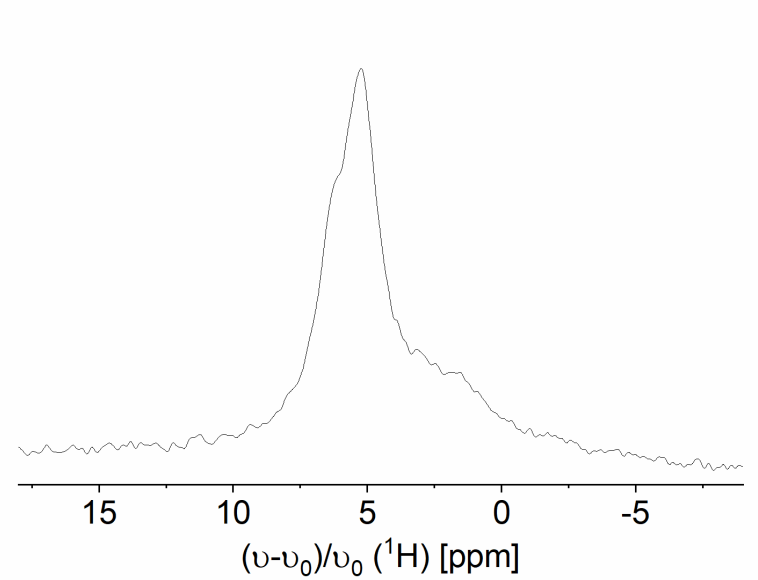

Figure S3.2. ^{1}H MAS NMR spectrum of $Sr_{13}[^{11}BN_2]_6D_{6.8}H_{1.2}$ showing the same two signals at 6.4 and 5.4 ppm as $Sr_{13}[BN_2]_6H_8$ (Figure 5 in the manuscript) and confirming the presence of hydrogen in the sample. The shoulder at around 2 ppm arises from minor impurities.

Table S3.3. Atomic positions, occupations and anisotropic displacement parameters of $Sr_{13}[BN_2]_6H_8$ based on single crystal XRD data. Standard deviations are given in parentheses.

atom	**Wyckoff**	***x***	***y***	***z***	***sof***
Sr1	6*h*	0.52082(3)	0.13085(3)	1/4	1
Sr2	6*h*	0.28494(3)	0.23947(3)	1/4	1
Sr3	2*a*	0	0	1/4	0.5
N1	6*h*	0.0823(3)	0.4542(3)	1/4	1
N2	6*h*	0.2443(3)	0.4016(3)	1/4	1
B1	6*h*	0.1725(4)	0.4404(4)	1/4	1

atom	**U_{11}**	**U_{22}**	**U_{33}**	**U_{12}**	**U_{13}**	**U_{23}**
Sr1	0.0089(2)	0.0085(2)	0.0104(2)	0.000	0.000	0.0046(1)
Sr2	0.0117(2)	0.0110(2)	0.0096(2)	0.000	0.000	0.0056(2)
Sr3	0.0101(4)	0.0101(4)	0.0162(6)	0.000	0.000	0.0051(2)
N1	0.009(2)	0.013(2)	0.016(2)	0.000	0.000	0.005(1)
N2	0.014(2)	0.013(2)	0.016(2)	0.000	0.000	0.008(1)
B1	0.012(2)	0.005(2)	0.006(2)	0.000	0.000	0.001(2)

Table S3.4. Atomic positions, occupations and isotropic displacement parameters of $Sr_{13}[^{11}BN_2]_6D_{6.8}H_{1.2}$ from refinement based on neutron powder diffraction data. Standard deviations are given in parentheses.

atom	Wyckoff	*x*	*y*	*z*	*sof*	U_{iso}
Sr1	6*h*	0.52072	0.13187	1/4	1	0.0195(11)
Sr2	6*h*	0.28377	0.23675	1/4	1	0.0080(12)
Sr3	2*a*	0	0	1/4	0.5	0.030(4)
N1	6*h*	0.08242	0.45367	1/4	1	0.0189(9)
N2	6*h*	0.24427	0.39968	1/4	1	0.0149(8)
B1	6*h*	0.17221	0.43937	1/4	1	0.0154(10)
D1	2*d*	2/3	1/3	1/4	0.831(10)	0.066(6)
H1	2*d*	2/3	1/3	1/4	0.169(10)	0.066(6)
D2	6*h*	0.17273	0.02253	1/4	0.855(8)	0.080(4)
H2	6*h*	0.17273	0.02253	1/4	0.145(8)	0.080(4)

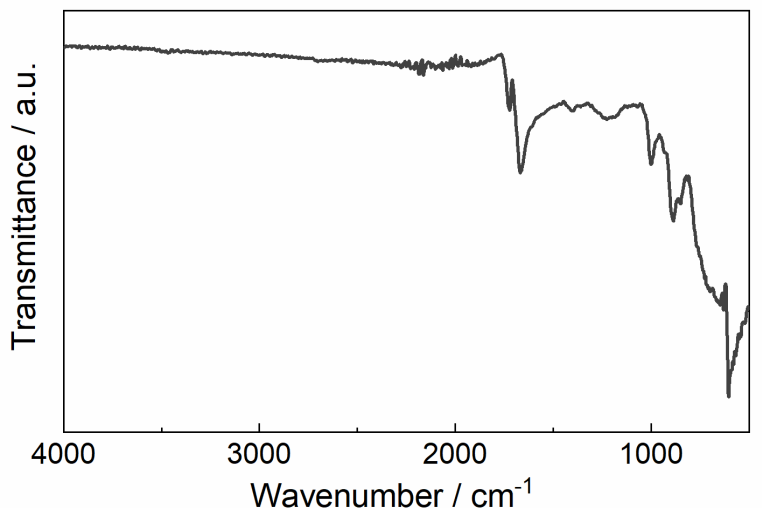

Figure S3.3. Full FTIR spectrum of $Sr_{13}[BN_2]_6H_8$, where in the region of 3600–3200 cm^{-1} no signal is visible, excluding any NH^- or OH^- species. The spectrum was recorded with a diamond attenuated total reflectance (ATR) unit.

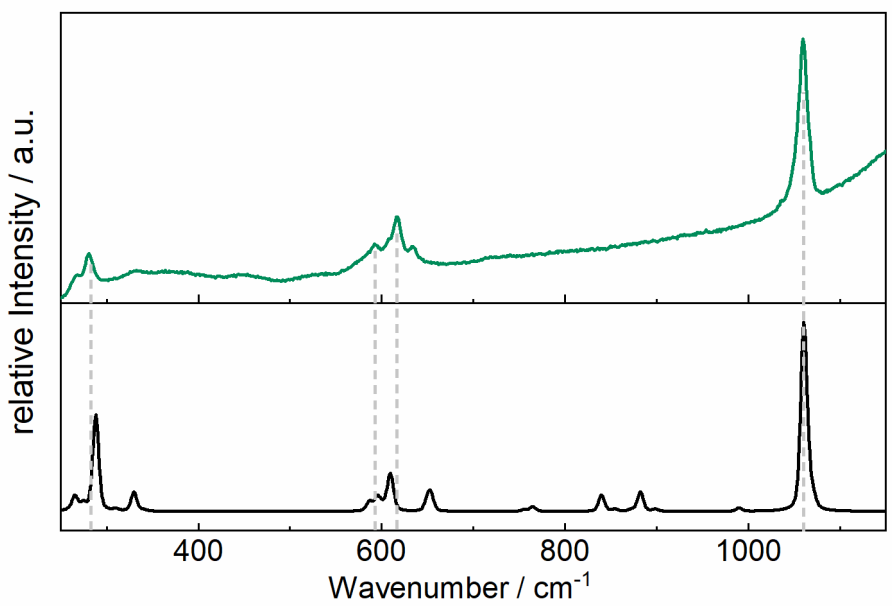

Figure S3.4. Experimental (top) and simulated (bottom) Raman spectrum of $Sr_{13}[BN_2]_6H_8$.

Table S3.5. Assignment of infrared vibrations with frequency, irreducible representation and intensity obtained by quantum chemical calculations. The plane is described by the strontium atoms.

frequency/ cm^{-1}	**Γ_{irrep}**	**intensity/ km·mol^{-1}**	**assignment**
73	A	2	isotropic lattice vibrations
78	E	2	isotropic lattice vibrations
80	E	9	isotropic lattice vibrations
94	A	2	isotropic lattice vibrations
106	A	3	isotropic lattice vibrations
113	A	3	isotropic lattice vibrations
124	E	7	isotropic lattice vibrations
125	E	20	isotropic lattice vibrations
143	E	14	isotropic lattice vibrations
156	E	5	isotropic lattice vibrations
168	E	14	isotropic lattice vibrations
181	E	170	isotropic lattice vibrations
200	A	98	$[BN_2]^{3-}$ out-of-plane vibration
219	A	537	$[BN_2]^{3-}$ out-of-plane vibration
227	A	1773	$[BN_2]^{3-}$ out-of-plane vibration

frequency/ cm^{-1}	**Γ_{irrep}**	**intensity/ $km \cdot mol^{-1}$**	**assignment**
229	E	3653	$[BN_2]^{3-}$ in-plane vibration
242	A	790	$[BN_2]^{3-}$ out-of-plane vibration
281	E	1226	$[BN_2]^{3-}$ in-plane vibration
290	E	851	$[BN_2]^{3-}$ in-plane vibration
305	E	185	$[BN_2]^{3-}$ in-plane vibration
328	E	790	$[BN_2]^{3-}$ in-plane vibration
385	A	779	H^- out-of-plane vibration
399	A	750	H^- out-of-plane vibration
621	E	1614	$[BN_2]^{3-}$ in-plane bending (ν_3)
629	E	786	$[BN_2]^{3-}$ in-plane bending (ν_3)
632	A	3	H^- in-plane vibration
644	A	7	$[BN_2]^{3-}$ in-plane bending (ν_3)
645	A	463	$[BN_2]^{3-}$ out-of-plane bending (ν_3)
650	A	278	$[BN_2]^{3-}$ out-of-plane bending (ν_3)
666	E	4485	H^- out-of-plane vibration
688	E	934	H^- in-plane vibration
692	E	9	H^- out-of-plane vibration
799	E	6008	H^- in-plane vibration
889	E	1085	H^- in-plane vibration
923	E	2490	H^- in-plane vibration
941	A	855	H^- out-of-plane vibration
951	E	704	H^- in-plane vibration
1047	E	1903	H^- in-plane vibration
1123	E	25	symmetrical $[BN_2]^{3-}$ stretching
1757	E	11193	antisymmetrical $[BN_2]^{3-}$ stretching (ν_2)
1808	E	20	antisymmetrical $[BN_2]^{3-}$ stretching (ν_2)

Table S3.6. Assignment of Raman vibrations with frequency, irreducible representation and intensity obtained by quantum chemical calculations. The plane is described by the strontium atoms.

frequency/ cm^{-1}	**Γ_{irrep}**	**intensity/ $km \cdot mol^{-1}$**	**assignment**
46	E	16	isotropic lattice vibrations
63	A	21	isotropic lattice vibrations
78	E	4	isotropic lattice vibrations
80	E	4	isotropic lattice vibrations
82	E	547	isotropic lattice vibrations
87	A	71	isotropic lattice vibrations
103	E	99	isotropic lattice vibrations
112	E	24	isotropic lattice vibrations
115	A	84	isotropic lattice vibrations
120	A	10	isotropic lattice vibrations
124	E	90	isotropic lattice vibrations
125	E	30	isotropic lattice vibrations
130	A	65	isotropic lattice vibrations
136	A	80	isotropic lattice vibrations
143	E	6	isotropic lattice vibrations
156	E	308	isotropic lattice vibrations
168	E	30	isotropic lattice vibrations
172	A	120	isotropic lattice vibrations
181	E	6	isotropic lattice vibrations
193	E	61	$[BN_2]^{3-}$ out-of-plane vibration
212	E	273	$[BN_2]^{3-}$ out-of-plane vibration
216	A	8	$[BN_2]^{3-}$ in-plane vibration
220	A	68	$[BN_2]^{3-}$ in-plane vibration
233	E	15	$[BN_2]^{3-}$ out-of-plane vibration
245	E	57	$[BN_2]^{3-}$ in-plane vibration
246	E	17	$[BN_2]^{3-}$ out-of-plane vibration
272	A	6	$[BN_2]^{3-}$ in-plane vibration
281	E	98	$[BN_2]^{3-}$ in-plane vibration

frequency/ cm^{-1}	**Γ_{irrep}**	**intensity/ $km \cdot mol^{-1}$**	**assignment**
290	E	48	$[BN_2]^{3-}$ in-plane vibration
305	E	646	$[BN_2]^{3-}$ in-plane vibration
328	E	13	$[BN_2]^{3-}$ in-plane vibration
349	A	126	$[BN_2]^{3-}$ in-plane vibration
361	A	8	$[BN_2]^{3-}$ in-plane vibration
621	E	63	H^- in-plane vibration
629	E	68	$[BN_2]^{3-}$ in-plane bending (v_3)
632	A	35	H^- in-plane vibration
638	A	30	H^- in-plane vibration
644	E	18	$[BN_2]^{3-}$ out-of-plane bending (v_3)
645	A	215	H^- in-plane vibration
649	E	24	$[BN_2]^{3-}$ out-of-plane bending (v_3)
688	E	68	H^- in-plane vibration
692	E	102	H^- out-of-plane vibration
799	E	11	H^- in-plane vibration
809	A	31	H^- in-plane vibration
889	E	109	H^- in-plane vibration
904	A	13	H^- in-plane vibration
923	E	11	H^- in-plane vibration
934	E	130	H^- out-of-plane vibration
951	E	14	H^- in-plane vibration
1047	E	21	H^- in-plane vibration
1122	A	1000	symmetrical $[BN_2]^{3-}$ stretching
1123	E	41	symmetrical $[BN_2]^{3-}$ stretching
1125	A	291	H^- in-plane vibration
1126	E	66	symmetrical $[BN_2]^{3-}$ stretching
1133	A	83	H^- in-plane vibration

Computational details

The geometry, electronic and vibrational properties of $Sr_{13}[BN_2]_6H_8$ were studied by density functional theory calculations at the DFT-PBE0 level of theory.[1,2] Calculations were conducted by the CRYSTAL17 program package.[3] Gaussian type basis sets, split valence polarized for Sr and triple zeta polarized for all other elements, were used. The respective basis sets have been derived from the molecular Karlsruhe def2 basis sets and prior works.[4–6] As the Sr3 position of the experimentally determined structure is disordered, an ordered model as input geometry was set. To avoid creating a large supercell with high computational costs, an ordered model with lower symmetry was chosen as substituting structure. The symmetry was lowered from $P6_3/m$ (no. 176) to $P3$ (no. 143) to introduce an ordered Sr3 position, herein denoted as Sr5. The new ordered position represents an averaged position of the symmetrically split, half occupied original Sr3 position. The reciprocal space was sampled using 3x3x8 Monkhorst-Pack-type k-meshes.[7] Tightened tolerance (TOLINTEG) of 8, 8, 8, 8 and 16 were used for the evaluation of Coulomb and exchange integrals. The atomic positions and lattice parameters were fully optimized within the constraints of the space group symmetry. The optimized lattice parameters *a* and *c* of the ordered model differed to the experimentally determined values by −0.05% and −0.2% respectively. Band paths within the reciprocal space for the determination of the electronic band structures were obtained by the Seek-path webservice.[8,9] Harmonic frequencies and corresponding Raman and IR intensities were simulated using the computational schemes implemented in the CRYSTAL17 program package.[10–12] The ordered model did not exhibit imaginary frequencies, confirming this model as a local energetic minimum. Raman intensities were calculated for polycrystalline powder samples with a Raman laser wavelength of λ = 532 nm and an experimental temperature of T = 298.15 K. The final IR and Raman spectra were simulated using a Lorentzian profile for the IR spectrum, a pseudo-Voigt profile (50:50 – Lorentzian:Gaussian) for the Raman spectrum and a FWHM of 8 cm^{-1} for both simulations.

Optimized crystal structure of the ordered model of $Sr_{13}[BN_2]_6H_8$ as CIF (DFT-PBE0/TZVP level of theory)

```
data_Sr13B6N12H8
_audit_creation_method FINDSYM

_cell_length_a    13.6662252000
_cell_length_b    13.6662252000
_cell_length_c    3.8764995000
_cell_angle_alpha 90.0000000000
_cell_angle_beta  90.0000000000
_cell_angle_gamma 120.0000000000
_symmetry_space_group_name_H-M "P 3"
_symmetry_Int_Tables_number 143
_space_group.reference_setting '143:P 3'
_space_group.transform_Pp_abc a,b,c;0,0,0

loop_
_space_group_symop_id
_space_group_symop_operation_xyz
1 x,y,z
2 -y,x-y,z
3 -x+y,-x,z

loop_
_atom_site_label
_atom_site_type_symbol
_atom_site_symmetry_multiplicity
_atom_site_Wyckoff_label
_atom_site_fract_x
_atom_site_fract_y
_atom_site_fract_z
_atom_site_occupancy
Sr1 Sr   3 d 0.47959  0.86956  0.74933 1.00000
Sr2 Sr   3 d 0.52044  0.13031  0.24967 1.00000
Sr3 Sr   3 d 0.04588  0.28799  0.74422 1.00000
Sr4 Sr   3 d -0.04627 0.71162  0.25288 1.00000
Sr5 Sr   1 a 0.00000  0.00000  0.01475 1.00000
N1  N    3 d 0.62881  0.08231  0.75036 1.00000
N2  N    3 d 0.37151  -0.08264 0.24799 1.00000
N3  N    3 d 0.84281  0.24537  0.74915 1.00000
N4  N    3 d 0.15702  0.75532  0.24867 1.00000
B1  B    3 d 0.73224  0.17355  0.75049 1.00000
B2  B    3 d 0.26777  0.82666  0.24747 1.00000
H1  H    1 b 0.33333  0.66667  0.74974 1.00000
H2  H    1 c 0.66667  0.33333  0.24887 1.00000
H3  H    3 d 0.14545  0.16922  0.74139 1.00000
H4  H    3 d 0.85058  0.82543  0.24600 1.00000
```

References

[1] J. P. Perdew, K. Burke, M. Ernzerhof, *Phys. Rev. Lett.* **1996**, *77*, 3865–3868.

[2] C. Adamo, V. Barone, *J. Chem. Phys.* **1999**, *110*, 6158–6170.

[3] R. Dovesi, A. Erba, R. Orlando, C. M. Zicovich-Wilson, B. Civalleri, L. Maschio, M. Rérat, S. Casassa, J. Baima, S. Salustro, B. Kirtman, *Wiley Interdiscip. Rev.: Comput. Mol. Sci.* **2018**, *8*, e1360.

[4] T. Wylezich, R. Valois, M. Suta, A. Mutschke, C. Ritter, A. Meijerink, A. J. Karttunen, N. Kunkel, *Chem. Eur. J.* **2020**, *26*, 11742–11750.

[5] F. Weigend, R. Ahlrichs, *Phys. Chem. Chem. Phys.* **2005**, *7*, 3297–3305.

[6] A. J. Karttunen, T. Tynell, M. Karppinen, *J. Phys. Chem. C* **2015**, *119*, 13105–13114.

[7] H. J. Monkhorst, J. D. Pack, *Phys. Rev. B* **1976**, *13*, 5188–5192.

[8] A. Togo, I. Tanaka, **2018**, arXiv:1808.01590.

[9] Y. Hinuma, G. Pizzi, Y. Kumagai, F. Oba, I. Tanaka, *Comput. Mater. Sci.* **2017**, *128*, 140–184.

[10] F. Pascale, C. M. Zicovich-Wilson, F. L. Gejo, B. Civalleri, R. Orlando, R. Dovesi, *J. Comput. Chem*. **2004**, *25*, 888–897.

[11] C. M. Zicovich-Wilson, F. Pascale, C. Roetti, V. R. Saunders, R. Orlando, R. Dovesi, *J. Comput. Chem*. **2004**, *25*, 1873–1881.

[12] L. Maschio, B. Kirtman, M. Rérat, R. Orlando, R. Dovesi, *J. Chem. Phys.* **2013**, *139*, 164101.

8.4 Supporting Information for Chapter 4

Structure Determination

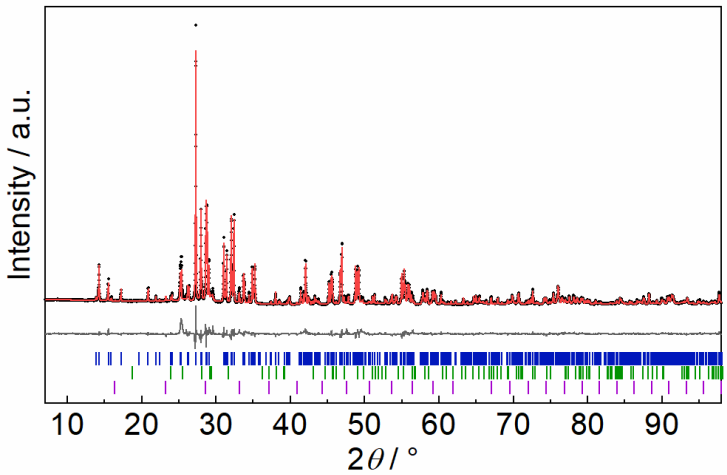

Figure S4.1. Rietveld refinement of $Sr_6N[BN_2]_2H_3$ based on powder XRD data. The black, red and gray lines show the experimental and calculated data and their difference, respectively. The Bragg markers denote from top to bottom: $Sr_6N[BN_2]_2H_3$ (92.5(2) wt %), SrH_2 (5.5(2) wt %) and $Sr_3B_2N_4$ (2.1(1) wt %).

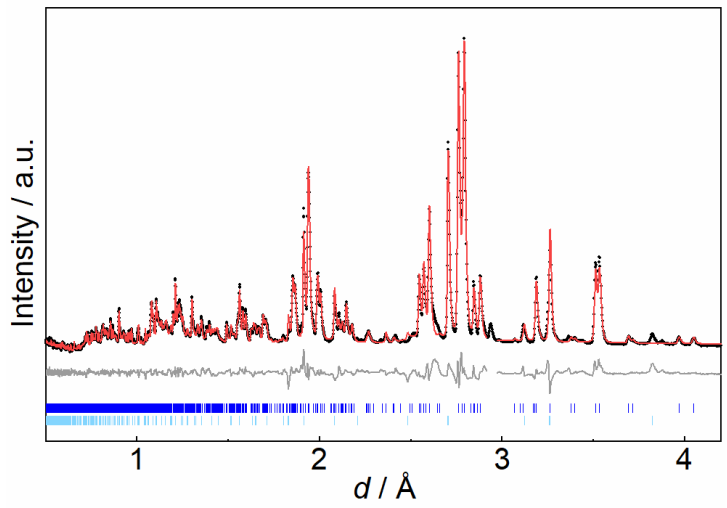

Figure S4.2. Rietveld refinement of $Sr_6N[^{11}BN_2]_2D_3$ based on time-of-flight neutron powder diffraction data collected at the high-resolution backscattering detector bank with the average $2\vartheta = 153°$. The red, black and gray lines show the calculated and experimental data and their difference, respectively. The Bragg markers indicate $Sr_6N[^{11}BN_2]_2D_3$ (top, 82.2(2) wt %) and Sr_2ND (bottom, 17.7(2) wt %).

Table S4.1. Atomic coordinates, isotropic thermal displacement parameters, Wyckoff position and site occupancy of $Sr_6N[BN_2]_2H_3$ obtained from single-crystal X-ray refinement data. Standard deviations are given in parentheses.

atom	*x*	*y*	*z*	U_{eq}	Wyck.	*occ.*
Sr1	0.28127(7)	0.06531(4)	0.30834(6)	0.01053(13)	4*e*	1
Sr2	0.26273(7)	0.44068(4)	0.32158(6)	0.01040(13)	4*e*	1
Sr3	0.17014(7)	0.79177(4)	0.04460(6)	0.01386(14)	4*e*	1
N1	0	0	0	0.0118(12)	2*a*	1
N2	0.5377(6)	0.1359(3)	0.1245(6)	0.0146(9)	4*e*	1
N3	0.5232(6)	0.3700(3)	0.1390(5)	0.0135(9)	4*e*	1
B1	0.5110(9)	0.2537(5)	0.1256(7)	0.0115(11)	4*e*	1

Table S4.2. Atomic coordinates, isotropic thermal displacement parameters, Wyckoff position and site occupancy of $Sr_6N[^{11}BN_2]_2D_3$ obtained from powder neutron diffraction data. Standard deviations are given in parentheses.

atom	*x*	*y*	*z*	U_{eq}	Wyck.	*occ.*
Sr1	0.2752(18)	0.0618(9)	0.304(1)	0.02(4)	4*e*	1
Sr2	0.2677(17)	0.4410(7)	0.3100(13)	0.02(3)	4*e*	1
Sr3	0.1556(10)	0.7899(5)	0.0395(9)	0.010(3)	4*e*	1
N1	0	0	0	0.015(3)	2*a*	1
N2	0.5353(13)	0.1388(7)	0.1203(11)	0.023(3)	4*e*	1
N3	0.5269(14)	0.3705(8)	0.1439(13)	0.028(3)	4*e*	1
B1	0.5072(13)	0.2521(15)	0.1242(11)	0.027(2)	4*e*	1
D1	0.0666(13)	0.2458(11)	0.2686(10)	0.036(3)	4*e*	1
D2	0.073(6)	0.521(4)	0.021(6)	0.177(17)	4*e*	0.5

Vibrational Spectroscopy

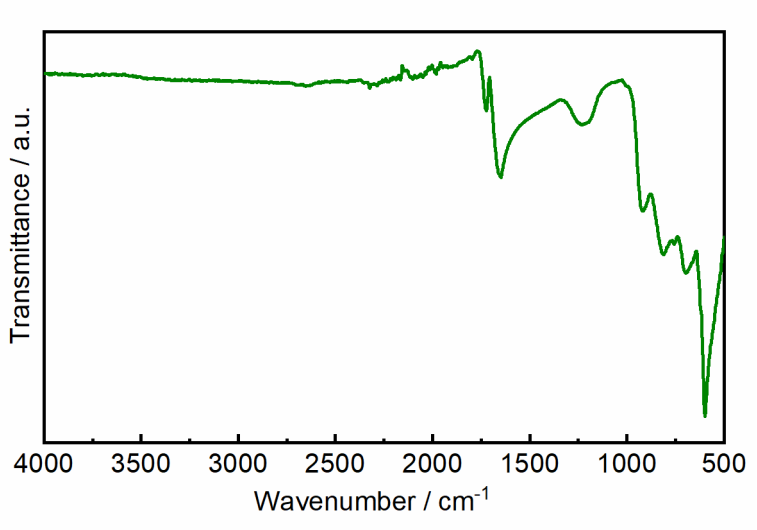

Figure S4.3. FTIR spectrum of $Sr_6N[BN_2]_2H_3$. No bands are in the region of 3600–3200 cm^{-1} visible, which excludes any NH or OH species.

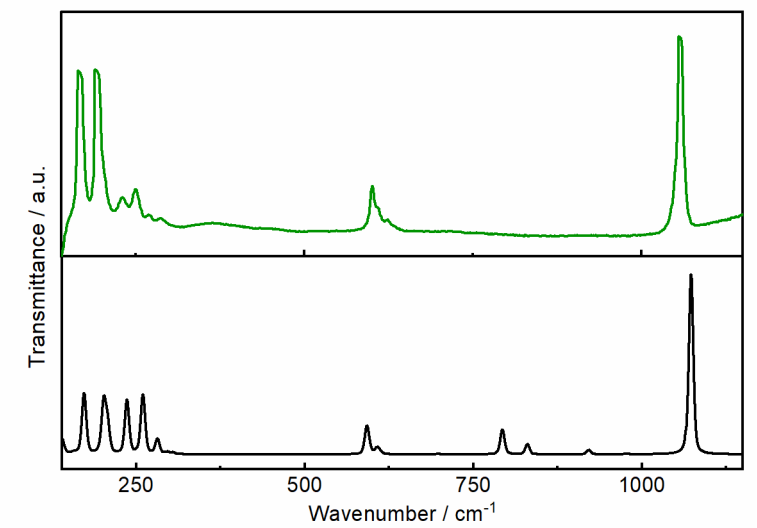

Figure S4.4. Experimental (top) and simulated (bottom) Raman spectrum of $Sr_6N[BN_2]_2H_3$. In the region of 800–900 cm^{-1}, the expected hydride in-plane and out-of-plane vibrations appear rather broad and unresolved compared to the simulated spectrum.

Table S4.3. Assignment of Infrared vibrations of $Sr_6N[BN_2]_2H_3$ with frequency, irreducible representation and intensity obtained by quantum chemical calculations. The plane is described by the different layers of $[BN_2]^{3-}$ units or hydride and nitride anions, respectively.

frequency/ cm^{-1}	Γ_{irrep}	intensity/ $km \cdot mol^{-1}$	assignment
0	B_u	0	isotropic lattice vibration
0	A_u	0	isotropic lattice vibration
0	B_u	0	isotropic lattice vibration
26	A_u	30	isotropic lattice vibration
94	A_u	560	isotropic lattice vibration
102	B_u	4	isotropic lattice vibration
115	A_u	91	isotropic lattice vibration
124	A_u	68	isotropic lattice vibration
136	B_u	52	isotropic lattice vibration
140	A_u	1	isotropic lattice vibration
148	B_u	32	isotropic lattice vibration
155	B_u	57	isotropic lattice vibration
167	A_u	6	isotropic lattice vibration
179	B_u	46	isotropic lattice vibration
184	A_u	2	isotropic lattice vibration
207	B_u	611	$[BN_2]^{3-}$ out-of-plane vibration
209	A_u	82	$[BN_2]^{3-}$ in-plane vibration
217	A_u	223	$[BN_2]^{3-}$ in-plane vibration
240	B_u	1959	$[BN_2]^{3-}$ in-plane vibration
250	B_u	2546	$[BN_2]^{3-}$ out-of-plane vibration
259	A_u	88	$[BN_2]^{3-}$ out-of-plane vibration
264	A_u	1170	$[BN_2]^{3-}$ in-plane vibration
265	B_u	598	$[BN_2]^{3-}$ in-plane vibration
274	B_u	640	H^- out-of-plane vibration N^{3-} out-of-plane vibration
275	A_u	30	$[BN_2]^{3-}$ in-plane vibration
336	A_u	2789	H^- in-plane vibration N^{3-} in-plane vibration
340	B_u	687	H^- in-plane vibration N^{3-} in-plane vibration
356	A_u	1795	H^- in-plane vibration N^{3-} in-plane vibration
366	B_u	368	H^- in-plane vibration N^{3-} in-plane vibration $[BN_2]^{3-}$ in-plane vibration

frequency/ cm^{-1}	**Γ_{irrep}**	**intensity/ $km \cdot mol^{-1}$**	**assignment**
376	A_u	740	H^- in-plane vibration N^{3-} in-plane vibration
382	B_u	98	H^- out-of-plane vibration N^{3-} out-of-plane vibration $[BN_2]^{3-}$ out-of-plane vibration
392	A_u	109	H^- in-plane vibration N^{3-} out-of-plane vibration
523	B_u	63	H^- out-of-plane vibration
617	B_u	1543	H^- out-of-plane vibration $[BN_2]^{3-}$ out-of-plane bending (ν_3)
623	A_u	1	$[BN_2]^{3-}$ out-of-plane bending (ν_3)
631	B_u	2055	H^- out-of-plane vibration $[BN_2]^{3-}$ out-of-plane bending (ν_3)
638	B_u	555	H1 in-plane vibration H2 out-of-plane vibration $[BN_2]^{3-}$ in-plane bending (ν_3)
639	A_u	7	$[BN_2]^{3-}$ in-plane bending (ν_3)
661	A_u	185	H1 in-plane vibration H2 out-of-plane vibration
743	B_u	1350	H1 in-plane vibration H2 out-of-plane vibration
812	A_u	347	H^- out-of-plane vibration
833	A_u	14	H^- out-of-plane vibration
844	B_u	154	H^- out-of-plane vibration
868	A_u	9	H1 in-plane vibration H2 out-of-plane vibration
872	B_u	4567	H^- out-of-plane vibration
964	B_u	2137	H^- in-plane vibration
989	A_u	1980	H^- in-plane vibration
1119	B_u	1	symmetrical $[BN_2]^{3-}$ stretching
1738	B_u	158	antisymmetrical $[BN_2]^{3-}$ stretching (ν_2)
1745	A_u	8448	antisymmetrical $[BN_2]^{3-}$ stretching (ν_2)

Table S4.4. Assignment of Raman vibrations of $Sr_6N[BN_2]_2H_3$ with frequency, irreducible representation and intensity obtained by quantum chemical calculations. The plane is described by the different layers of $[BN_2]^{3-}$ units or hydride and nitride anions, respectively.

frequency/ cm^{-1}	Γ_{irrep}	intensity/ $km \cdot mol^{-1}$	assignment
78	A_g	164	isotropic lattice vibration
93	B_g	7	isotropic lattice vibration
100	A_g	390	isotropic lattice vibration
101	B_g	69	isotropic lattice vibration
107	A_g	204	isotropic lattice vibration
108	B_g	17	isotropic lattice vibration
110	A_g	309	isotropic lattice vibration
121	A_g	27	isotropic lattice vibration
125	B_g	4	isotropic lattice vibration
137	A_g	47	isotropic lattice vibration
147	B_g	85	isotropic lattice vibration
149	A_g	4	isotropic lattice vibration
166	B_g	8	isotropic lattice vibration
181	A_g	346	isotropic lattice vibration
204	B_g	16	isotropic lattice vibration
211	A_g	35	isotropic lattice vibration
212	A_g	232	isotropic lattice vibration
215	B_g	162	$[BN_2]^{3-}$ out-of-plane vibration
243	B_g	265	$[BN_2]^{3-}$ out-of-plane vibration
244	A_g	39	$[BN_2]^{3-}$ in-plane vibration
269	A_g	22	$[BN_2]^{3-}$ out-of-plane vibration
271	B_g	264	$[BN_2]^{3-}$ out-of-plane vibration
293	B_g	92	$[BN_2]^{3-}$ in-plane vibration
308	B_g	11	$[BN_2]^{3-}$ in-plane vibration
315	A_g	8	$[BN_2]^{3-}$ in-plane vibration
624	B_g	16	$[BN_2]^{3-}$ out-of-plane bending (ν_3)
634	A_g	39	$[BN_2]^{3-}$ in-plane bending (ν_3)
640	B_g	13	$[BN_2]^{3-}$ in-plane bending (ν_3)
727	A_g	3	H^- in-plane vibration
826	B_g	138	H^- in-plane vibration
836	B_g	3	H^- out-of-plane vibration
865	A_g	57	H^- out-of-plane vibration
960	A_g	26	H^- in-plane vibration
1017	B_g	5	H^- in-plane vibration
1114	B_g	13	symmetrical $[BN_2]^{3-}$ stretching
1117	A_g	1000	symmetrical $[BN_2]^{3-}$ stretching

Conductivity Measurements

To determine the partial ionic and electronic conductivity of $Sr_6N[BN_2]_2H_3$, electrochemical impedance spectroscopy (EIS) measurements were performed on a cold-pressed pellet. The pressed pellet has a relative pellet density of 77.7%. The electrochemical impedance measurement (Figure S4.5) shows an imperfect semicircle. The absence of a polarization tail suggests that the sample is a mixed ionic and electronic conductor. To account for both the ionic and electronic conduction processes, the spectra were fitted using an equivalent circuit comprising a resistor and a constant phase element in series (ionic conduction), which are parallel connected to both a resistor (electronic conduction) and another constant phase element (geometrical capacitance). The CPE of the ionic conduction process has an effective capacitance (according to the Brug formulas) of C_{Brug}=2.4×10^{-11} F, which is often assigned to grain boundary processes.[80] The low alpha value of 0.56, suggests that possibly two different processes overlap, however it was not possible to fit these processes separately. The CPE of the geometrical capacitance has an effective capacitance of C_{Brug}=7.6×10^{-11} F. Figure S4.6 depicts temperature-dependent plots of the ionic and electronic conductivity, which show clear Arrhenius behavior. The activation energies of the ionic and electronic conduction are determined to be 0.437 eV and 0.522 eV, respectively.

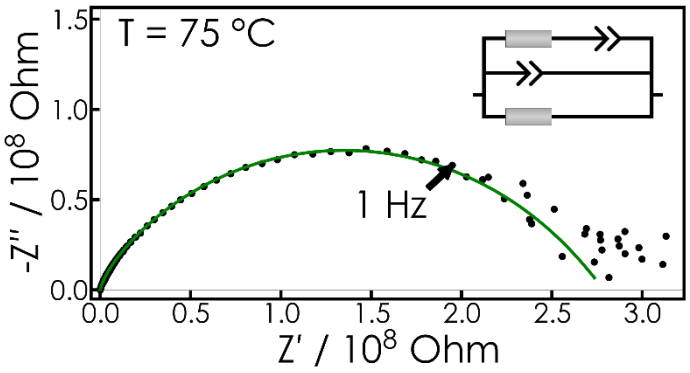

Figure S4.5. Electrochemical impedance measurement of a cold-pressed pellet of $Sr_6N[BN_2]_2H_3$. The data was only fitted between 1 MHz and 1 Hz due to noise at low frequencies. However, to show the behavior at low frequencies, the measured data points down to 0.01 Hz were included in the plot.

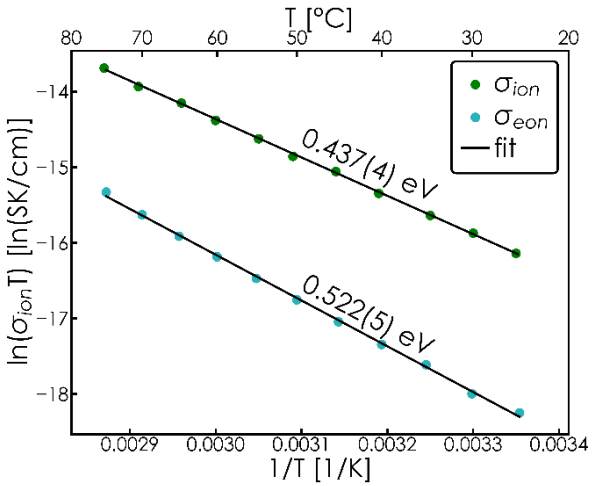

Figure S4.6. Ionic and electronic activation energies of a cold-pressed pellet of $Sr_6N[BN_2]_2H_3$ determined by electrochemical impedance spectroscopy.

The electric conductivities of the sample were assessed by conducting a chronopotentiometry (a direct current polarization technique) measurement (Figure S4.7). After an initial phase without applied current, a current of 5 nA was introduced, resulting in a voltage increase. The electronic conductivity can be calculated from the saturation point (U_e) of the voltage using Ohm's law and the pellet dimensions (cf. Eq. 1). The measurement yields an electronic conductivity of σ_{eon}=5.8×10^{-10} S/cm at 75 °C. This is in good agreement with the electronic conductivity obtained from EIS (σ_{eon}=6.3×10^{-10} S/cm). From the so-called IR drop, the total electric conductivity can be determined according to Equation 2. By averaging the two IR drops, the resultant total electric conductivity is calculated as σ_{total}=7.5×10^{-10} S/cm.

$$\sigma_{eon} = \frac{1}{R_{eon}} \frac{d}{A} \; with \; R_{eon} = \frac{U_e}{I} \qquad \text{(Eq. 1)}$$

$$\sigma_{total} = \frac{1}{R_{IR}} \frac{d}{A} \; with \; R_{IR} = \frac{U_{IR}}{I} \qquad \text{(Eq. 2)}$$

The ionic conduction is then derived by subtracting the electronic conductivity from the total, resulting in a value of σ_{ion}=1.7×10^{-10} S/cm.

$$\sigma_{ion} = \sigma_{total} - \sigma_{eon} \qquad \text{(Eq. 3)}$$

Notably, this value is one order of magnitude lower than that obtained via EIS. This discrepancy is likely attributed to the fact that the measured conductivities approach the lower limit of our measurement capabilities. Consequently, errors introduced by the measuring equipment exert a pronounced influence on the results.

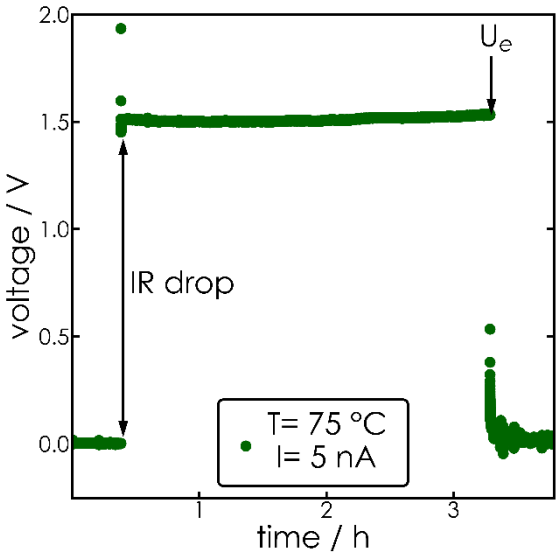

Figure S4.7. Chronopotentiometry measurement of $Sr_6N[BN_2]_2H_3$ at 75 °C and 5 nA. From the saturation point of the voltage, the electronic resistance can be calculated using Ohm's law.

The activation energies of both Sr^{2+} and H^- migration were estimated using the software package softBV and the structure of $Sr_6N[BN_2]_2H_3$ determined in this work (Figure S4.8 and S4.9). SoftBV, tailored for optimizing the prediction of activation energies in Li-ion conduction, is employed to reinforce the conclusions drawn from X-ray and neutron diffraction data. While Sr^{2+} migration leads to extremely high predicted activation energies of around 3.9 eV even for one-dimensional ion conduction, simulation of H^- migration yields more reasonable activation energies for a two-dimensional ion conduction process of 0.60 eV. This is in good agreement with the measured activation energy from temperature-dependent impedance spectroscopy of 0.437(3) eV. The difference can most likely be explained by the simplicity of the softBV simulation, which is more simplistic (e.g. lattice dynamics are not taken into account) and hence faster, but less accurate than DFT. As there is not sufficient data reported for hydride ions, the accuracy of this calculations is not as high as for other prominent ions such as lithium or oxide ions. However, the trend that the activation barrier for hydrides is significantly smaller than the one for strontium further supports our thesis that hydrides are the conducting species in our compound.

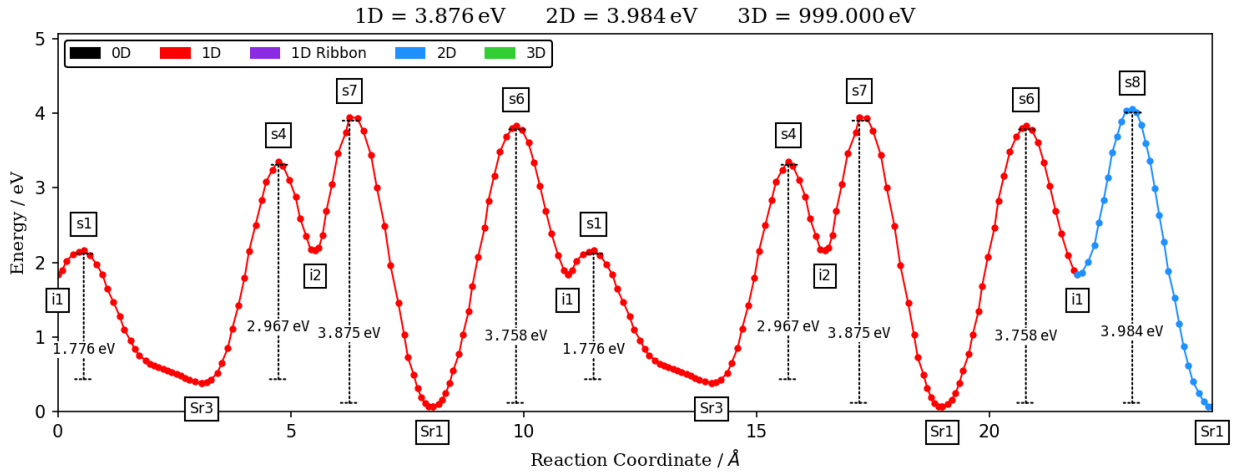

Figure S4.8. Calculation of the energy barrier for the migration of Sr^{2+} atoms in $Sr_6N[BN_2]_2H_3$ using the softBV program.

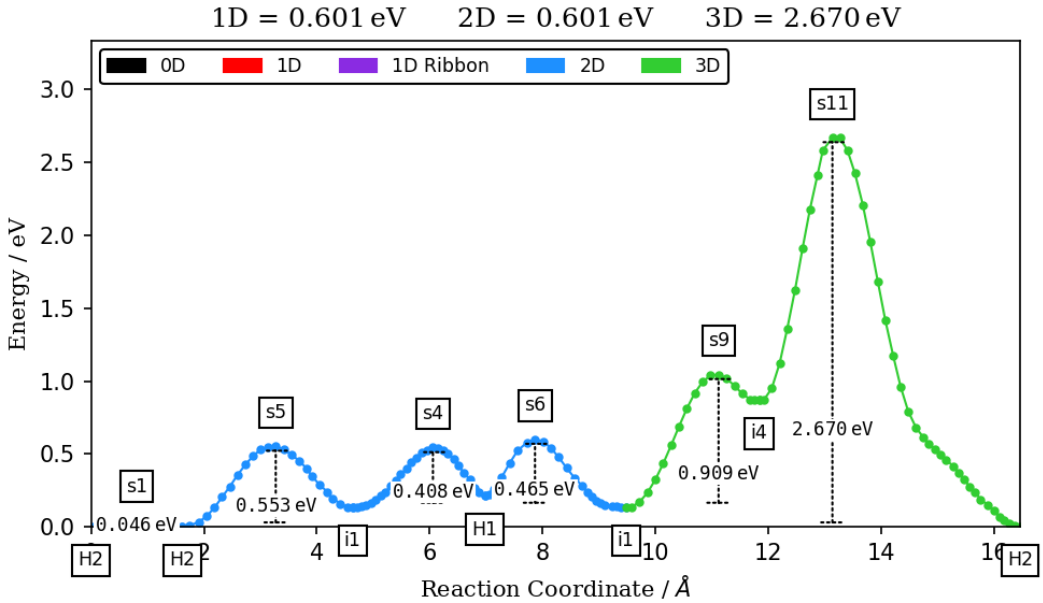

Figure S4.9. Calculation of the energy barrier for the migration of H^- atoms in $Sr_6N[BN_2]_2H_3$ using the softBV program.

From the parameters obtained from the impedance measurements between 25 and 75 °C, the ionic conductivity at 300 °C can be estimated. The activation energy and prefactor of the ionic conductivity were determined by applying the Arrhenius equation to the measured ionic conductivities. Using those parameters, the ionic conductivity at 300 °C was estimated to be around $\sigma_{300°C}=5.8\times10^{-7}$ S/cm.

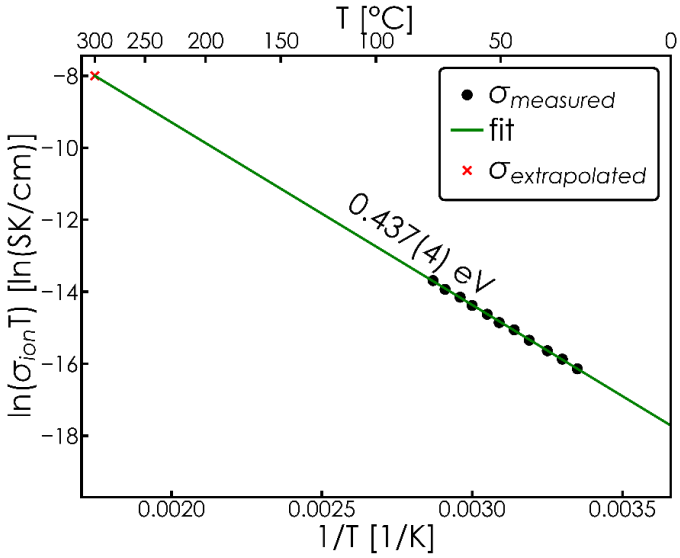

Figure S4.10. Arrhenius plot of the ionic conductivities at different temperatures as well as the resulting activation energy. Using the Arrhenius equation, the ionic conductivity value for 300 °C was estimated.

Quantum Chemical Calculations

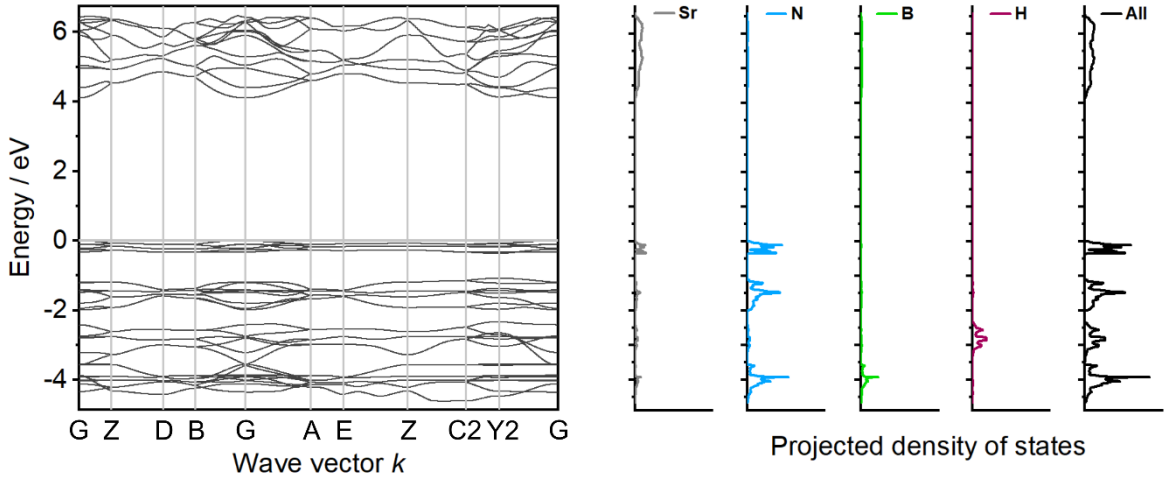

Figure S4.11. Electronic band structure and projected density of states of $Sr_6N[BN_2]_2H_3$ calculated at the DFT-PBE0/TZVP level of theory.

Optimized crystal structure of the ordered model of $Sr_6N[BN_2]_2H_3$ as CIF (DFT-PBE0/TZVP level of theory)

```
data_Sr6B2N5H3 small cell
_audit_creation_method FINDSYM

_cell_length_a    13.2734723541
_cell_length_b    11.3871000000
_cell_length_c    7.7311000000
_cell_angle_alpha 90.0000000000
_cell_angle_beta  106.2940977310
_cell_angle_gamma 90.0000000000

_symmetry_space_group_name_H-M "P 1 21/c 1"
_symmetry_Int_Tables_number 14
_space_group.reference_setting '014:-P 2ybc'
_space_group.transform_Pp_abc a,b,c;0,0,0

loop_
_space_group_symop_id
_space_group_symop_operation_xyz
1 x,y,z
2 -x,y+1/2,-z+1/2
3 -x,-y,-z
4 x,-y+1/2,z+1/2

loop_
_atom_site_label
_atom_site_type_symbol
_atom_site_symmetry_multiplicity
_atom_site_Wyckoff_label
_atom_site_fract_x
_atom_site_fract_y
_atom_site_fract_z
_atom_site_occupancy
Sr1 Sr   4 e 0.89064  -0.06531 0.08231  1.00000
Sr2 Sr   4 e 0.39064  -0.06531 0.58231  1.00000
Sr3 Sr   4 e 0.88137  0.55932  0.05979  1.00000
Sr4 Sr   4 e 0.38137  0.55932  0.55979  1.00000
Sr5 Sr   4 e 0.83507  0.29177  0.79046  1.00000
Sr6 Sr   4 e 0.33507  0.29177  0.29046  1.00000
N1  N    4 e 0.75000  0.50000  0.75000  1.00000
N2  N    4 e -0.01885 0.36400  0.10565  1.00000
N3  N    4 e 0.48115  0.36400  0.60565  1.00000
```

```
N4  N    4 e -0.01160 0.13000  0.12740  1.00000
N5  N    4 e 0.48840  0.13000  0.62740  1.00000
B1  B    4 e -0.00550 0.24630  0.12000  1.00000
B2  B    4 e 0.49450  0.24630  0.62000  1.00000
H1  H    4 e 0.71750  0.25000  0.47950  1.00000
H2  H    4 e 0.21750  0.25000  -0.02050 1.00000
H3  H    4 e 0.74500  0.52100  0.26900  1.00000


data_Sr6B2N5H3 large cell
_audit_creation_method FINDSYM

_cell_length_a    13.1786851500
_cell_length_b    11.3871642200
_cell_length_c    7.6810711900
_cell_angle_alpha 90.0000000000
_cell_angle_beta  106.2592850000
_cell_angle_gamma 90.0000000000

_symmetry_space_group_name_H-M "P 1 21/c 1"
_symmetry_Int_Tables_number 14
_space_group.reference_setting '014:-P 2ybc'
_space_group.transform_Pp_abc a,b,c;0,0,0

loop_
_space_group_symop_id
_space_group_symop_operation_xyz
1 x,y,z
2 -x,y+1/2,-z+1/2
3 -x,-y,-z
4 x,-y+1/2,z+1/2

loop_
_atom_site_label
_atom_site_type_symbol
_atom_site_symmetry_multiplicity
_atom_site_Wyckoff_label
_atom_site_fract_x
_atom_site_fract_y
_atom_site_fract_z
_atom_site_occupancy
Sr1 Sr   4 e 0.89035  0.43540 0.58252  1.00000
Sr2 Sr   4 e 0.39034  0.43544 0.08252  1.00000
Sr3 Sr   4 e 0.88150  0.05946 0.55866  1.00000
```

```
Sr4 Sr   4 e 0.38148  0.05944 0.05866  1.00000
Sr5 Sr   4 e 0.83587  0.79593 0.29104  1.00000
Sr6 Sr   4 e 0.33590  0.79590 0.79106  1.00000
N1  N    4 e 0.75000  0.00001 0.25001  1.00000
N2  N    4 e -0.01869 0.86345 0.60628  1.00000
N3  N    4 e 0.48132  0.86346 0.10630  1.00000
N4  N    4 e -0.01206 0.63070 0.62745  1.00000
N5  N    4 e 0.48798  0.63071 0.12746  1.00000
B1  B    4 e -0.00604 0.74711 0.62015  1.00000
B2  B    4 e 0.49400  0.74713 0.12016  1.00000
H1  H    4 e 0.71915  0.74997 -0.01584 1.00000
H2  H    4 e 0.21919  0.75000 0.48412  1.00000
H3  H    4 e 0.75000  0.00004 0.75001  1.00000
```

Mulliken Population analysis of $Sr_6N[BN_2]_2H_3$ (DFT-PBE0/TZVP level of theory)

ALPHA+BETA ELECTRONS

MULLIKEN POPULATION ANALYSIS - NO. OF ELECTRONS 216.000000

ATOM Z CHARGE A.O. POPULATION

```
1 SR 238  8.816  0.743  1.209  0.238  0.128  0.115  0.143  1.934  1.934
          1.939  0.008  0.008  0.005  0.005  0.006  0.098  0.099
          0.065  0.063  0.076
2 SR 238  8.816  0.743  1.209  0.238  0.128  0.115  0.143  1.934  1.934
          1.939  0.008  0.008  0.005  0.005  0.006  0.098  0.099
          0.065  0.063  0.076
3 SR 238  8.816  0.743  1.209  0.238  0.128  0.115  0.143  1.934  1.934
          1.939  0.008  0.008  0.005  0.005  0.006  0.098  0.099
          0.065  0.063  0.076
4 SR 238  8.816  0.743  1.209  0.238  0.128  0.115  0.143  1.934  1.934
          1.939  0.008  0.008  0.005  0.005  0.006  0.098  0.099
          0.065  0.063  0.076
5 SR 238  8.819  0.743  1.208  0.238  0.141  0.117  0.129  1.937  1.933
          1.933  0.006  0.009  0.004  0.006  0.007  0.080  0.104
          0.054  0.080  0.089
6 SR 238  8.819  0.743  1.208  0.238  0.141  0.117  0.129  1.937  1.933
          1.933  0.006  0.009  0.004  0.006  0.007  0.080  0.104
          0.054  0.080  0.089
7 SR 238  8.819  0.743  1.208  0.238  0.141  0.117  0.129  1.937  1.933
          1.933  0.006  0.009  0.004  0.006  0.007  0.080  0.104
          0.054  0.080  0.089
8 SR 238  8.819  0.743  1.208  0.238  0.141  0.117  0.129  1.937  1.933
          1.933  0.006  0.009  0.004  0.006  0.007  0.080  0.104
```

0.054 0.080 0.089
9 SR 238 8.808 0.742 1.208 0.228 0.110 0.142 0.109 1.934 1.934
1.934 0.007 0.007 0.006 0.008 0.008 0.075 0.087
0.086 0.086 0.097
10 SR 238 8.808 0.742 1.208 0.228 0.110 0.142 0.109 1.934 1.934
1.934 0.007 0.007 0.006 0.008 0.008 0.075 0.087
0.086 0.086 0.097
11 SR 238 8.808 0.742 1.208 0.228 0.110 0.142 0.109 1.934 1.934
1.934 0.007 0.007 0.006 0.008 0.008 0.075 0.087
0.086 0.086 0.097
12 SR 238 8.808 0.742 1.208 0.228 0.110 0.142 0.109 1.934 1.934
1.934 0.007 0.007 0.006 0.008 0.008 0.075 0.087
0.086 0.086 0.097
13 N 7 8.234 0.818 1.159 0.789 1.078 0.758 0.743 0.755 0.270
0.268 0.264 0.447 0.445 0.438 0.000 0.000 0.000
0.000 0.000
14 N 7 8.234 0.818 1.159 0.789 1.078 0.758 0.743 0.755 0.270
0.268 0.264 0.447 0.445 0.438 0.000 0.000 0.000
0.000 0.000
15 N 7 7.945 0.818 1.158 0.793 0.941 0.685 0.538 0.700 0.276
0.297 0.273 0.475 0.516 0.465 0.001 0.000 0.003
0.003 0.003
16 N 7 7.945 0.818 1.158 0.793 0.941 0.685 0.538 0.700 0.276
0.297 0.273 0.475 0.516 0.465 0.001 0.000 0.003
0.003 0.003
17 N 7 7.945 0.818 1.158 0.793 0.941 0.685 0.538 0.700 0.276
0.297 0.273 0.475 0.516 0.465 0.001 0.000 0.003
0.003 0.003
18 N 7 7.945 0.818 1.158 0.793 0.941 0.685 0.538 0.700 0.276
0.297 0.273 0.475 0.516 0.465 0.001 0.000 0.003
0.003 0.003
19 N 7 7.932 0.818 1.158 0.796 0.932 0.694 0.542 0.683 0.272
0.299 0.274 0.462 0.518 0.474 0.001 0.000 0.003
0.003 0.003
20 N 7 7.932 0.818 1.158 0.796 0.932 0.694 0.542 0.683 0.272
0.299 0.274 0.462 0.518 0.474 0.001 0.000 0.003
0.003 0.003
21 N 7 7.932 0.818 1.158 0.796 0.932 0.694 0.542 0.683 0.272
0.299 0.274 0.462 0.518 0.474 0.001 0.000 0.003
0.003 0.003
22 N 7 7.932 0.818 1.158 0.796 0.932 0.694 0.542 0.683 0.272
0.299 0.274 0.462 0.518 0.474 0.001 0.000 0.003
0.003 0.003
23 B 5 4.954 0.916 1.045 0.215 0.710 0.449 0.155 0.451 0.029
0.067 0.029 0.182 0.391 0.184 0.007 0.001 0.052
0.020 0.051

24 B 5 4.954 0.916 1.045 0.215 0.710 0.449 0.155 0.451 0.029
0.067 0.029 0.182 0.391 0.184 0.007 0.001 0.052
0.020 0.051
25 B 5 4.954 0.916 1.045 0.215 0.710 0.449 0.155 0.451 0.029
0.067 0.029 0.182 0.391 0.184 0.007 0.001 0.052
0.020 0.051
26 B 5 4.954 0.916 1.045 0.215 0.710 0.449 0.155 0.451 0.029
0.067 0.029 0.182 0.391 0.184 0.007 0.001 0.052
0.020 0.051
27 H 1 1.729 0.145 0.464 1.118 0.001 0.001 0.001
28 H 1 1.729 0.145 0.464 1.118 0.001 0.001 0.001
29 H 1 1.729 0.145 0.464 1.118 0.001 0.001 0.001
30 H 1 1.729 0.145 0.464 1.118 0.001 0.001 0.001
31 H 1 1.761 0.138 0.410 1.212 0.000 0.000 0.000
32 H 1 1.761 0.138 0.410 1.212 0.000 0.000 0.000

ATOM Z CHARGE SHELL POPULATION

1 SR 238 8.816 0.743 1.209 0.624 5.807 0.032 0.402
2 SR 238 8.816 0.743 1.209 0.624 5.807 0.032 0.402
3 SR 238 8.816 0.743 1.209 0.624 5.807 0.032 0.402
4 SR 238 8.816 0.743 1.209 0.624 5.807 0.032 0.402
5 SR 238 8.819 0.743 1.208 0.625 5.804 0.033 0.406
6 SR 238 8.819 0.743 1.208 0.625 5.804 0.033 0.406
7 SR 238 8.819 0.743 1.208 0.625 5.804 0.033 0.406
8 SR 238 8.819 0.743 1.208 0.625 5.804 0.033 0.406
9 SR 238 8.808 0.742 1.208 0.589 5.802 0.036 0.430
10 SR 238 8.808 0.742 1.208 0.589 5.802 0.036 0.430
11 SR 238 8.808 0.742 1.208 0.589 5.802 0.036 0.430
12 SR 238 8.808 0.742 1.208 0.589 5.802 0.036 0.430
13 N 7 8.234 0.818 1.159 0.789 3.334 0.803 1.330 0.001
14 N 7 8.234 0.818 1.159 0.789 3.334 0.803 1.330 0.001
15 N 7 7.945 0.818 1.158 0.793 2.865 0.845 1.456 0.010
16 N 7 7.945 0.818 1.158 0.793 2.865 0.845 1.456 0.010
17 N 7 7.945 0.818 1.158 0.793 2.865 0.845 1.456 0.010
18 N 7 7.945 0.818 1.158 0.793 2.865 0.845 1.456 0.010
19 N 7 7.932 0.818 1.158 0.796 2.850 0.845 1.454 0.010
20 N 7 7.932 0.818 1.158 0.796 2.850 0.845 1.454 0.010
21 N 7 7.932 0.818 1.158 0.796 2.850 0.845 1.454 0.010
22 N 7 7.932 0.818 1.158 0.796 2.850 0.845 1.454 0.010
23 B 5 4.954 0.916 1.045 0.215 1.764 0.125 0.757 0.131
24 B 5 4.954 0.916 1.045 0.215 1.764 0.125 0.757 0.131
25 B 5 4.954 0.916 1.045 0.215 1.764 0.125 0.757 0.131
26 B 5 4.954 0.916 1.045 0.215 1.764 0.125 0.757 0.131
27 H 1 1.729 0.145 0.464 1.118 0.002
28 H 1 1.729 0.145 0.464 1.118 0.002

29 H 1 1.729 0.145 0.464 1.118 0.002
30 H 1 1.729 0.145 0.464 1.118 0.002
31 H 1 1.761 0.138 0.410 1.212 0.001
32 H 1 1.761 0.138 0.410 1.212 0.001

OVERLAP POPULATION CONDENSED TO ATOMS FOR FIRST 6 NEIGHBORS

ATOM A	1 SR	ATOM B	CELL	R(AB)/AU	R(AB)/ANG	OVPOP(AB)
	29 H	(-1 0 0)	4.774	2.526	0.015	
	19 N	(0 -1 0)	4.805	2.543	0.076	
	14 N	(-1 -1 0)	4.984	2.637	0.118	
	16 N	(0 0 0)	4.992	2.642	0.067	
	21 N	(0 0 1)	5.065	2.680	0.061	
	32 H	(-1 -1 0)	5.305	2.807	0.020	

ATOM A	5 SR	ATOM B	CELL	R(AB)/AU	R(AB)/ANG	OVPOP(AB)
	29 H	(-1 0 0)	4.752	2.515	0.014	
	15 N	(0 0 0)	4.846	2.564	0.072	
	13 N	(-1 0 0)	4.918	2.602	0.121	
	17 N	(0 0 1)	4.978	2.634	0.062	
	31 H	(-1 0 0)	5.014	2.653	0.019	
	20 N	(0 0 0)	5.037	2.665	0.059	

ATOM A	9 SR	ATOM B	CELL	R(AB)/AU	R(AB)/ANG	OVPOP(AB)
	30 H	(-1 0 -1)	4.673	2.473	0.021	
	27 H	(0 0 0)	4.694	2.484	0.021	
	13 N	(-1 0 -1)	4.850	2.567	0.141	
	15 N	(0 0 -1)	5.184	2.743	0.049	
	22 N	(0 0 0)	5.245	2.776	0.045	
	26 B	(0 0 0)	5.286	2.797	0.013	

ATOM A	13 N	ATOM B	CELL	R(AB)/AU	R(AB)/ANG	OVPOP(AB)
	9 SR	(1 0 1)	4.850	2.567	0.141	
	5 SR	(1 0 0)	4.918	2.602	0.121	
	2 SR	(0 0 0)	4.984	2.637	0.118	
	28 H	(1 0 1)	6.521	3.451	-0.003	
	27 H	(1 0 1)	6.539	3.460	-0.003	
	15 N	(0 0 0)	7.073	3.743	-0.002	

ATOM A	15 N	ATOM B	CELL	R(AB)/AU	R(AB)/ANG	OVPOP(AB)
	23 B	(0 0 0)	2.524	1.336	0.564	
	5 SR	(0 0 0)	4.846	2.564	0.072	
	7 SR	(0 0 1)	4.978	2.634	0.062	
	2 SR	(0 0 0)	4.992	2.642	0.067	
	19 N	(0 0 0)	5.018	2.655	-0.067	
	9 SR	(0 0 1)	5.184	2.743	0.049	

ATOM A	19 N	ATOM B	CELL	R(AB)/AU	R(AB)/ANG	OVPOP(AB)
	23 B	(0 0 0)	2.513	1.330	0.594	
	1 SR	(0 1 0)	4.805	2.543	0.076	
	15 N	(0 0 0)	5.018	2.655	-0.067	
	6 SR	(0 0 0)	5.037	2.665	0.059	
	3 SR	(0 0 1)	5.065	2.680	0.061	
	12 SR	(0 0 0)	5.245	2.776	0.045	

ATOM A	23 B	ATOM B	CELL	R(AB)/AU	R(AB)/ANG	OVPOP(AB)
	19 N	(0 0 0)	2.513	1.330	0.594	
	15 N	(0 0 0)	2.524	1.336	0.564	
	12 SR	(0 0 0)	5.286	2.797	0.013	
	9 SR	(0 0 1)	5.379	2.846	0.013	
	2 SR	(0 0 0)	6.026	3.189	0.009	
	3 SR	(0 0 1)	6.084	3.220	0.010	

ATOM A	27 H	ATOM B	CELL	R(AB)/AU	R(AB)/ANG	OVPOP(AB)
	12 SR	(0 0 0)	4.673	2.473	0.021	
	9 SR	(0 0 0)	4.694	2.484	0.021	
	7 SR	(-1 0 0)	4.752	2.515	0.014	
	3 SR	(-1 0 0)	4.774	2.526	0.015	
	23 B	(-1 0 -1)	6.445	3.411	0.002	
	31 H	(-1 0 0)	6.520	3.450	-0.001	

ATOM A	31 H	ATOM B	CELL	R(AB)/AU	R(AB)/ANG	OVPOP(AB)
	5 SR	(1 0 0)	5.014	2.653	0.019	
	2 SR	(0 0 0)	5.305	2.807	0.020	
	27 H	(1 0 0)	6.520	3.450	-0.001	
	28 H	(1 0 0)	6.540	3.461	-0.001	
	10 SR	(0 0 0)	6.683	3.536	0.010	
	20 N	(1 0 0)	6.858	3.629	-0.002	

8.5 Supporting Information for Chapter 5

Structure Determination

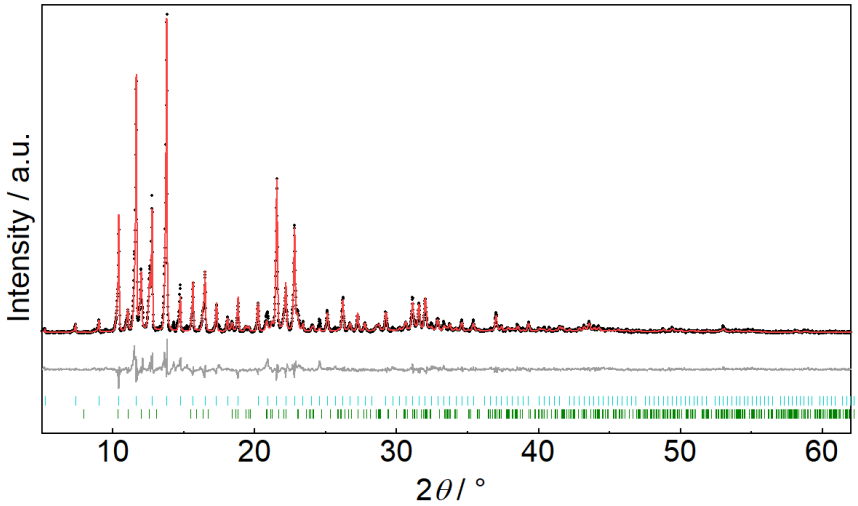

Figure S5.1. Rietveld refinement of $Ba_{12}[BN_2]_{6.67}H_4$ based on powder XRD data. The black, red and gray lines show the experimental and calculated data and their difference, respectively. The Bragg markers denote $Ba_{12}[BN_2]_{6.67}H_4$ (85.9(2) wt %, top) and BaH_2 (14.1(2) wt %, bottom).

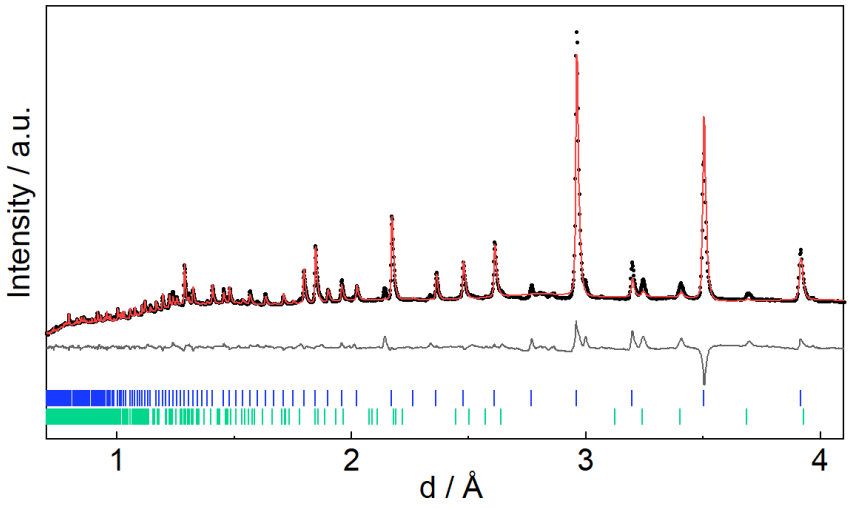

Figure S5.2. Rietveld refinement of $Ba_{12}[^{11}BN_2]_{6.67}H_4$ based on time-of-flight neutron powder diffraction data collected at the high-resolution backscattering detector bank with the average $2\vartheta = 153°$. The red, black and gray lines show the calculated and experimental data and their difference, respectively. The Bragg markers indicate $Ba_{12}[^{11}BN_2]_{6.67}H_4$ (98.6(3) wt %, top) and BaH_2 (1.42(4) wt %, bottom).

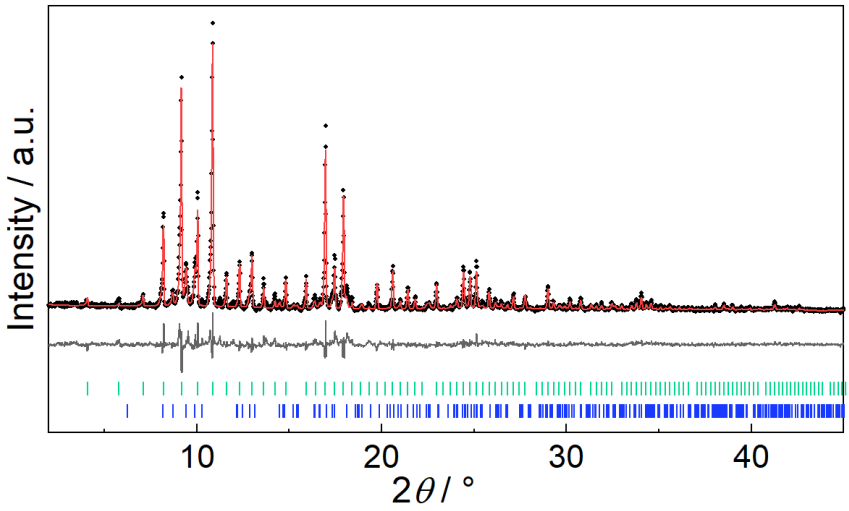

Figure S5.3. Rietveld refinement of $Ba_{12}[BN_2]_{6.67}H_4$ based on powder XRD data measured at −100 °C. The black, red and gray lines show the experimental and calculated data and their difference, respectively. The Bragg markers denote $Ba_{12}[BN_2]_{6.67}H_4$ (87.2(3) wt %, top) and BaH_2 (12.8(4) wt %, bottom).

Table S5.1. Atomic coordinates, isotropic thermal displacement parameters, Wyckoff position and site occupancy of $Ba_{12}[BN_2]_{6.67}H_4$ obtained from single-crystal X-ray refinement data. Standard deviations are given in parentheses.

atom	***x***	***y***	***z***	U_{eq} / Å²	**Wyck.**	***occ.***
Ba1	0.18033(5)	0	0.30270(5)	0.0236(2)	24*g*	1
B1	½	0	0.1503(1)	0.031(3)	12*e*	1
N1	0.3803(8)	0	0.1608(8)	0.040(2)	24*g*	1
B2	0	0	0	0.016	2*a*	0.667
N2	0	0.050(5)	0.107(3)	0.016	24*g*	0.111

Table S5.2. Atomic coordinates, isotropic thermal displacement parameters, Wyckoff position and site occupancy of $Ba_{12}[^{11}BN_2]_{6.67}H_4$ obtained from powder neutron diffraction data. Standard deviations are given in parentheses.

Atom	***x***	***y***	***z***	U_{eq} **/ Å²**	**Wyck.**	***occ.***
Ba1	0.1788(4)	0	0.3028(4)	0.0035(13)	24*g*	1
B1	½	0	0.1496(4)	0.022(2)	12*e*	1
N1	0.3865(3)	0	0.1595(3)	0.03800	24*g*	1
B2	0	0	0	0.01267	2*a*	0.667
N2	0	0.05300	0.10500	0.01267	24*g*	0.111
H1	1/4	1/4	1/4	0.016(4)	8*c*	1

Vibrational Spectroscopy

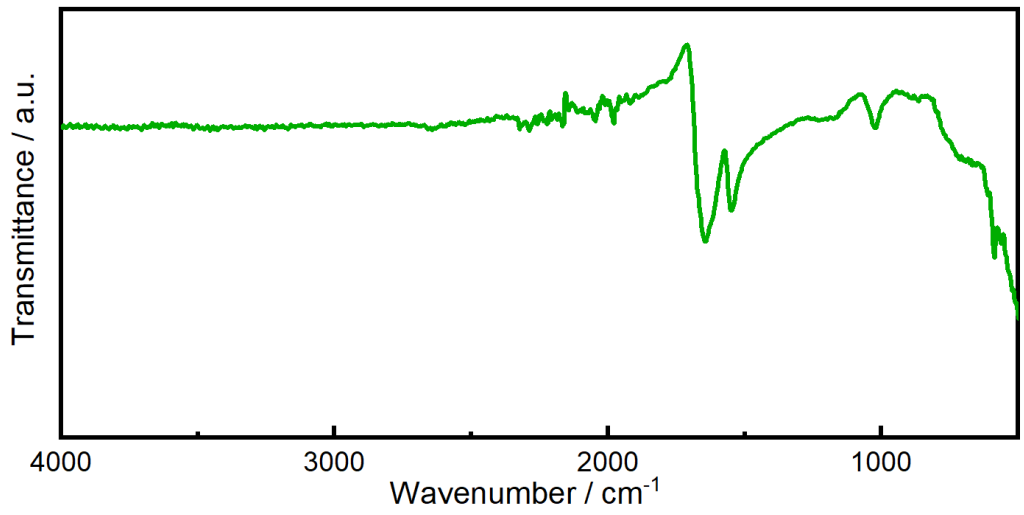

Figure S5.4. Full FTIR spectrum of $Ba_{12}[BN_2]_{6.67}H_4$. No bands are in the region of 3600–3200 cm^{-1} visible, which excludes any NH^- or OH^- species.

Table S5.3. Assignment of Infrared vibrations of $Ba_{12}[BN_2]_{6.67}H_4$ with frequency, irreducible representation and intensity obtained by quantum chemical calculations.

frequency/ cm^{-1}	Γ_{irrep}	intensity/ $km \cdot mol^{-1}$	assignment
54	E_u	27	various lattice vibrations
62	E_u	287	various lattice vibrations
68	E_u	59	various lattice vibrations
79	A_u	25	various lattice vibrations
90	A_u	42	various lattice vibrations
94	E_u	31	various lattice vibrations
95	A_u	71	various lattice vibrations
101	E_u	64	various lattice vibrations
104	E_u	176	various lattice vibrations
109	E_u	33	various lattice vibrations
111	E_u	26	various lattice vibrations
114	E_u	89	various lattice vibrations
125	E_u	293	various lattice vibrations
128	E_u	54	various lattice vibrations
130	A_u	37	various lattice vibrations
137	A_u	23	various lattice vibrations
141	E_u	50	various lattice vibrations
162	E_u	1534	various lattice vibrations
169	E_u	661	various lattice vibrations
169	A_u	58	various lattice vibrations
174	E_u	3172	various lattice vibrations
189	A_u	792	various lattice vibrations
191	E_u	200	various lattice vibrations
205	A_u	2269	various lattice vibrations
210	A_u	357	various lattice vibrations
215	E_u	172	various lattice vibrations
219	A_u	115	various lattice vibrations
222	E_u	178	various lattice vibrations
223	A_u	644	various lattice vibrations
229	E_u	1498	various lattice vibrations
235	A_u	537	various lattice vibrations
236	E_u	2418	various lattice vibrations
241	A_u	3541	various lattice vibrations
242	E_u	1125	various lattice vibrations
249	A_u	249	various lattice vibrations
251	E_u	499	various lattice vibrations
261	E_u	783	various lattice vibrations
264	A_u	1863	various lattice vibrations
267	E_u	7609	various lattice vibrations
278	E_u	1488	various lattice vibrations
289	A_u	1190	various lattice vibrations

frequency/ cm^{-1}	Γ_{irrep}	intensity/ $km \cdot mol^{-1}$	assignment
293	A_u	35	various lattice vibrations
309	E_u	203	various lattice vibrations
323	A_u	61	various lattice vibrations
328	E_u	36	various lattice vibrations
334	E_u	316	various lattice vibrations
347	A_u	28	various lattice vibrations
361	E_u	95	various lattice vibrations
505	A_u	178	H^- vibration
537	A_u	1235	H^- vibration
559	E_u	956	H^- vibration
566	E_u	6229	H^- vibration
593	A_u	526	$[N–B–N]_i$ bending (v_3)
615	E_u	26	$[N–B–N]_i$ bending (v_3)
624	E_u	373	$[N–B–N]_o$ bending (v_3)
626	A_u	802	$[N–B–N]_o$ bending (v_3)
628	E_u	213	$[N–B–N]_o$ bending (v_3)
629	A_u	233	$[N–B–N]_o$ bending (v_3)
639	E_u	546	$[N–B–N]_o$ bending (v_3)
666	E_u	552	$[N–B–N]_o$ bending (v_3)
667	A_u	445	$[N–B–N]_o$ bending (v_3)
672	A_u	339	$[N–B–N]_o$ bending (v_3)
673	E_u	370	$[N–B–N]_o$ bending (v_3)
677	A_u	175	$[N–B–N]_o$ bending (v_3)
679	E_u	455	$[N–B–N]_o$ bending (v_3)
714	E_u	4292	H^- vibration
731	A_u	9568	H^- vibration
735	A_u	1519	H^- vibration
741	E_u	391	H^- vibration
769	E_u	4101	H^- vibration
794	E_u	5331	H^- vibration
830	E_u	5081	H^- vibration
837	A_u	13	H^- vibration
852	E_u	1441	H^- vibration
1100	E_u	67	symmetrical $[N–B–N]_o$ stretching (v_1)
1110	E_u	64	symmetrical $[N–B–N]_o$ stretching (v_1)
1111	A_u	41	symmetrical $[N–B–N]_o$ stretching (v_1)
1114	E_u	55	symmetrical $[N–B–N]_o$ stretching (v_1)
1656	A_u	8230	antisymmetrical $[N–B–N]_i$ stretching (v_2)
1737	E_u	135	antisymmetrical $[N–B–N]_o$ stretching (v_2)
1756	E_u	458	antisymmetrical $[N–B–N]_o$ stretching (v_2)
1758	A_u	6175	antisymmetrical $[N–B–N]_o$ stretching (v_2)
1760	E_u	15425	antisymmetrical $[N–B–N]_o$ stretching (v_2)
1785	A_u	87	antisymmetrical $[N–B–N]_o$ stretching (v_2)

Table S5.4. Assignment of Raman vibrations of $Ba_{12}[BN_2]_{6.67}H_4$ with frequency, irreducible representation and intensity obtained by quantum chemical calculations.

frequency/ cm^{-1}	Γ_{irrep}	intensity/ $km \cdot mol^{-1}$	assignment
44	E_g	795	various lattice vibrations
52	E_g	593	various lattice vibrations
59	E_g	63	various lattice vibrations
67	E_g	210	various lattice vibrations
69	A_g	57	various lattice vibrations
71	E_g	413	various lattice vibrations
74	A_g	33	various lattice vibrations
76	E_g	103	various lattice vibrations
77	A_g	67	various lattice vibrations
81	E_g	202	various lattice vibrations
85	A_g	35	various lattice vibrations
86	E_g	139	various lattice vibrations
92	A_g	61	various lattice vibrations
94	E_g	91	various lattice vibrations
97	E_g	211	various lattice vibrations
100	E_g	306	various lattice vibrations
104	A_g	18	various lattice vibrations
108	E_g	493	various lattice vibrations
109	E_g	235	various lattice vibrations
112	A_g	103	various lattice vibrations
113	E_g	139	various lattice vibrations
117	A_g	57	various lattice vibrations
120	E_g	52	various lattice vibrations
121	A_g	484	various lattice vibrations
136	A_g	26	various lattice vibrations
142	A_g	113	various lattice vibrations
146	E_g	92	various lattice vibrations
155	E_g	521	various lattice vibrations
161	E_g	661	various lattice vibrations
170	E_g	360	various lattice vibrations
180	E_g	744	various lattice vibrations
191	A_g	29	various lattice vibrations
194	E_g	407	various lattice vibrations
198	A_g	120	various lattice vibrations
202	E_g	571	various lattice vibrations
216	A_g	33	various lattice vibrations
222	E_g	527	various lattice vibrations
231	A_g	162	various lattice vibrations
232	E_g	40	various lattice vibrations
240	E_g	56	various lattice vibrations
249	A_g	169	various lattice vibrations

frequency/ cm^{-1}	**Γ_{irrep}**	**intensity/ $km \cdot mol^{-1}$**	**assignment**
250	E_g	31	various lattice vibrations
255	E_g	153	various lattice vibrations
256	A_g	142	various lattice vibrations
261	E_g	181	various lattice vibrations
271	E_g	35	various lattice vibrations
291	A_g	26	various lattice vibrations
297	A_g	18	various lattice vibrations
308	E_g	427	various lattice vibrations
315	A_g	611	various lattice vibrations
321	E_g	1000	various lattice vibrations
330	E_g	524	various lattice vibrations
337	A_g	17	various lattice vibrations
343	A_g	295	various lattice vibrations
345	E_g	155	various lattice vibrations
354	E_g	283	various lattice vibrations
557	E_g	29	H^- vibration
628	A_g	18	$[N–B–N]_o$ bending (v_3)
629	E_g	27	$[N–B–N]_o$ bending (v_3)
632	E_g	252	$[N–B–N]_o$ bending (v_3)
633	A_g	47	$[N–B–N]_o$ bending (v_3)
638	A_g	149	$[N–B–N]_o$ bending (v_3)
643	E_g	326	$[N–B–N]_o$ bending (v_3)
666	A_g	63	$[N–B–N]_o$ bending (v_3)
667	E_g	28	$[N–B–N]_o$ bending (v_3)
674	E_g	87	$[N–B–N]_o$ bending (v_3)
676	A_g	50	$[N–B–N]_o$ bending (v_3)
679	E_g	144	$[N–B–N]_o$ bending (v_3)
680	A_g	105	$[N–B–N]_o$ bending (v_3)
736	E_g	18	H^- vibration
1057	A_g	266	symmetrical $[N–B–N]_i$ stretching (v_1)
1099	A_g	656	symmetrical $[N–B–N]_o$ stretching (v_1)
1100	E_g	62	symmetrical $[N–B–N]_o$ stretching (v_1)
1109	A_g	971	symmetrical $[N–B–N]_o$ stretching (v_1)
1110	E_g	157	symmetrical $[N–B–N]_o$ stretching (v_1)
1116	A_g	707	symmetrical $[N–B–N]_o$ stretching (v_1)
1117	E_g	148	symmetrical $[N–B–N]_o$ stretching (v_1)

Quantum Chemical Calculations

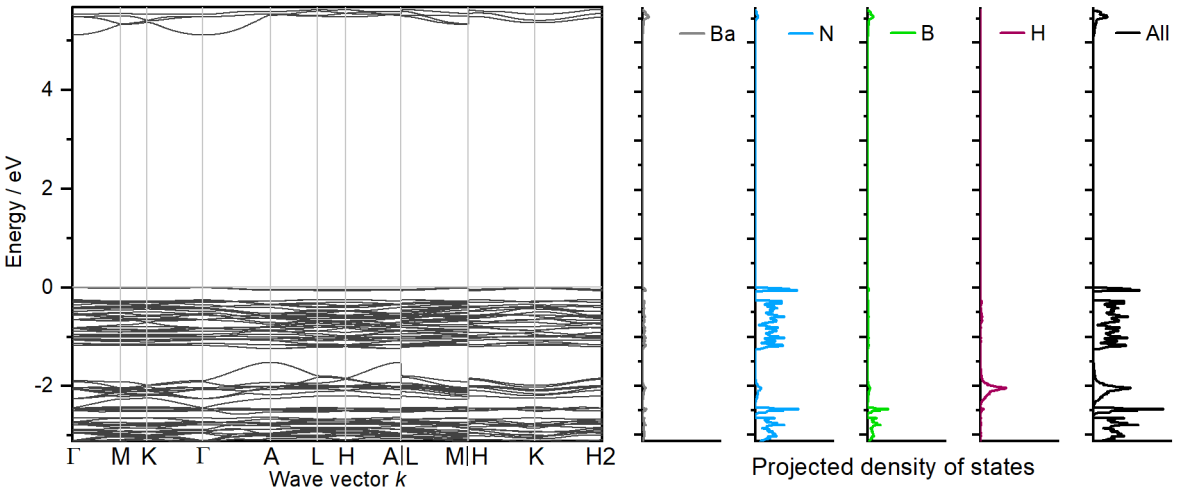

Figure S5.5. Electronic band structure and projected density of states of $Ba_{12}[BN_2]_{6.67}H_4$ calculated with the DFT-PBE0 method.

Optimized crystal structure of the ordered model of $Ba_{12}[BN_2]_{6.67}H_4$ as CIF (DFT-PBE0 method)

```
data_Ba12[BN2]6.67H4
_audit_creation_method FINDSYM

_cell_length_a    15.5122786200
_cell_length_b    15.5122786200
_cell_length_c    9.6035143800
_cell_angle_alpha 90.0000000000
_cell_angle_beta  90.0000000000
_cell_angle_gamma 120.0000000000

_symmetry_space_group_name_H-M "P -3"
_symmetry_Int_Tables_number 147
_space_group.reference_setting '147:-P 3'
_space_group.transform_Pp_abc a,b,c;0,0,0

loop_
_space_group_symop_id
_space_group_symop_operation_xyz
1 x,y,z
2 -y,x-y,z
3 -x+y,-x,z
4 -x,-y,-z
5 y,-x+y,-z
6 x-y,x,-z

loop_
_atom_site_label
```

```
_atom_site_type_symbol
_atom_site_symmetry_multiplicity
_atom_site_Wyckoff_label
_atom_site_fract_x
_atom_site_fract_y
_atom_site_fract_z
_atom_site_occupancy
Ba1 Ba   6 g 0.53026 0.17982  0.65695  1.00000
Ba2 Ba   6 g 0.19789 0.51369  -0.01705 1.00000
Ba3 Ba   6 g 0.85014 0.82931  0.33823  1.00000
Ba4 Ba   6 g 0.40640 0.29608  0.42538  1.00000
Ba5 Ba   6 g 0.06904 0.62596  0.75263  1.00000
Ba6 Ba   6 g 0.72410 -0.03994 0.08868  1.00000
N1  N    6 g 0.68447 0.14409  0.70920  1.00000
N2  N    6 g 0.35545 0.48315  0.03479  1.00000
N3  N    6 g 0.01861 0.81983  0.35809  1.00000
N4  N    6 g 0.43883 0.40620  0.19416  1.00000
N5  N    6 g 0.09869 0.73911  0.51710  1.00000
N6  N    6 g 0.77776 0.07088  0.85805  1.00000
B1  B    6 g 0.73818 0.11296  0.77932  1.00000
B2  B    6 g 0.40848 0.45287  0.10787  1.00000
B3  B    6 g 0.06748 0.78234  0.42578  1.00000
N7  N    2 d 0.33333 0.66667  0.52269  1.00000
N8  N    2 d 0.33333 0.66667  0.80412  1.00000
B4  B    2 d 0.33333 0.66667  0.66358  1.00000
H1  H    2 d 0.33333 0.66667  0.16553  1.00000
H2  H    1 b 0.00000 0.00000  0.50000  1.00000
H3  H    6 g 0.83161 0.66465  0.17293  1.00000
H4  H    3 f 0.50000 0.00000  0.50000  1.00000
```

9 Miscellaneous

9.1 List of Publications in this Thesis

1. **Strontium Nitridoborate Hydride Sr_2BN_2H Verified by Single-Crystal X-ray and Neutron Powder Diffraction**

   Sophia L. Wandelt, Ayla Karnas, Alexander Mutschke, Nathalie Kunkel, Clemens Ritter, and Wolfgang Schnick

   Inorg. Chem. **2022**, *61*, 12685–12691

The syntheses of this contribution were performed by Sophia L. Wandelt and Ayla Karnas during her Bachelor's thesis and work as a research assistant, which was both supervised by Sophia L. Wandelt and Wolfgang Schnick. Alexander Mutschke conducted all quantum chemical calculations as well as the FTIR and Raman measurements. Clemens Ritter performed the neutron powder diffraction experiment. The evaluation of all data, structure solution, literature screening, conceptualization and writing of the manuscript was conducted by Sophia L. Wandelt with support from Alexander Mutschke. Nathalie Kunkel took part with the correction of the manuscript. The revision process was done by Sophia L. Wandelt. Supervision of the research project was headed by Wolfgang Schnick. All authors contributed to the discussion of the results and revised the manuscript.

2. **A Novel Nitridoborate Hydride $Sr_{13}[BN_2]_6H_8$ Elucidated from X-ray and Neutron Diffraction Data**

   Sophia L. Wandelt, Alexander Mutschke, Dmitry Khalyavin, Jennifer Steinadler, and Wolfgang Schnick

   Chem. Eur. J. **2023**, e202301241

The syntheses and formal analyses were performed by Sophia L. Wandelt. Dmitry Khalyavin conducted the neutron powder diffraction measurements and supported the evaluation thereof. The evaluation and fitting of the NMR spectra was done by Jennifer Steinadler. Alexander Mutschke conducted all quantum chemical calculations as well as the Raman measurements and their evaluation. The structure solution, literature screening, conceptualization and writing of the manuscript was performed by Sophia L. Wandelt. The revision process was done by Sophia L. Wandelt. Supervision of the research project was headed by Wolfgang Schnick. All authors contributed to the discussion of the results and revised the manuscript.

3. Combining Nitridoborates, Nitrides and Hydrides – Synthesis and Characterization of the Multianionic $Sr_6N[BN_2]_2H_3$

Sophia L. Wandelt, Alexander Mutschke, Dmitry Khalyavin, Robert Calaminus, Jennifer Steinadler, Bettina V. Lotsch, and Wolfgang Schnick

Angew. Chem. Int. Ed. **2023**, e202313564

The syntheses and formal analyses were performed by Sophia L. Wandelt. Dmitry Khalyavin conducted the neutron powder diffraction measurements and supported the evaluation thereof. The evaluation and fitting of the NMR spectra was done by Jennifer Steinadler. Alexander Mutschke conducted all quantum chemical calculations as well as the Raman measurements and their evaluation. Robert Calaminus did the electrochemical impedance spectroscopy and chronopotentiometry measurements and their evaluation. The structure solution, literature screening, conceptualization and writing of the manuscript was performed by Sophia L. Wandelt. The revision process was done by Sophia L. Wandelt and Robert Calaminus. Supervision of the research project was headed by Bettina V. Lotsch and Wolfgang Schnick. All authors contributed to the discussion of the results and revised the manuscript**.**

4. $Ba_{12}[BN_2]_{6.67}H_4$ – A Disordered Anti-Skutterudite filled with Nitridoborate Anions

Sophia L. Wandelt, Alexander Mutschke, Dmitry Khalyavin, Jennifer Steinadler, Antti J. Karttunen, and Wolfgang Schnick

Angew. Chem. Int. Ed. **2023**, e202316469

The syntheses and formal analyses were performed by Sophia L. Wandelt. Dmitry Khalyavin conducted the neutron powder diffraction measurements and supported the evaluation thereof. The evaluation and fitting of the NMR spectra was done by Jennifer Steinadler. The theoretical NMR calculations were performed by Antti J. Karttunen. Alexander Mutschke conducted all other quantum chemical calculations as well as the Raman measurements and their evaluation. The structure solution, literature screening, conceptualization and writing of the manuscript was performed by Sophia L. Wandelt. Supervision of the research project was headed by Wolfgang Schnick. All authors contributed to the discussion of the results and revised the manuscript**.**

9.2 List of Publications beyond this Thesis

1. **Accessing Tetravalent Transition-Metal Nitridophosphates through High-pressure Metathesis**

   Simon D. Kloß, Sophia L. Wandelt, Andreas Weis, and Wolfgang Schnick

   Angew. Chem. Int. Ed. **2018**, *57*, 3192–3195

2. **High-pressure Metathesis of the $M_{1-x}PO_{3+4x}N_{1-4x}$ ($x \approx 0.05$) and $M_{0.75}PO_4$ (M = Zr, Hf) Orthophosphates**

   Simon D. Kloß, Andreas Weis, Sophia L. Wandelt, and Wolfgang Schnick

   Inorg. Chem. **2018**, *57*, 4164–4170

3. **Ratiometric Detection of Nerve Agents by Coupling Complementary Properties of Silicon-Based Quantum Dots and Green Fluorescent Protein**

   Cristopher J. T. Robidillo, Sophia L. Wandelt, Rochelin Dalangin, Lijuan Zhang, Haoyang Yu, Alkiviathes Meldrum, Robert E. Campbell, and Jonathan G. C. Veinot

   ACS Appl. Mater. Interfaces **2019**, *11*, 33478–33488

4. **Order and Disorder in Mixed (Si,P)–N Networks $Sr_2SiP_2N_6:Eu^{2+}$ and $Sr_5Si_2P_6N_{16}:Eu^{2+}$**
   Marwin Dialer, Monika M. Pointner, Sophia L. Wandelt, Philipp Strobel, Peter J. Schmidt, Lkhamsuren Bayarjargal, Björn Winkler, and Wolfgang Schnick

   Adv. Opt. Mater. **2023**, 2302668

9.3 Conference Contributions and Oral Presentations

1. Erleuchtende Erkenntnisse im System Sr–Ba–Mg–Si-N

Sophia L. Wandelt

Talk, 5. Obergurgl-Seminar Festkörperchemie

Obergurgl (Austria), 31.01.2020

2. $Sr[Mg_3SiN_4]:Eu^{2+}$ und $Ba[Mg_3SiN_4]:Eu^{2+}$

Sophia L. Wandelt

Talk, Schnick Group Seminar

Munich (Germany), 13.05.2020

3. Nitridoborathydride und Design of Experiments

Sophia L. Wandelt

Talk, Schnick Group Seminar

Munich (Germany), 09.06.2021

4. Nitridoborathydride und Neutronen

Sophia L. Wandelt

Talk, Schnick Group Seminar

Munich (Germany), 25.05.2022

5. Structure Elucidation of Strontium Nitridoborate Hydride Sr_2BN_2H with Single Crystal X-ray and Neutron Powder Diffraction

Sophia L. Wandelt, Ayla Karnas, Alexander Mutschke, Nathalie Kunkel, Clemens Ritter, Wolfgang Schnick

Poster, 21. Vortragstagung für Anorganische Chemie der Fachgruppen Wöhler-Vereinigung und Festkörperchemie und Materialforschung

Marburg (Germany), 27.09.2022

6. Cubic Icosahedra

Sophia L. Wandelt

Talk, 6. Obergurgl-Seminar Festkörperchemie

Obergurgl (Austria), 26.01.2023

7. Expanding the Sr–B–N–H System with $Sr_{13}[BN_2]_6H_8$ Validated by X-ray and Neutron Diffraction

Sophia L. Wandelt, Alexander Mutschke, Dmitry Khalyavin, Wolfgang Schnick

Poster, European Conference on Neutron Scattering

Garching bei München (Germany), 21.03.2023

8. Chemodynamical Evolution of Galaxies

Sophia L. Wandelt

Talk, Grün Astrophysics Group Seminar

München (Germany), 26.04.2023

9. Expanding the Hydride Chemistry – Introducing the Ion Conducting Nitridoborate Nitride Hydride $Sr_6N[BN_2]_2H_3$

Sophia L. Wandelt, Alexander Mutschke, Robert Calaminus, Jennifer Steinadler, Dmitry Khalyavin, Bettina V. Lotsch, Wolfgang Schnick

Poster, 11th International Symposium on Nitrides

Saint-Malo (France), 03.05.2023

9.4 Deposited Crystal Structures

The Crystallographic Information Files (CIF) of the investigated compounds are provided free of charge by the joint Cambridge Crystallographic Data Centre and Fachinformationszentrum Karlsruhe Access Structures service (http://www.ccdc.cam.ac.uk/structures) by quoting the corresponding deposition number.

compound	**CSD-**
Sr_2BN_2H	2164755
$Sr_2{}^{11}BN_2D_{0.86}H_{0.14}$	2171502
$Sr_{13}[BN_2]_6H_8$	2239357
$Sr_{13}[{}^{11}BN_2]_6D_{6.8}H_{1.2}$	2239358
$Sr_6N[BN_2]_2H_3$	2279203
$Sr_6N[{}^{11}BN_2]_2D_3$	2279204
$Ba_{12}[BN_2]_{6.67}H_4$	2300675
$Ba_{12}[{}^{11}BN_2]_{6.67}H_4$	2300676